Fermilab

FERMILAB-Conf-01/107-T July 2001

Fermilab-Conf-01/107-T

WORKSHOP ON AN e^+e^- COLLIDER IN THE VLHC TUNNEL

Contributions to the Workshop held at the Illinois Institute of Technology, Chicago, IL, March 9-11, 2001

Editors:

G. Dugan

Laboratory of Nuclear Studies, Cornell University, Ithaca, NY 14850

A. Tollestrup

Fermilab, Batavia, IL 60510

Authors:

J. Norem, L. Teng, S. Sharma

Argonne National Lab, Argonne, IL 60439

R. Assmann, K. Cornelis, E. Keil, O. Grobner

CERN, Geneva, Switzerland

S. Belomestnykh, G. Dugan, R. Talman

Laboratory of Nuclear Studies, Cornell University, Ithaca, NY 14850

C. Johnstone, T. Sen

Fermilab, Batavia, IL 60510

D. Amidei

University of Michigan, Ann Arbor, MI 48109

1 INTRODUCTION

This document is a collection of the contributions made to the March IIT workshop on an e^+e^- collider in the VLHC tunnel. This machine, which is based on a relatively conservative extrapolation of LEP technology, has a baseline luminosity of 10^{33} /cm^2/s at a CM energy of 370 GeV. The overall parameters and general description of such a machine is described in T. Sen and J. Norem, **A Very Large Lepton Collider in the VLHC Tunnel**, to be published. A preprint of this paper is included as Appendix 2 of this report.

The intention of the workshop was to define the parameters of such a collider and make them available to the community for use in further physics studies. It is clear that the machine cannot compete with a full scale linear collider. Its main interest would be if a VLHC were built and if a linear collider did not already exist. In this case, it could provide a limited and perhaps crucial view of low mass Higgs states. Although the study is incomplete, it does define rather well the parameters of the machine, as well as the challenges that the design faces. The study benefited greatly from the participation of the machine experts that were willing to spend time looking at the design.

In this document, the workshop contributions are organized into sections which cover the physics motivation for the machine; the injector; beam dynamics issues in the collider; and accelerator systems.

The physics section describes luminosity benchmarks for study of a light Higgs boson, and machine performance issues related to lineshape measurements at the $t\bar{t}$ threshold.

The contribution on the injector presents a design for a 45 GeV injector. The injection energy is motivated by two considerations: the collider has potential stability problems at injection, which are mitigated by a relatively high injection energy; and, at this energy, the injector can also serve as a Z^0 factory. One of the principal conclusions of the IIT workshop was that this was the most natural way to provide a high-luminosity Z^0 factory with polarized beams.

The beam dynamics contributions cover a range of topics, including experience from LEP, design options for the lattice and IR's that aim at increasing the luminosity to close to 10^{34} /cm^2/s, and considerations on beam stability, rf system distribution, beam separation, and radiative spin polarization of the beams.

The magnet, vacuum system, and rf system required for the machine are discussed in the accelerator systems contributions.

Finally, in the conclusions section, the leading R&D issues for the machine, as identified at the workshop, are summarized. In an Appendix, some thoughts on beam-beam considerations for a VLLC are provided.

Thanks must also be extended to the Illinois Consortium for Accelerator Research and the Illinois Institute of Technology for hosting the workshop and providing the necessary financial support. In particular, without the support of Prof. T. Morrison, Prof. D. Kaplan and Prof. H. Rubin the workshop would not have been possible.

2 SOME PHYSICS BENCHMARKS FOR A 400 GEV VLLC

Dante Amidei
University of Michigan, Ann Arbor, MI 48109

2.1 Introduction

The physics of high energy e^+e^- collisions has been detailed in a vast literature. For a given energy and luminosity, circular and linear e^+e^- colliders have similar physics programs, up to differing capabilities with beam polarization and energy control. An electron synchrotron in the VLHC tunnel (VLLC) could access physics in the range 200-400 GeV, but the limited energy reach severely restricts the additional physics program. However, in the event that a linear electron collider is not built, a machine as described here could provide a useful addition to the VLHC facility.

The frontier program at a VLCC would include the study of a light Higgs boson, the detailed examination of $t\bar{t}$ pair production, precision measurements at the WW threshold, and study of putative low lying SUSY states. The full catalog of physics opportunities with these measurements may be extrapolated from the linear collider literature. For the purpose of this machine study, I use two topics from that literature to benchmark pertinent machine performance issues: the luminosity required to study a light Higgs boson, and the effect of beam-beam effects on lineshape measurements at the $t\bar{t}$ threshold. I assume a VLCC with an instantaneous luminosity of $5\text{x}10^{33}\ \text{cm}^{-2}\ \text{s}^{-1}$, and integral accumulations of 50 fb^{-1} per year. The discussion here draws entirely on previous LC study efforts [1,4], which are assumed reliable, unless noted.

Note that the facility design emerging from this study includes a smaller injection ring, operating at 45 GeV and L = $10^{33}\ \text{cm}^{-2}\ \text{s}^{-1}$. If good polarization is possible, this is a platform for a giga-Z program [2].

2.2 Luminosity Requirements for Study of a Light Higgs Boson

The associated production mode ZH, already utilized in the Higgs search at LEP, remains key at higher energies. The main measurements are based on final state reconstruction, and the main demand on the machine is luminosity. As seen in Fig. 1, the cross section for this process peaks at $\sqrt{s} \approx M_Z + \sqrt{2}M_H$ [4]. For $110 < M_H < 150\ \text{GeV}/\text{c}^2$, operating at E_{cm} = 300 GeV, cross sections are of order 150-200 fb, yielding samples of between 5 and 10 thousand signal events for $50\,\text{fb}^{-1}$. Reconstruction of the Z in any of its visible decay modes reveals the recoiling Higgs as a peak in the missing mass, even if the Higgs decays are invisible. In the case of invisible Z decays to neutrinos, a SM-like Higgs can be reconstructed from b-tagged jets in the decay $\text{H} \rightarrow b\bar{b}$. Combining all channels, $1\,\text{fb}^{-1}$ is said to be sufficient for discovery. [5]

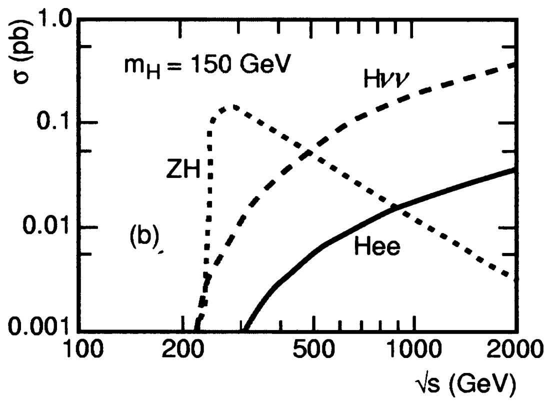

Figure 1 SM Higgs cross section

Using ZH, benchmark measurements of the Higgs mass, cross section, and CP follow with 50 fb^{-1}[5]. The combination of the di-jet mass in $H \to b\bar{b}$ and the recoil mass in $Z \to l\bar{l}$ gives the Higgs mass M_H to a precision of 180 MeV. The total ZZh cross section, which is proportional to the ZZH coupling, and tests whether a single Higgs is responsible for the whole Z mass, can be measured to 4%. The angular distribution of the Higgs and the polarization of the Z are shown to be sensitive to Higgs CP with 50 fb^{-1} at 300 GeV.

With 100 fb^{-1}, the ZH mode can be used for detailed study of branching ratios. Using $\sqrt{N}$ scaling from the study of Battaglia [6], the precision expected on the branching ratios for the measurable modes is given as follows:

Mode	BR error
$b\bar{b}$	4%
$c\bar{c}$	14%
$\tau\bar{\tau}$	10%
WW*	11%

The fermion modes are identified with heavy flavor tagging and lepton ID, and can be compared with both the SM prediction for the Yukawa couplings and those for a non-minimal Higgs sector. The BR(WW) in combination with the WWh coupling determines the Higgs total width. The WWh coupling follows from the ZZh coupling and the Weinberg angle, so the Higgs width can be inferred indirectly to the precision of BR(WW*).

Samples of 200 fb^{-1} would allow direct search for additional Higgs bosons in ZZH' down to a few percent of the Standard Model cross section. If all Higgs are lighter than 150 GeV, the sum rule relating all the couplings to the Z mass can be checked with 5% accuracy [3]. A final item of interest, the Higgs trilinear couplings, to be measured in ZHH, require LC like conditions of 500 GeV and 600 fb^{-1}.

2.3 . Line-shape Measurements at the Top Threshold

Differences in energy control and beam-beam interactions in the synchrotron *vs.* linear collider may impact lineshape measurements. For the VLLC, the obvious benchmark is the $t\bar{t}$ cross section at threshold, where the lineshape is, in principle, sensitive to m_t, the total top decay width Γ_t, the strong coupling α_s, the Higgs mass, and the Higgs Yukawa coupling. Older LC studies (*ca*. Snowmass 96) estimate the measurement precision for each of these quantities. Recent questions about the reliability of the theory curves in these studies would seem to be answered by a new renormalization group based calculation claiming the remaining theoretical error is now small compared to the size of the effects to be measured [7]. I therefore review lineshape issues as in the early work.

Since the top total decay width $\Gamma_t \approx 1.5$ GeV, bound state effects are described by the Coulomb-like potential of perturbative QCD, and the resonance is small and broad.

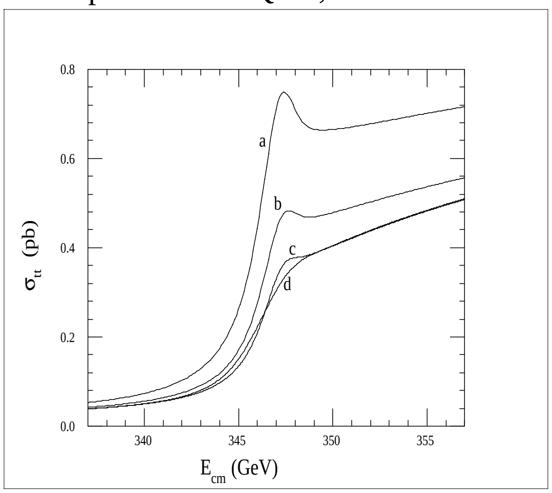

Figure 2 Threshold behavior of top pair production **a**) theoretical **b**) add ISR **c**) add beamstrahlung **d**) add energy spread

Fig. 2, above, is taken from a linear collider study [8]. Curve **a** shows the theoretical excitation spectrum; with QCD level spacings smaller than Γ_t, all resonances merge under the 1S state. Curve **b** shows the effect of ISR, which will be the same at a circular machine. Curve **c** shows the additional effect of beamstrahlung for a typical NLC X-band collider design, with beamstrahlung parameter of approximately 0.05. The main effect of ISR and beamstrahlung is to move a significant fraction of the luminosity to energies below the threshold; however, we see that the resonance is also degraded to a shoulder. Curve **d** incorporates the effect of a 0.6% energy spread, and is seen to remove the shoulder, leaving the lineshape information mostly in the slope. The detailed luminosity spectrum can be unfolded from the acollinearity of Bhabha scattering events as a function of $\sqrt{s}$ [9]. At a LC, the magnitude of the energy spread can be measured with spectrometers on the spent beam. *It would be very interesting to recalculate these curves for the VLCC case of significantly reduced beamstrahlung and an energy spread* *of just 0.1%, to see if the resonance information is better preserved, and can be studied without requiring such a significant unfold of the lineshape systematics.*

For m_t= 175GeV/c^2, the $t\bar{t}$ cross section at threshold is roughly 0.5 pb, yielding 25,000 events with 50 fb^{-1}. The main background is WW production with roughly 10 times the rate. Linear collider studies suggest this may be normalized by changing the beam polarization; we will assume here that other techniques will be available, for instance using the high forward peaking of WW.

A simulation study for m_t= 170 GeV/c^2, using a scan of 11 points across the threshold with 1 fb^{-1}each, including the effects of ISR and beamstrahlung, but only a 0.1% energy spread, finds m_t measured to 350 MeV and α_s to 0.007 [10,11]. Fixing α_s via other measurements would improve the precision on top mass.

The effect of non-standard width Γ_t is shown for the ideal and "realistic" beams case in Fig 3.

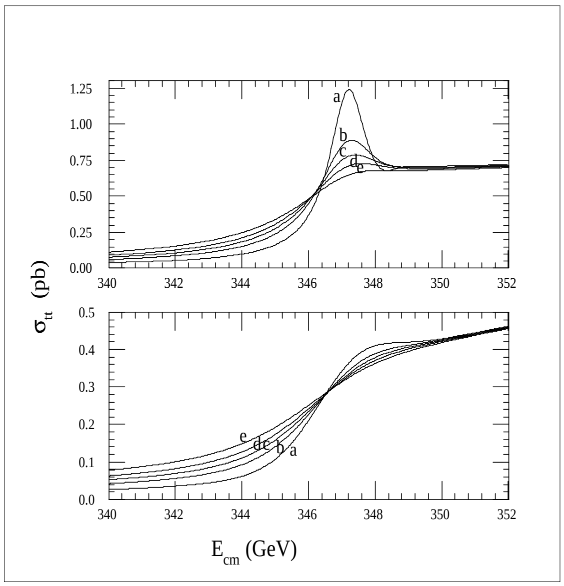

Figure 3 Lineshape for m_t= 175 GeV when the decay width is scaled by **a**) 0.5 **b**) 0.8 **c**) 1.0 **d**) 1.2 **e**) 1.5

If m_t and α_s are known, the study above claims that measurement of the cross section below threshold can determine the width Γ_t to 10% with 50 fb^{-1}. However, note that this study is odd because it mixes LC sized beamstrahlung with CC sized energy spread.

The short range Yukawa potential from a light Higgs affects $t\bar{t}$ wavefunction at the origin. Fig 4, below, shows the ideal lineshape normalization vs. m_{Higgs} [12]. If m_{Higgs} is known, this shape is sensitive to the Yukawa coupling λ_t. A study incorporating "realistic" LC beam conditions, shows the effect expected with m_{Higgs}= 300 GeV/c^2, for 50% scaling variations in the SM value of λ_t[8] and claims that such modifications to λ_t can be determined to 25% with 50 fb^{-1}.[11].

It would be interesting to re-examine all of these measurements in the context of VLLC parameters, and this may be accomplished with modest effort by piggy-backing on future Linear Collider studies.

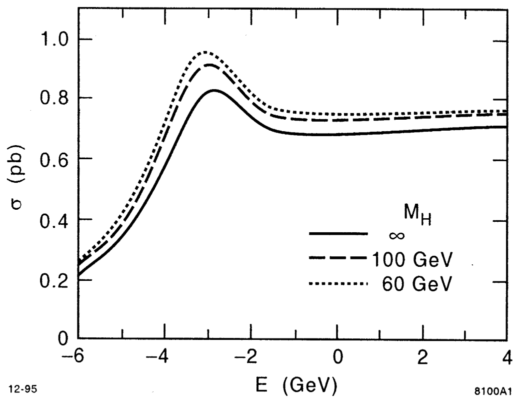

Figure 4 Ideal lineshape vs. m_{Higgs} (no beam effects)

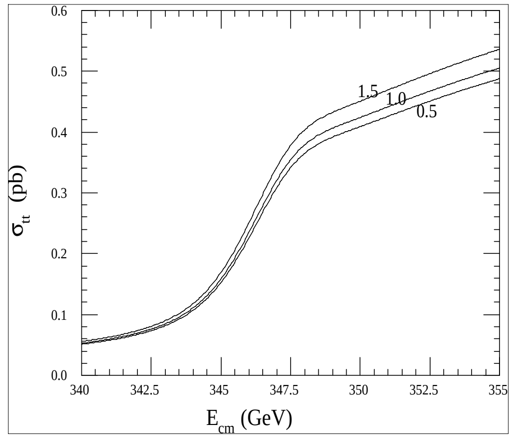

Figure 5 Lineshape vs. Yukawa coupling scale factor

Finally, it is worth noting that the VLLC is a fine environment for direct top measurements above threshold. The $t\bar{t}$ final state is reconstructable with good efficiency and accuracy. With $10\,\mathrm{fb}^{-1}$, the decay $t \rightarrow H^{\pm}b$ may be observed at 3σ down to BR = 5%; with $30\,\mathrm{fb}^{-1}$, the decay $t \rightarrow \tilde{t} + \mathrm{LSP}$ may be observed at 3σ down to BR = 5%, for $m_{\tilde{t}} = 100\ \mathrm{GeV}/c^2$ and $m_{LSP} = 40\mathrm{GeV}/c^2$ [13].

There is a large literature on study of anomalous couplings of $t\bar{t}$ to $Z - \gamma$ [14], many of which employ beam polarization at a LC. *Sensitivity to these effects via angular distributions in the* $t\bar{t}$ *final state produced with unpolarized beams should be a topic for future study.*

2.4 References

[1] See, for instance, J. Bagger et al., “The Case for a 500 GeV e^+e^- Linear Collider”, hep-ex/0007022.

[2] E. Keil, “A Z Factory in the VLCC Injector”, Section 3 of this work, presented at the Workshop on an e^+e^- Ring at VLHC, Illinois Institute of Technology, Chicago, IL. March 2001.

[3] See, for instance, J. Bagger et al., “The Case for a 500 GeV e^+e^-Linear Collider”, hep-ex/0007022.

[4] “Physics and Technology of the Next Linear Collider”, hep-ex/9605011

[5] P. Janot, in “Physics and Experiments with Linear Colliders”, R. Orava. P. Eerola, and M. Nordberg, eds, World Scientific, Singapore, 1992.

[6] M. Battaglia, in “Physics and Experiments with Future e^+e^- Linear Colliders, E. Fernandez and A. Pacheco, eds, hep-ph/9910271.

[7] A. Hoang et al,“A Renormalization Group Improved Calculation of Top Quark Production near Threshold”, CERN-TH/2000-340, hep-ph/0011254.

[8] R. Frey et al. “Top Quark Physics: Future Measurements”, hep-ph/9704243

[9] N.M. Frary and D. Miller, DESY 92-123A, Vol I, 1992, p. 379.

[10] K. Fukii, T. Matsui, and Y. Sumino, Phys Rev **D50**, 4341, 1994.

[11] K. Fuji, 1995 SLAC Summer Institute

[12] R. Harlander, M. Jezabek, and J. H. Kuhn, hep-ph/9506292.

[13] H. Murayama and M. Peskin, "Physics Opportunities of e^+e^- Linear Colliders", SLAC-PUB-7149, hep-ex/9606003.
[14] See [8] above, and refs therein.

3 A Z FACTORY IN THE VLLC INJECTOR

Eberhard Keil

CERN, Geneva, Switzerland

Abstract

A Z factory in the VLLC injector with polarized beams is presented. Its circumference is about two Tevatron circumferences. Wigglers make the bunches longer at injection, and reduce the risk of collective instabilities and the polarization time at collision energy. However, they are powerful sources of synchrotron radiation, and associated damage. The vertical amplitude function β_y^* at the interaction point is assumed to be 40 mm. At this value, reaching a peak luminosity L=10^{33} $cm^{-2}s^{-1}$ implies about 50 MW of RF power for the two beams. A lower value of β_y^* could be exploited by using any intermediate method between two extremes: (i) At constant L and RF power, the circumference and the polarization time could be reduced. (ii) At constant circumference, RF power, and polarization time, L could be increased. Apertures and separation schemes have only been designed at the collision energy. In the discussion of polarization time, peak polarization and figure of merit, all depolarizing mechanisms, due to the momentum spread in the beam and orbit errors, are ignored.

3.1 Introduction

The idea for a Z factory in the injector for a Very Large Lepton Collider VLLC in the VLHC tunnel was developed during the Workshop on a e^+e^- collider in VLHC tunnel, held 9 to 11 March 2001 at the Illinois Institute of Technology, Chicago. The VLLC [1] proper is designed for 184 GeV maximum energy. Operating it a the Z energy is unattractive, for two reasons: The parameters appear to be stretched, and polarization is excluded because of the polarization time of several days, by far exceeding the beam-beam bremsstrahlung lifetime.

Injection energies into the VLLC between 30 and 50 GeV were considered in [1]. Injection at 20GeV was proposed in [2]. Both proposals suffer from the low magnetic field, and collective instabilities. For both reasons, a higher injection energy looks attractive.

The parameter search reported below was done in *Mathematica* with a notebook and packages. The notebook `z0fact12km.nb` [3] is specific. The packages [4] contain formulae valid for many machines and $e^{\pm}$, $\mu^{\pm}$, and p. The notebook contains the input parameters from the user, and finds parameters for the interaction point(s) IP, arcs in thin-element approximation, synchrotron radiation, RF system, collective effects, etc. It also writes a short file with parameters for MAD [5]. MAD finds solutions for finite elements, corrects chromaticity, tracks, etc.

3.2 Parameters

The first step in the parameter search for the Z factory is determining some overall parameters. This is done in the next section. The parameters in the tables agree with those in `z0fact12km.nb` at 9:58:36 on 6 April 2001.

3.2.1 Overall Parameters

Polarized $e^\pm$ are essential for a Z factory [6]. Hence, the choice of bending radius ρ, average arc radius R, and circumference `cirC` is a compromise between two conflicting requirements. A short polarization time is achieved by making these quantities small. A small energy spread with little depolarization, and small synchrotron radiation losses are achieved by making these quantities large. Having tried machines with a circumference equal to or twice that of the Tevatron, we settled for the latter. Table 1 shows the overall Z factory parameters.

Ideally, one would adjust the Z factory parameters such that the number of bunches and their population is equal to that needed for the VLLC. By also choosing the ratio of circumferences appropriately, one could profit from the powerful injector, and transfer both e^+ and e^- bunches into the correct buckets of VLLC in a fraction of a second, in the same style as the transfer of proton bunches from SPS to LHC.

Table 1: Overall Z factory parameters. Here and in later tables, asterisks (*) mark input parameters, and *Mathematica* variables are written as `teletype` characters.

*Collision energy `collE`	46 [GeV]
*Bending radius ρ	1200 [m]
*Average arc radius `R`	1400 [m]
*Circumference `cirC`	12566 [m]
Total arc length `totArcL`	8796.46 [m]
Revolution frequency `revolF`	23856.7 [Hz]
*Number of bunches `bunchK`	80
Bunch spacing `bunchS`	157.08 [m]
Dipole field `dipoleB`	0.127866 [T]

3.2.2 Interaction Point Parameters

The next logical step in the parameter search is fixing the beam parameters at the interaction point(s) such that the design luminosity is reached at the design beam-beam tune shift parameters $\xi_x = \xi_y$ and at the collision energy. Table 2 shows the results of this calculation. The assumed beam-beam tune shift parameters are smaller than in the VLLC [1] by a factor of two. The amplitude functions at the interaction point β_{IPx} and β_{IPy} are a little smaller. These assumptions need justification. The ideal goal of having bunch number and bunch population equal to those in the VLLC is also not reached. The bunch population is only about 37% of the VLLC value. This can be fixed easily, once the VLLC parameters are more stable. I assume flat beams and optimum coupling with $\sigma_{IPx}/\sigma_{IPy} = \beta_{IPx}/\beta_{IPy}$ and $\sigma'_{IPx} = \sigma'_{IPy}$.

Table 2: Interaction Point Parameters

*Beam-beam tune shift parameters $\xi_x = \xi_y$	0.05
*Amplitude functions at IP β_{IPx}, β_{IPy}	0.8, 0.04 [m]
Bunch population `bunchN`	2.4993 x 10^{11}
Bunch current `bunchI`	0.955302 [mA]
Normalized hor. Emittance $\varepsilon_x = \beta\gamma\sigma_{IPx}^2 / \beta_{IPx}$	2.13507 [mm]
Normalized vert. Emittance $\varepsilon_y = \beta\gamma\sigma_{IPy}^2 / \beta_{IPy}$	0.106753 [mm]
Hor. RMS beam radius σ_{IPx}	0.137746 [mm]
Vert. RMS beam radius σ_{IPy}	6.88731 [μm]
RMS beam divergence $\sigma'_{IPx} = \sigma'_{IPy}$	0.172183 [mrad]
Beam current `beamI`	0.0764241 [A]
*Luminosity L	10^{33} [$cm^{-2}\,s^{-1}$]

3.2.3 Arc Parameters

The objective of the arc design is choosing the tune of the arcs such that the normalized emittance ε_x in Table 2 is equal to the equilibrium emittance from quantum excitation and synchrotron radiation damping. Table 3 shows the resulting unspectacular arc parameters. The length of the arc quadrupoles is the largest of three lower limits, given by (i) the pole tip field, an engineering constraint, (ii) the condition that the quadrupole field at one RMS beam radius be at most equal to the dipole field, avoiding radiative betatron synchrotron coupling [7] and (iii) the condition that the variation of the damping partition number with the momentum error $\left| dJ_x / d(\delta p/p) \right| \leq 500$, avoiding tight tolerances on the RF frequency, given by:

$$\frac{\Delta f}{f} = \frac{\eta \Delta J_x}{dJ_x / d(\delta p / p)} \tag{3.1}$$

Table 3: Arc Parameters

*Phase advance `phaseAdv`/2π	0.25
Number of FODO periods in arcs `periodN`	222
Arc tune Q	55.5
Length of arc periods `periodL`	39.6237 [m]
Bending angle of arc periods `periodA`	0.0283026
Average amplitude function β_x	25.2252 [m]
Average dispersion D_x	0.454509 [m]
Maximum amplitude function $\hat{\beta}_x$	67.6419 [m]
Maximum dispersion D_x^{max}	0.758975 [m]
Length of dipoles/half cell	16.9816 [m]
Length of arc quadrupole `quadL`	0.611337 [m]
Focal length of arc quadrupole `focalL`	14.0091 [m]
Momentum compaction η	0.000268682

3.2.4 Wiggler Parameters

Damping wigglers reduce the polarization time by a factor `polF` at 46 GeV. They are installed in straight sections where the dispersion vanishes, and reduce the equilibrium emittance by a factor `1/lossF`. They increase the synchrotron radiation loss by a factor `lossF`, and the relative RMS energy spread by a factor `sigeF`. The three factors are related by `sigeF`^{2}`=polF/lossF` [8]. Table 4 shows their parameters. A total length `plusL` of positive wigglers is needed. The field there points in the same direction as in the arc dipoles. I assume that the field in the positive wigglers is `plusB`=0.5 T. In the negative wigglers it is smaller by a factor `ratioB`=6, in order to preserve most of the equilibrium polarization. Many of the parameters are quite sensitive to the wiggler field `plusB`, which should be carefully chosen. The calculation ignores the depolarization due to the energy spread and orbit errors. In total, the wigglers occupy about 3.7% of the Z factory circumference. Wigglers are useful since `lossF` < `polF`.

Table 4: Wiggler Parameters

*Energy	12 GeV	46 GeV
*Emittance reduction factor `epsF`	0.3	0.9179
*Magnetic field in positive wigglers	0.5 [T]	0.5 [T]
Length of positive wigglers `plusL`	67.1135 [m]	37.8037 [m]
Energy spread enhancement factor `sigeF`	3.08927	1.09577
Energy loss enhancement factor `lossF`	3.33333	1.08944
Polarization rate enhancement factor `polF`		1.30812
Polarization time `tauP`		0.292935 [h]
Equilibrium polarization		0.911999
RMS relative energy spread σ_e	0.000916726	0.00124643
Average hor. RMS beam radius σ_x	0.432334	0.95876 [mm]
Maximum hor. RMS beam radius $\hat{\sigma}_x$	0.720959	1.58089 [mm]

At injection and during acceleration, damping wigglers increase the RMS energy spread and the bunch length, and decrease the transverse emittance and the synchrotron radiation time. This improves the collective effects. Table 4 also shows the wiggler parameters at injection.

3.2.5 Synchrotron Radiation Parameters

Table 5 shows the synchrotron radiation parameters that can be calculated from the information available. The synchrotron radiation power is substantial, amounting to about 50 MW for two beams. The linear synchrotron radiation power density is a factor 1.7 higher than in LEP2 [9]. Synchrotron radiation power and power density are simply consequences of the choice of the parameters L, $\xi_x = \xi_y$ and $\beta_y << \beta_x$.

Table 5: Synchrotron Radiation (SR) Parameters. Only the loss/turn, the power/beam and the damping time τ_x include the effect of the wigglers. All other quantities apply to the arcs.

*Energy	12 GeV	46 GeV
SR loss/turn	5.09632 [MV]	359.612 [MV]
SR power/beam	0.38948[MW]	27.483 [MW]
Linear SR power density/beam	13.2831 W/m	2867.82 W/m
Horizontal amplitude damping time τ_x	197.398 msec	10.724 msec
Critical photon energy	3.19474 [kV]	179.939 [kV]
Total number of photons	8.4278 x10^{16}/[m-sec]	3.2306x10^{17}/[m-sec]
*Vacuum chamber radius *b*	40 mm	40 mm
`distSR`	10.5829 m	10.5829 m
`incidenceA`	7.5592 mrad	7.5592 mrad
`spotSR`	0.778923 [mm]	0.345143 [mm]
`powSRm2`	0.0170532 W/mm^2	8.30908 W/mm^2

The last four parameters in Table 5 are related to where and how the synchrotron radiation hits the vacuum chamber. I assume quite generously that it has 40 mm radius. The synchrotron radiation hits the vacuum chamber a distance `distSR` downstream from the point where it is emitted, at an angle `incidenceA`. The height of the strip of vacuum chamber `spotSR` includes the contributions of the opening angle of the synchrotron radiation and the vertical divergence of the beam. The power density in the strip is `powSRm2`. The linear synchrotron radiation power density generated by the positive wigglers is 51 kW/m, a factor 18 higher than in the arcs.

3.2.6 RF System Parameters

Table 6 shows the parameters of the RF system. The harmonic number h_{RF} is a multiple of the number of bunches. The exact values of RF wavelength λ_{RF} and frequency f_{RF} follow from h_{RF}. At 46 GeV, the peak voltage `voltRF` and the remaining parameters follow from the imposed quantum lifetime τ_Q. The RF system must supply about 450 MV total peak voltage, and about 55 MW total power to the two beams. It will probably consist of about 200 single-cell, super-conducting cavities, each with about 2.25 MV peak voltage and about 275 kW peak power, within the reach of typical couplers. At 12 GeV, the parameters of the RF system are adjusted such that the quantum lifetime τ_Q is the same at 12 and 46 GeV.

Table 6: RF System Parameters

*Energy	12 GeV	46 GeV
*Quantum lifetime τ_Q	24 [h]	24 [h]
Harmonic number h_{RF}	16720	16720
RF wavelength λ_{RF}	0.751577 [m]	0.751577 [m]
Frequency f_{RF}	398.884[MHz]	398.884[MHz]
Relative bucket height `bucketH`	0.00731511	0.0079418
Overvoltage factor `overV`	1.486221	1.1517
Peak RF voltage `voltRF`	25.2476 [MV]	451.21 [MV]
Stable phase angle/2π ϕ_s	0.382536	0.332613
Synchrotron tune Q_s	0.0333595	0.0589835
RMS bunch length σ_s	14.7669 [mm]	11.3555 [mm]
Bunch area `bunchArea` $4\pi E\sigma_e\sigma_s/c$	0.0068092[Vs]	0.027291[Vs]
Beam-beam bremsstrahlung lifetime τ_{bb}		9.84998 [h]

Knowing the parameters of the RF system, the beam-beam bremsstrahlung lifetime $\tau_{bb} \approx$ 9.8 h can be calculated. It is roughly proportional to the vertical amplitude function β_{IPy} at the interaction point. The polarization time `tauP` in Table 4 must be much shorter, in order to reach a useful level of polarization within a run.

3.2.7 Collective Effects

Table 7 shows results on collective effects, calculated at injection energy, 12 GeV, given by the maximum e^+e^- energy of the Main Injector [1], and at collision energy, 46 GeV. I use rather standard formulae [10,11,12,13]. Converting the threshold for the transverse mode-coupling instability $Z_\perp^{\mathrm{TMCI}}$ in Table 7 to its longitudinal equivalent $Z_\parallel^{\mathrm{TMCI}}$ with the standard formula [14], vacuum chamber radius b and circumference C

$$Z^{\mathrm{TMCI}}{}_\parallel = \frac{\pi b^2 Z_\perp{}^{\mathrm{TMCI}}}{C} \tag{3.2}$$

yields $Z_\parallel^{\mathrm{TMCI}} \approx$ 2.9224 Ω at 45 GeV, which looks safe, and $Z_\parallel^{\mathrm{TMCI}} \approx$ 0.5607 Ω at 12 GeV, which is less safe. The growth rate of the resistive-wall instability, calculated for a mode number *(n-Q)* =0.25, is faster than the damping rate due to synchrotron radiation $1/\tau_x \approx$ 16.8863/s at 12 GeV. The resistive-wall power is a small fraction of the synchrotron radiation power. The transverse resistive wall impedance is above the threshold for the transverse mode-coupling instability, as claimed by G. Dugan.

Table 7: Collective Effects

* Energy	12 GeV	46 GeV
Skin depth of Cu chamber	0.849707 [mm]	0.849707 [mm]
Transverse resistive wall impedance	10.0034 [MΩ/m]	10.0034 [MΩ/m]
Resistive wall growth rate	19.1688 [/s]	5.00072 [/s]
Resistive wall power/beam	8.92167 [kW]	12.7078 [kW]
Threshold $Z_{\parallel}$ for coh. synchr. Oscillations	0.524547 [mΩ]	2.66779 [mΩ]
Threshold $Z_{\parallel}$ for μ-wave instability	0.0688374 [Ω]	0.56108 [Ω]
Threshold $Z_{\perp}$ for transverse mode-coupling	0.981236 [MΩ/m]	5.1142 [MΩ/m]

3.2.8 Beam Separation

The Z factory has two rings, like B factories [15,16]. Unlike in B factories, the energies of the two beams are the same, and magnetic separation is impossible. Near the interaction points, the two beams pass through common elements, in particular the low-β-quadrupoles, and possibly the common RF system. As in the proposed horizontal separation system for the VLLC [17], the separation is launched by electro-static separators next to a horizontally focusing quadrupole. It is enhanced by a double septum magnet half a period later, and completed at the next horizontally focusing quadrupole. Table 8 shows the parameters of the components at 45 GeV. The integrated separator field corresponds to less than that of two typical LEP separators [9]. I assume the same field in the septum magnet B≈0.25962 T as in VLLC [17], arrive at 14.2 m total length and about 400 A/mm linear current density, and about 7 mm septum thickness. Contrary to the VLLC, the length of the electro-static separators and septum magnets is not small compared to the length of the FODO periods. Hence, the calculation should be refined, also taking into account the thickness of insulation and vacuum chambers in the septum magnets.

Table 8 :Beam Separation Parameters

* Hor. separation at magnetic septum	10σ
Separator kick	0.349475 [mrad]
Hor. offset at magnetic septum	6.92374 [mm]
Integrated separator field	16.076 [MV]
* Half separation between rings	0.5 [m]
Septum kick	24.0442 [mrad]
Integrated septum field	3.68934 [Tm]

3.3 Polarization

The figure of merit M in a collider with polarized particles is given by the ratio of two integrals [8]:

$$M = \frac{\int_0^c L(t)P^2(t)dt}{\int_0^c L(t)dt} \tag{3.3}$$

Here *L(t)* and *P(t)* are the instantaneous luminosity and polarization, respectively, and *c* is the duration of a coast. Assuming that the RMS beam sizes at the interaction point are independent of time, the luminosity is simply proportional to the square of the bunch population *N*. I assume further that the only mechanism for particle loss is beam-beam bremsstrahlung, and express all times in units of the initial beam-beam bremsstrahlung lifetime τ_{bb} in Table 6. In this case the bunch population is given by

$$N(t) = \frac{N(0)}{1+t} \tag{3.4}$$

The polarization $P(t)$ builds up according to

$$P(t) = \hat{P}[1 - \exp(-t/p)] \tag{3.5}$$

Here, $\hat{P}$ is the equilibrium polarization in Table 4, and *p* is the polarization time in units of τ_{bb}. With (3.4) and (3.5), the integrals in (3.3) can be evaluated in closed form. The result is with the exponential integral *Ei*:

$$\begin{aligned} M/\hat{P}^2 = {} & [\exp(-2c/p)/c/p]\{-(\exp(c/p)-1)^2 p + 2\exp[(1+2c)/p](1+c) \\ & (-Ei(-1/p) + \exp(1/p)(Ei(-2/p) - Ei(-2(1+c)/p)) + Ei(-(1+c)/p))\} \end{aligned} \tag{3.6}$$

Figure 1 shows $M/\hat{P}^2$. In order to reach useful levels, the polarization time has to be less than about 10% of the beam-beam bremsstrahlung lifetime τ_{bb}, and the coast time *c* has to be a good fraction of τ_{bb}. Note that the luminosity drops to one half of its initial value after $c = \sqrt{2} - 1$. Table 9 summarizes the polarization parameters. Comparing the polarization parameters for a few polarization wiggler excitations between zero and the value listed in Table 4 shows that the best figure of merit *M* is achieved at that value. A stronger wiggler excitation might further improve M. The calculation ignores the depolarization due to the energy spread and orbit errors.

Let *f* be the fill time between two successive coasts, also measured in units of τ_{bb}. The average luminosity reaches a maximum when fill and coast time are related by $c = \sqrt{f}$ [18]. If $f\tau_{bb}$< 1.69 h, the luminosity averaged over the fill and coast times is at least one half of the peak value.

Table 9: Polarization Parameters

Beam-beam bremsstrahlung lifetime τ_{bb}	9.84998 [h]
Polarization time τ_p	0.292935 [h]
Coast time τ_C	4.07995 [h]
Equilibrium polarization $\hat{P}$	0.911999
Figure of merit M	0.713102

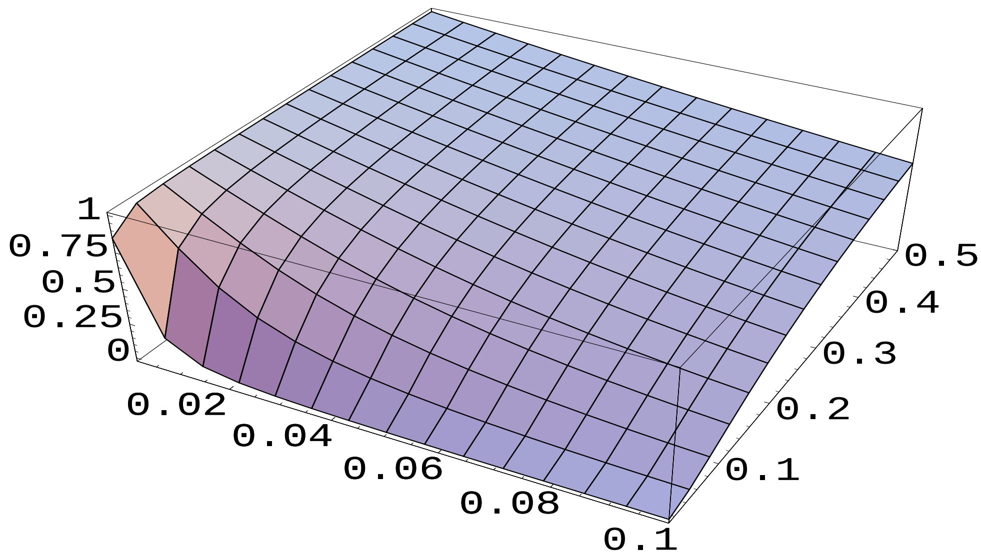

Figure 1: Figure of merit $M/\hat{P}^2$as a function of the polarization time on the left axis, and of the coast time on the right axis. Both times are measured in units of the initial beam-beam bremsstrahlung lifetime.

3.4 Conclusions

The concept of a Z factory in the VLLC injector with polarized *e+e-* beams is presented. The circumference *C* of such a collider is between one and two Tevatron circumferences. Wigglers are an essential ingredient of the concept. They make the bunches longer at injection, and reduce the risk of collective instabilities. They reduce the polarization time at collision energy. However, they are powerful sources of synchrotron radiation, and associated damage. The wiggler parameters should be refined. The vertical amplitude function at the interaction point is assumed to be β_y^*=40 mm. At this value, reaching a peak luminosity L=10^{33} cm^{-2}s^{-1} implies about 50 MW of RF power for the two beams. A lower value of β_y^* is very attractive. It could be exploited by using any intermediate method between two extremes: (i) At constant *L* and RF power, the circumference and the polarization time could be reduced. (ii) At constant circumference, RF power, and polarization time, *L* could be increased. Apertures and separation schemes have only been designed at the collision energy. In the discussion of polarization time, peak polarization and figure of merit, all depolarizing mechanisms, due to the momentum spread in the beam and orbit errors are ignored.

3.5 Acknowledgements

I should like to thank the organizers, T. Morrison, A. Tollestrup, G. Dugan, and J. Norem, for a stimulating workshop.

3.6 References

[1] T. Sen and J. Norem, A Very Large Lepton Collider in the VLHC Tunnel, to be published. (Preprint in Appendix 2 of this report)

[2] E. Keil, A Very Large Lepton Collider, http://wwwslap.cern.ch/~keil/Math/vllc.nb (2001).

[3] E. Keil, A High-Luminosity Z-Factory, http://wwwslap.cern.ch/~keil/Math/z0fact12km.nb (2001).

[4] E. Keil, Muon Storage Rings Design with Simple Mathematica Packages, CERN-SL-99-053-AP (1999).

[5] H. Grote and F.C. Iselin, The MAD Program, Version 8.16, User's Reference Manual, CERN/SL/90-13 (AP)(Rev. 4) (1995).

[6] C. Hill, this workshop.

[7] F. Barbarin, F.C. Iselin, J.M. Jowett, Particle Dynamics in LEP at Very High Energy, Proc. 4th European Particle Accelerator Conf. (World Scientific, Singapore 1994) 193.

[8]A. Blondel and J.M. Jowett, Wigglers for Polarization, CERN 88-06, Vol. 2 (1988) 216.

[9] The LEP2 Team, LEP Design Report -- Vol. III: LEP2, CERN-AC/96-01(LEP2) (1996)

[10] F. Ruggiero, Single-beam collective effects in the LHC, Particle Accelerators, **50** (1995) 83.

[11] J.T. Rogers, Collective Effects and Impedances in the RLHC(s), Cornell University CBN 96-14 (1996).

[12] B. Zotter, Current Limitations in LEP due to Vacuum Chamber Bellows, LEP Note 528 (1985).

[13] E. Keil, Synchrotron Radiation Dominated Hadron Colliders, Proc. Particle Accelerator Conference PAC'97 (Vancouver, 12-16 May 1997) 104.

[14] A.W. Chao, Physics of Collective Beam Instabilities in High Energy Accelerators (Wiley, New York 1993).

[15] An Asymmetric B Factory Based on PEP, SLAC-372 (1991).

[16] KEKB B-Factory Design Report, KEK Report 95-7 (1995).

[17] E. Keil, Beam Separation in a Very Large Lepton Collider, this workshop.

[18] K. Hübner and E. Keil, Optimization of average luminosity in pp and $\bar{p}$p colliders, IEEE Trans. Nucl. Sci. **NS-32** (1985) 1632.

4 BEAM DYNAMICS

4.1 Lattice Design of a Very Large Lepton Collider

Carol Johnstone and Tanaji Sen
Fermilab, Batavia, IL 60510

4.1.1 Luminosity

The desired luminosity is close to 10^{34} cm^{-2} sec^{-1} for this e^+e^- collider to produce sufficient number of physics events per year. At high energy where the synchrotron radiation power and the beam-beam tune shifts are limited, the luminosity is given by [1]

$$L = \frac{3}{16\pi r_e^{\,2}(m_e c^2)} \quad \frac{\xi_y P_T}{\beta_y^{\,*}} \quad \rho\gamma^{-3}$$

In a machine of given radius and at constant synchrotron radiation power P_T, the luminosity can be increased by increasing the beam-beam parameter ξ_y and by reducing β_y^*. The beam-beam limit per IP is known to scale with damping decrement τ_d from observations at LEP over many years. At an energy of 185 GeV in the VLLC, $\tau_d = 0.1$ and the expected limiting value $\xi_y \geq 0.1$ from the scaling law [1]. This limiting value depends on the number of interaction points in the ring, since the physical limit is on the total beam-beam tune shift. In this report we will assume $\xi_y = 0.14$ with two interaction points. If there is only a single high luminosity IP, then $\xi_y > 0.14$ should be feasible.

The lower limit on β_y^* is determined by several factors:

- The bunch length σ_s. If $\beta_y^* < \sigma_s$, there is a loss of luminosity due to the hour-glass effect.
- The aperture of the IR quads. The beam size in these quadrupoles is proportional to $1/\beta_y^*$.
- The chromaticity generated by the IR quadrupoles. The chromaticity is proportional to L/β_y^* where L is the distance to the center of the first quadrupole.

The last two factors in fact may limit β_y^* to a value greater than the bunch length – see [2] for an analytic estimate. The bunch length in the VLLC is 7 mm, here we will assume that $\beta_y^* = 1$ cm to meet the first constraint and design an Interaction Region which meets the other two constraints mentioned above.

With these parameter values, the luminosity reaches 7 x 10^{33} cm^{-2} sec^{-1} which is seven times greater than the luminosity with the parameter choices in [1]. Attaining a luminosity of 10^{34} cm^{-2} sec^{-1} might require that there be only a single IR and perhaps also a value of β_y^* closer to the bunch length. The design parameters of consequence are listed in Table 1.

Table 1: Selected beam parameters

Collider Storage Ring Geometry	racetrack
Maximum Storage Ring Energy	185 GeV
β_x^*/β_y^*	1 / 0.01 m
$\varepsilon_{x,rms}/\varepsilon_{y,rms}$ (unnormalized)	6.009 / 0.3005 nm-rad
Total synchrotron radiation power P_T	100 MW
Luminosity with ξ_y = 0.14	7.0 x 10^{33} cm^{-2} sec^{-1}
Luminosity with ξ_y = 0.20	10.0 x 10^{33} cm^{-2} sec^{-1}
$\delta p/p$(rms)	.1%

4.1.2 Overview of the Lattice

The ring geometry is a racetrack layout. The lattice has two circular arcs joined by two insertions, the experimental and RF insertions. The experimental insertion contains an IR at each end and the RF insertion contains the accelerating RF cavities. The long straight reserved between the two IRs and the opposing straight for RF are composed simply of 84 dipole-free arc FODO cells. The number of cells used was kept divisible by 4 to insure an integer phase advance across the long straights.

Although not yet designed, provision is made for injection, extraction, and other required functions such as beam scraping. Presently, the total number of cells in the ring is 855 (not counting the 8 dispersion suppression cells). A few of the arc cells are located not in the arcs, but between the final-focus and the straight section in the experimental insertion.

4.1.3 Arc Module

The parameters of the arc lattice are discussed in [1]. The phase advance per cell is chosen to be 90°. The cell length is determined by the equilibrium emittance while the quadrupole gradient is limited from above by the radiative beta-synchrotron effect. The optical and magnet parameters of the arc lattice are shown in Table 2. The beam pipe aperture is determined by requiring that the threshold current for the onset of the TMCI instability driven by the resistive wall impedance be a factor of two above the design current [3].

Table 2: Optics and magnet parameters of the arcs

Cell Length	226.345 m
Cell phase advance	90°
$\beta_x^{max}/\beta_y^{max}$	386 / 66 m
D_x^{max}/D_x^{min}	1.1 / 0.54 m
Number of arc cells	426
Dipoles:	
Length	15 m
Bend	0.61 mr
Field	.024 T
Half aperture	5 cm
Number in arc module	12
Quadrupoles:	
Length	1 m
Strength	77 T/m

4.1.4 Interaction Region design

The important parameters are β_y^* and L^* - the distance from the IP to the first quadrupole. We assume L^* = 3 m, a value that may be larger than required. Indeed if superconducting quadrupoles can be placed inside the detectors, then L^*~2 m may be feasible. All the design challenges associated with IR optics are eased and the luminosity delivered can be increased when L^* is reduced.

The low-beta function values at the IP are produced by two strong superconducting quadrupoles in the final focus with pole tip fields of 10 T. The full interaction region is symmetric under reflection about the interaction point (IP). The first quadrupole, 3 m from the IP, is vertically focusing to minimize the vertical beta function in that quadrupole and the corresponding vertical linear chromaticities. The next quadrupole is positioned primarily to establish an optimal IP to vertical sextupole phase advance in addition to a direct and efficient match to the arc module. The peak vertical beta function reaches 1.2 km and the peak horizontal value is less than 0.6 km. The vertical high beta value cannot be reduced significantly without reducing L^*. In fact placing the nearest quadrupoles within the detectors to reduce L^* may be a feasible option. This can be examined in a more aggressive design.

The gradients of these IR quadrupoles are limited from above by synchrotron radiation generated in these quadrupoles. This radiation should not cause particle losses via the radiative beta-synchrotron coupling effect and also not generate large backgrounds in the detectors. Energy lost by each particle to synchrotron radiation generated by traveling off-axis through a quadrupole can be estimated from

$$U = \frac{1}{2\pi} C_\gamma \frac{E^4}{\rho} \quad \frac{L_Q}{\rho}$$

Here L_Q is the length of the quadrupole, and ρ is the bend radius at a specified amplitude which we will take to be 1σ.

The important IR parameters are shown in Table 3. The maximum beam sizes are quite small compared to the beam-pipe aperture so there should be no constraints on the physical aperture, even allowing for closed orbit distortions.

Table 3: IR magnet and optics parameters

Distance from IP to first quadrupole L^*	3.0 m
Maximum gradient of IR quads	197.5 T/m
Length of quadrupoles F/D	0.45 m/ 1.23 m
Half aperture of IR quads	5 cm
Maximum β_x/β_y in IR	502 m/ 1180 m
RMS Beam size in the D quad σ_x/σ_y	0.41 mm/ 0.60 mm
RMS Beam size in the F quad σ_x/σ_y	1.74 mm/ 0.21 mm
Linear chromaticities of IR Q'_x/Q'_y	-11/ -71
Energy lost by a particle displaced $1\,\sigma_y$ in D quad	0.76 MeV
Energy lost by a particle displaced $1\,\sigma_x$ in F quad	2.3 MeV

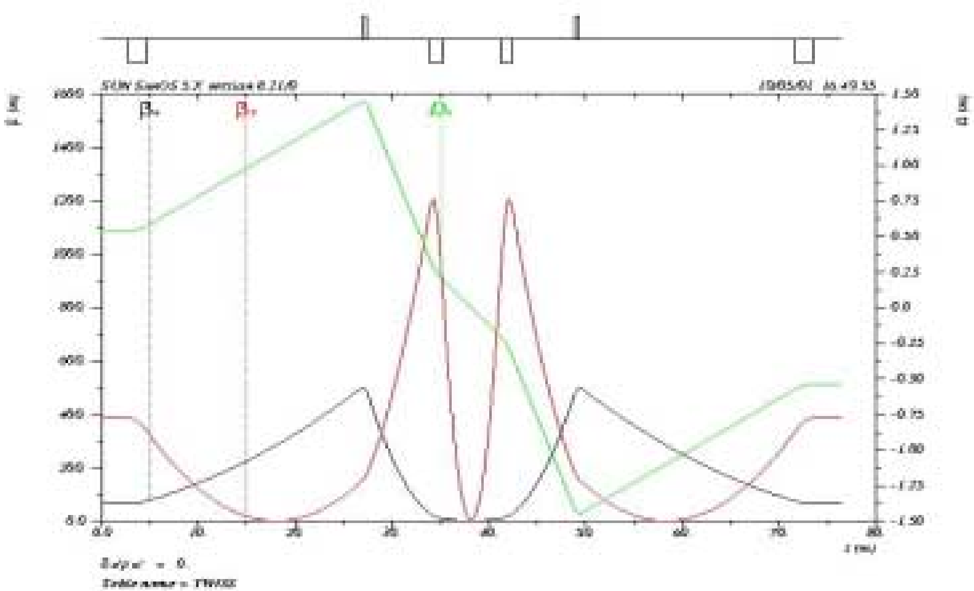

Figure 1: Plot of the beta functions and the horizontal dispersion in the IR section. Note that the dispersion at the IP is zero but the slope is non-zero.

4.1.5 Chromaticity compensation

To achieve the design luminosity, the β_y^* in the vertical must be only 1 cm, and the chromaticity increases as β_y^* decreases. The natural chromaticity of this IR is about –71 units in the vertical plane and requires careful chromatic correction to achieve broad momentum acceptance. With a horizontal β_x^* of 1m, the horizontal chromaticity due to the IR is only –11 units and requires no special treatment. Incorporating a second, identical IR makes the design inherently more difficult, since constructive/destructive interference of nonlinearities between each IR must be considered. The total linear chromaticities of the ring including both IRs, the RF straights and the arcs are –349 and –472 units in the horizontal and vertical planes respectively.

4.1.6 ***Interaction Region***

The large chromaticity (linear and nonlinear) of the IR requires a local chromaticity compensation in order to prevent a large chromatic beta mismatch from propagating into the rest of the ring. This in turn requires sextupoles placed close to the IR. Conventionally the dispersion and its slope are made to vanish at the IP to avoid an increase of the beam size due to momentum spread. With no other bends in the IR, the dispersion stays zero over the straight IR section. The nearest sextupoles to the IR must therefore be placed in the arcs adjacent to the IRs. Such an arrangement might suffice to locally compensate the chromaticity but we have not studied it in detail.

Here we pursue a more aggressive approach by allowing a non-zero dispersion slope at the IP but the dispersion at the IP is required to be zero. While it will increase the transverse size of the bunch tails, this should not significantly affect the luminosity as the bunch length is small. The dispersion at the location of the doublet quadrupoles now allows sextupoles to be placed adjacent to these quadrupoles and start the local compensation of chromaticity.

In order to create dispersion at the high-beta quadrupoles, a dispersion wave is allowed to propagate across the IR controlled only by the horizontal phase advance. The strength of the vertical quadrupole and the position of the horizontal high-beta quadrupoles were adjusted to give a horizontal phase advance of $\pi/2$ from the arcs. Since the IR effectively begins at an arc symmetry point, D_x' is 0. With a phase advance of $\pi/2$ to the IP, D_x then becomes 0 and D_x' nonzero at that point. To automatically reinstate the match to the arc, the full phase advance must be 2π. Since the IR is symmetric, there is another $\pi/2$ in phase advance to the beta-function match/symmetry point of the arc. If two empty (dipole free) 90° arc cells are then installed on the opposite side of the IR from the arc, the net phase advance from the end of the arc to that point is exactly 2π (at 185 GeV) and the dispersion returns to its full arc value of D_x = 0.537 m and D_x' = 0. m (hence an automatic match to the arc).

The next step in chromatic correction is to position the vertical sextupoles an odd multiple of $\pi/2$ away from the IP so that the vertical chromatic beta wave (propagating at twice the phase advance) due to the IR quads is out of phase with these sextupoles and therefore better compensated. In this design however, the horizontal phase advance across the IR is the primary constraint required to maintain the dispersion match. Still with proper choice of gradients, the phase advance to the first vertical sextupole outside the IR was maintained to an accuracy level of $2.96\pi/2$ on the arc side and $4.96\pi/2$ on the experimental insertion side, which has to include an additional π from the two empty arc cells. Additional quadrupoles can be inserted at a later stage to maintain the dispersion match and increase the robustness of the IR design to gradient and field errors.

The nonlinear chromaticity of the IRs was corrected by using two standard arc cells (with arc dipoles) on either side of the IR and using their two families of sextupoles (per plane) to minimize the total chromaticity of this extended IR insert up to 3rd order in the chromaticity. The same sextupole strengths are used in the two arc cells, which connect the IR to the arc and complete the IR insertion in terms of local correction.

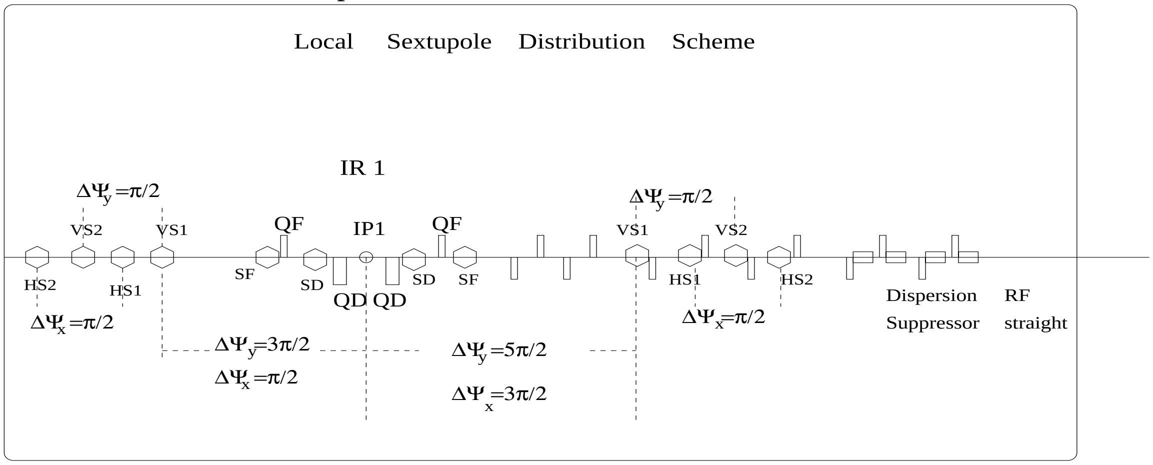

Figure 2: Sketch of the local sextupole distribution around IR1. On the left of the local sextupole HS2 are the regular arc cells while on the right is the long straight followed by IR2. The distribution of sextupoles around IR2 is mirror symmetric to the above distribution.

Figure 2 shows a sketch of the sextupole distribution used for local chromaticity compensation. Sextupoles SF and SD compensate the chromaticity of the doublet quadrupoles while VS1, VS2, HS1, HS2 are sextupoles that compensate the nonlinear chromaticities of the doublet and chromatically match the beta functions into the arc cell values. The phase advances that have to be kept constant are also shown in this figure.

4.1.7 RF straights

Simply canceling the linear chromaticity of these two straights using a single-family, global sextupole correction in the arcs did not appear to produce sufficient momentum acceptance. Instead, about a hundred cells flanking both the experimental and RF insertions have increased sextupole strengths to match the chromatic beta wave arising from the straight sections into the adjoining arcs.

4.1.8 The Complete Ring

Phasing not only of the two IRs relative to one another, but also with respect to the long straights proved imperative. The two IRs, inserted at either end of the experimental straight, were phased by an odd multiple of $\pi/2$ relative to each other. The sextupole strengths used in the complete ring are described in Table 4. Further refinement will help in decreasing the strengths and perhaps also the number of different families of sextupoles.

Table 4. Sextupole strengths for chromaticity correction.

Final-focus:	
vertical sextupole strength SD	991 T/ m^{-2}
horizontal sextupole strength SF	591 T/ m^{-2}
Arc cells (see figure 2):	
VS1/VS2 strength	6.4 T/ m^{-2}
HS1/HS2 strength	67 T/ m^{-2}
General Arc cells:	
sextupole strength: horizontal/ vertical	6.8 T/m^{-2} / 14.2 T/m^{-2}
RF chromatic correction cells:	
sextupole strength: horizontal/ vertical	9.9 T/m^{-2} / 20.4 T/m^{-2}

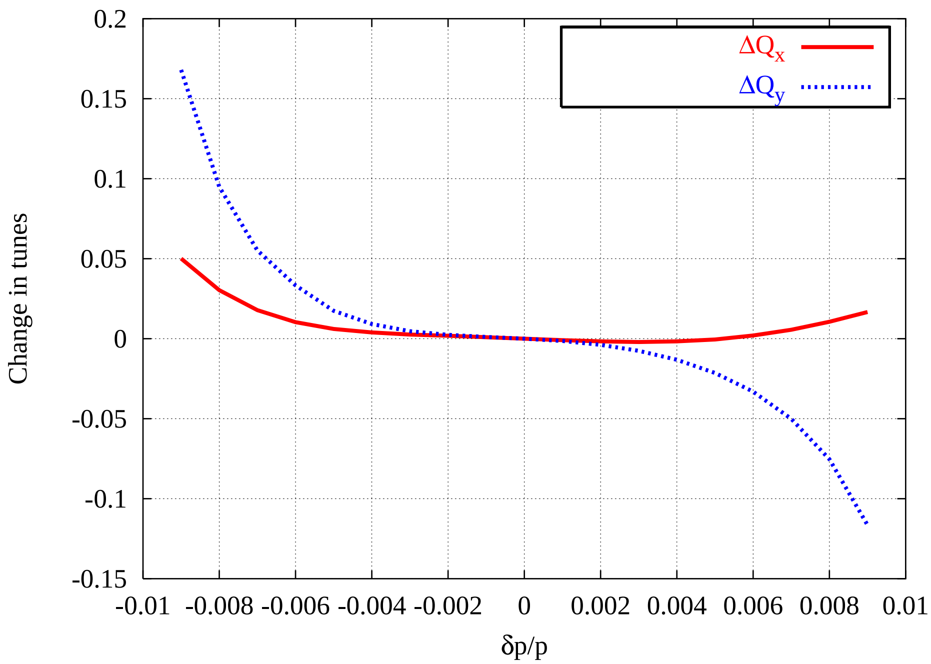

Figure 3: Dependence of the tune on the momentum deviation

Figure 3 shows the momentum dependence of the tune over a spread of ± 0.9%. As expected the vertical tune has a stronger dependence on the momentum. The nonlinear chromaticity correction has removed most of the quadratic dependence of Q_y on $\delta p/p$, leaving the cubic dependence as the dominant part. Over this range of momentum spread, the vertical tune changes by approximately ± 0.15 which may be tolerable. Figure 4 shows the momentum dependence of the relative change in β^{max} in the arcs. At the edges of the momentum aperture there is about a 40% beating in β_y compared to the values at zero momentum deviation and a much smaller 10% beating in β_x.

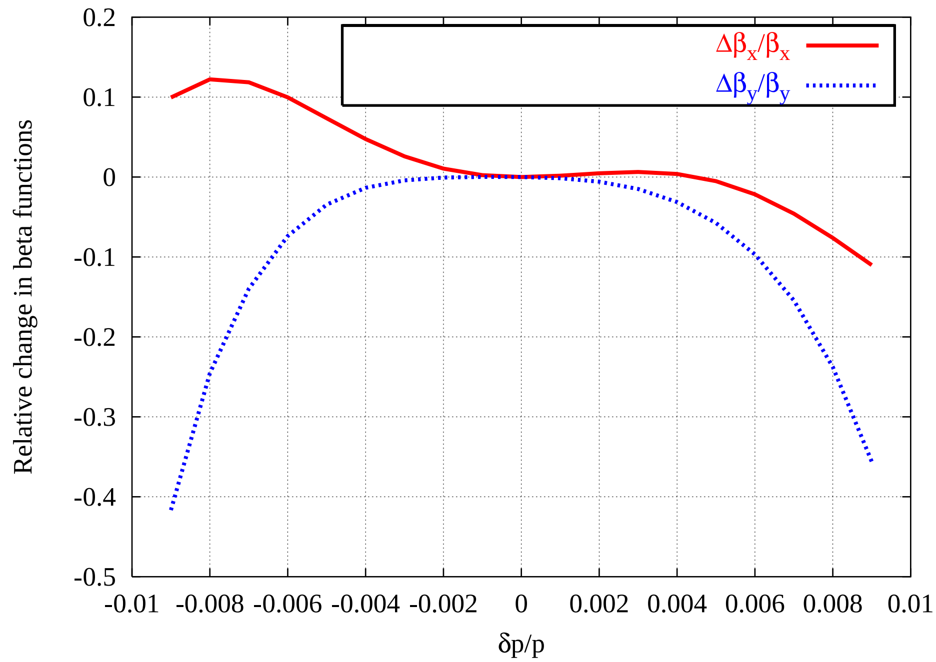

Figure 4: Dependence of the beta function in the arcs on the momentum deviation.

4.1.9 Summary

We have presented the outlines of an IR design which in principle achieves a luminosity of 7.0 x 10^{33} cm^{-2} sec^{-1} with β_x^*= 1.0m, β_y^*= 0.01 m and a beam-beam parameter of 0.14 and assuming two interaction regions. The luminosity could be raised to 10^{34} cm^{-2} sec^{-1} if there is a single interaction region and the beam-beam limit is raised to 0.20. We have shown that even with two IRs, the momentum acceptance is ± 0.9% which should be large enough for sufficient quantum lifetime. Refinement of the chromaticity compensation scheme may increase the momentum acceptance further.

Several other issues such as synchrotron radiation in the IRs, collimators and masking schemes, dynamic aperture, beam separation schemes etc. need to be considered to complete the IR design. These issues will be examined as the design study of this large e^+ e^- collider matures.

4.1.10 References

[1] T. Sen and J. Norem, A Very Large Lepton Collider in the VLHC Tunnel, to be published. (Preprint in Appendix 2 of this report)

[2] E. Keil, Frontiers of particle beams: Factories with e^+e^- rings, Lecture Notes in Physics 425, pg 106 (1994)

[3] G. Dugan, Beam stability requirements on the aperture, these proceedings

4.2 Chromatic Matching of the Interaction Region

Richard Talman

Laboratory of Nuclear Studies, Cornell University, Ithaca, NY 14850

4.2.1 ***Introduction***

The r.m.s. fractional energy spread, σ_δ, of the VLLC is expected to be about 0.001 which is similar to recent high energy LEP running, but roughly a factor of two higher than the fractional energy spread of existing e+/e- rings (for example σ_δ =0.0006 at CESR.) Since the lattice energy acceptance has to be roughly 10 σ_δ, the energy acceptance of VLLC has to be about $\pm 1\%$. This will be very hard to meet for the five-times-lower-than LEP β^* values needed for high luminosity. In preliminary studies, with rudimentary IR designs, with the distance from the IP to the first quad equal to 2 m, I have been unable to achieve energy acceptances greater than $5\sigma_\delta$ with β_y^*= 0.01m and β_x^*=1 m. My (half-hearted) attempts at local chromaticity compensation have not improved upon this[1]. Because this seems like the dominant lattice problem, I discuss it in some detail, in hopes of getting people to analyze the extent to which this limitation is fundamental. In the end one requires complicated lattice programs to get reliable designs, but once one has been reduced to this it is hard to learn what the fundamental limitations are.

4.2.2 ***Matching Algorithm***

Being preliminary and not fully worked out (as well as unsuccessful) the prescriptions for lattice matching to be discussed may or may not be consistent with prescriptions due to Montague and others. (B. W. Montague, LEP note 165, 1979.) For simplicity I started with a "minimally racetrack-shaped" ring with just one IR. The rest of the ring consisted of two arcs made from pure FODO cells. There is a single bend-free cell opposite to the intersection region, to make the gross geometry more symmetric. Chromaticity correction was performed by two families of sextupoles, with a sextupole superimposed on every arc quad. (Not surprisingly) this configuration turned out to be inadequate because the optical match of the IR to the regular arc cannot support a sufficient momentum bandwidth. The next simplest possibility seemed to be to exploit the first two cells of the regular arc for a local achromatic match of the vertical optics. This gave little improvement (though it was not investigated in any detail.)

The most promising scheme discovered so far has been to break the arcs into identical, repeated, 5-cell sectors, with vertical and horizontal sextupoles paired into achromatics. Letting "f/d" stand for focusing/defocusing half quads, "o" stand for drift, as is customary, also let ".F./.D." stand for focusing/defocusing sextupoles. Then the five cell achromatic sequence follows:

f.F.oddoffoddo.F.ffodd.D.offoddoffo.D.ddof (4.1)

---

[1] Some time after writing this, by improving the arc design rather than by improving the IR to arc match, I developed the lattice having β_y^*=0.02m described below, which is rather well behaved. So some of the following discussion is probably too pessimistic.

Since only 2/5 of the sextupoles have been retained, their strengths are increased by a factor 5/2. But, with phase advance per cell being approximately π /2 the sextupoles in (4.1) form non-interleaved achromats.

In terms of Twiss parameters, the one-dimensional transfer matrix from lattice point 1 (e.g. the IP) to lattice point 2 (e.g. the start of the FODO arc) is

$$M(2 \leftarrow 1) = \begin{bmatrix} \sqrt{\beta_2/\beta_1}(C+\alpha_1 S) & \sqrt{\beta_1\beta_2}S \\ \dfrac{-S(1+\alpha_1\alpha_2)+C(\alpha_1-\alpha_2)}{\sqrt{\beta_1\beta_2}} & \sqrt{\beta_2/\beta_1}(C-\alpha_2 S) \end{bmatrix} \tag{4.2}$$

where $S \equiv \sin\phi$, $C = \cos\phi$, where ϕ is the betatron phase advance through the section.

By symmetry, at the IP, $\alpha_{x1} = \alpha_{y1} = 0$, and these remain true independent of momentum offset δ . By starting and ending the regular arc with a half-quad one can, without loss of generality, assume that $\alpha_{x2} = \alpha_{y2} = 0$, though this relation will break down for $\delta \neq 0$. The full transfer matrix through the "demagnifying" output half of the intersection region therefore has the form

$$M = \begin{bmatrix} \sqrt{\dfrac{\beta_{x2}}{\beta_{x1}}}C_x & \sqrt{\beta_{x2}\beta_{x1}}S_x & 0 & 0 \\ \dfrac{-S_x}{\sqrt{\beta_{x2}\beta_{x1}}} & \sqrt{\dfrac{\beta_{x1}}{\beta_{x2}}}C_x & 0 & 0 \\ 0 & 0 & \sqrt{\dfrac{\beta_{y2}}{\beta_{y1}}}C_y & \sqrt{\beta_{y2}\beta_{y1}}S_y \\ 0 & 0 & \dfrac{-S_y}{\sqrt{\beta_{y2}\beta_{y1}}} & \sqrt{\dfrac{\beta_{y1}}{\beta_{y2}}}C_y \end{bmatrix} \tag{4.3}$$

This same form can be used for matching between any sectors that have the property that there are waists ($\alpha_{x1} = \alpha_{y1} = 0$) in both planes at both ends. (Both α-functions change sign at most quadrupoles, and for those quads there is a "waist" in both planes in the quad interior. Especially for thin quads it is not very restrictive to require these waists to coincide.) Supposing that both beta functions are known at both ends, the following equations can be derived by combining elements of $\boldsymbol{M}$:

$$\begin{aligned} M_{11}\beta_{x1} - M_{22}\beta_{x2} &= 0, \\ M_{33}\beta_{y1} - M_{44}\beta_{y2} &= 0, \\ M_{12} + \beta_{x1}\beta_{x2}M_{21} &= 0, \\ M_{34} + \beta_{y1}\beta_{y2}M_{43} &= 0. \end{aligned} \tag{4.4}$$

Other equations, such as

$$\beta_{x1}M_{11}M_{21} + M_{12}M_{22}/\beta_{x1} = 0, \quad M_{11}M_{12}/\beta_{x2} + \beta_{x2}M_{12}M_{22} = 0 \tag{4.5}$$

plus the corresponding y equations can be derived but, being quadratic in the matrix elements, and hence giving higher order polynomials in the unknowns, they are less amenable to solution by algebraic solvers that work with polynomials, such as MAPLE, which is what I use. Presumably either set of four equations could be used to fix four parameters of a sector under study.

(Though it may not really be necessary) it is standard to have zero dispersion through the "IR sector". It will now be shown that the chromatic compensation must be outside this sector. i.e. chromatic correction without dispersion is impossible. (This is probably obvious to experts.)

Since only drifts and quads are contemplated, the elements M_{ij} are polynomial functions of the quad strengths q_i and drift lengths L_i. In principle, if the four parameters $\beta_{x1}, \beta_{x2}, \beta_{y1}$, and β_{y2} are given, and four of the q_i and L_i are free, then the variables can be determined to match the lattice. In practice it is not nearly this simple, as there may be multiple solutions, or worse, none at all. Some or all of the matches may have complex strengths or complex or negative lengths. Nevertheless, with a certain amount of trial and error, Eqs. (4.4) can be used to design matching sections, though it may be necessary to introduce intermediate points and complete the match sector by sector.

Supposing that the q_i and L_i of the IP-to-regular-arc-region have been determined, the matrix $\boldsymbol{M}$ is known, and satisfies Eqs. (4.4) and (4.5). It would be nice if these equations could be satisfied identically in δ. But this is clearly impossible. (See, for example, in Steffen, *High Energy Beam Optics*, proof of the impossibility of designing fully momentum-independent bend-free sections.) One often concentrates on compensating just the ``chromaticities" $Q'_x = dQ_x/d\delta$ and $Q'_y = dQ_y/d\delta$ and one expects the chromaticities due to the IR section to be comparable to the chromaticities due to the rest of the ring. It is obligatory (both because of fast head tail instability and avoidance of resonances) that $Q'_x \approx Q'_y \approx 0$. The simplest way to achieve this is to increase the strengths of the arc sextupoles. Though this cuts proportionally the dynamic acceptance the arcs would have had all by themselves, this acceptance is still adequate in any cases I have looked at.

I believe that the dominant phenomenon that limits off-momentum acceptance is the "chromatic beta-mismatch". Because low-beta IR's are "highly tuned", the $q_i/(1+\delta)$ momentum dependence of the quadrupoles causes a mismatch which launches a δ-dependent "beta-wave". This beta-wave can seriously reduce the off-momentum aperture.

Let us suppose that the arc sextupoles have been tuned to make the ring achromatic in the sense mentioned two paragraphs back.[2] This means that the arcs themselves are "over-compensated", so their periodic Twiss functions depend on δ. In particular their "period matched" end values are $\alpha_2(\delta)$ and $\beta_2(\delta)$(both planes). Fortunately, because the chromaticity compensation is spread over the entire arcs, this dependence will be fairly mild---it is the extreme chromatic dependence of the IR sections that really matters. A certain amount of iteration will be required to achieve self-consistency, but let us therefore assume that values of the derivatives with respect to δ ,

$$\beta'_{x2}, \beta'_{y2}, \alpha'_{x2}, \alpha'_{y2} \tag{4.6}$$

[2] Following tradition, the phrase "chromatic correction" will be used ambiguously.

are known. The most ideal IR design imaginable would exactly compensate these dependencies to make the IP values $\alpha_1(\delta)$ and $\beta_1(\delta)$ constant (both planes) at the end of dispersion-free IR sectors. We expect this to be impossible, but it seems unnecessary to be quite so greedy. We could afford to let $\beta_{x1}(\delta)$ and $\beta_{y1}(\delta)$ continue to depend on δ. Even if these quantities vary substantially over the momenta present in the beam, the resulting beam distortion at the IP could be acceptable, and might cause little loss of luminosity. However, closure of the lattice off-momentum requires $\alpha_{x1}(\delta)$ and $\alpha_{y1}(\delta)$ to be independent of δ; that is

$$\alpha'_{x1}(\delta) = \alpha'_{y1}(\delta) = 0. \tag{4.7}$$

If these are satisfied the lattice would presumably stay approximately matched over a substantial range of δ even if the β's vary δ. Unfortunately, it will now be shown that this extra "freedom" is illusory.

The formulas by which Twiss functions evolve from 1 to 2 are

$$\begin{aligned} \beta_2 &= M_{11}^2\beta_1 - 2M_{11}M_{12}\alpha_1 + M_{12}^2\frac{1+\alpha_1^2}{\beta_1}, \\ \alpha_2 &= -M_{11}M_{21}\beta_1 + (M_{11}M_{22} + M_{12}M_{21})\alpha_1 - M_{12}M_{22}\frac{1+\alpha_1^2}{\beta_1} \end{aligned} \tag{4.8}$$

It is now more convenient to proceed backwards through the demagnifying section, and for this we require the inverse matrix

$$M^{-1} = \begin{bmatrix} M_{22} & -M_{12} & 0 & 0 \\ -M_{21} & M_{11} & 0 & 0 \\ 0 & 0 & M_{44} & -M_{34} \\ 0 & 0 & -M_{43} & M_{33} \end{bmatrix} \tag{4.9}$$

The elements of this matrix can then be substituted into the inverses of Eqs. (4.8);

$$\begin{aligned} \beta_1 &= M_{22}^2\beta_2 + 2M_{22}M_{12}(-\alpha_2) + M_{12}^2\frac{1+\alpha_2^2}{\beta_2}, \\ \alpha_1 &= M_{22}M_{21}\beta_2 + (M_{22}M_{11} + M_{12}M_{21})(-\alpha_2) + M_{12}M_{11}\frac{1+\alpha_2^2}{\beta_2} \end{aligned} \tag{4.10}$$

In this step the signs of α_2 have been reversed since the evolution is back through the demagnifying section.

On-momentum (δ=0), Eqs. (4.10) are presumably already satisfied (in both planes) because the lattice is assumed to be already matched. It is the first order momentum dependence we are interested in. Furthermore, as explained above, we are only requiring the α matches. In particular, we demand that conditions (4.7) be satisfied:

$$
\begin{aligned}
&\frac{d}{d\delta}(M_{22}M_{21}\beta_{x2} - (M_{22}M_{11} + M_{12}M_{21})\alpha_{x2} + M_{12}M_{11}\frac{1+\alpha_{x2}^2}{\beta_{x2}} = 0,\\
&\frac{d}{d\delta}(M_{44}M_{43}\beta_{y2} - (M_{44}M_{33} + M_{34}M_{43})\alpha_{y2} + M_{34}M_{33}\frac{1+\alpha y_{x2}^2}{\beta_{y2}} = 0
\end{aligned}
\tag{4.11}
$$

Since this is two fewer conditions than full achromaticity would require, we can remain hopeful that a bend-free IR can be designed that satisfies them. Note that this design is not quite the same as what is usually called “local chromaticity correction”, and which employs sextupoles and dispersive regions in the intersection region. The only elements being used here are linear.

All quantities appearing on the left hand sides of Eqs. (4.11) are known. The matrix elements M_{ij} are all known as polynomials in the q_i, the L_i and δ . The on-momentum α_2's and β_2's are known from the matched lattice design and their slopes are known, according to Eq. (4.6). The operative word “known” may be a bit too strong here since, as mentioned already, a certain amount of iteration will be required. The Twiss parameters and their first order momentum derivatives will be known from whatever lattice fitting software is being used.

If the IR section were being matched to general arcs, according to Eqs. (4.11) , formulas for the α-functions would also be required. But since we are fitting to a pure FODO arc (neglecting the perturbing influence of the far straight) the arc α-functions vanish at the IR boundaries. Conditions Eqs. (4.11) then reduce to

$$
\begin{aligned}
&\frac{d}{d\delta}(\tilde{M}_{22}\tilde{M}_{21}\tilde{\beta}_{x2} + \tilde{M}_{12}\tilde{M}_{11}\frac{1}{\beta_{x2}}) = 0,\\
&\frac{d}{d\delta}(\tilde{M}_{44}\tilde{M}_{43}\tilde{\beta}_{y2} + \tilde{M}_{34}\tilde{M}_{33}\frac{1}{\beta_{y2}}) = 0
\end{aligned}
\tag{4.12}
$$

The tildes on the $\tilde{M}_{ij}$, $\tilde{\beta}_{x2}$ and $\tilde{\beta}_{y2}$ indicate that all quadrupole strength parameters q_i have been replaced by $q_i/(1+\delta) \approx q_i(1-\delta)$ in the formulas expressing the matrix elements in terms of the quadrupole strengths and drift lengths; no sextupole strengths enter here (as yet.) For a match to the regular arc, valid to linear order in δ, the factors $\tilde{\beta}_{x2}$ and $\tilde{\beta}_{y2}$ have to agree with the values in Eq. (4.6). (Because of the weak chromaticity of the arcs, just treating $\tilde{\beta}_{x2}$ and $\tilde{\beta}_{y2}$ as independent of δ may be adequate.)

One can note that the validity of Eqs. (4.12) would imply that the second of Eqs. (4.5) is momentum-independent (to leading order.) Also, if points 1 and 2 are reversed in the above argument, one obtains an equation equivalent to the first of Eqs. (4.5) (in lowest order.) So requiring Eqs. (4.12) amounts to requiring that Eqs. (4.4) hold not only for δ =0 but also to linear order in δ . This means that demanding a momentum-independent α match implies also a momentum-independent β match. As suggested above, such a match is probably impossible. My failure to find a configuration of quads and drifts satisfying Eqs. (4.12), even after considerable effort, is consistent with this (and is why I performed the above analysis.)

Let us therefore contemplate placing sextupoles in the end cell or cells of the FODO arcs, in order to satisfy conditions (4.12). Since the simplest form of achromat uses identical sextupoles separated by phase advance of π , it seems sensible to use two cells, each with phase advance π /2. Before doing this let us calculate the sextupole strengths needed to compensate the arc chromaticity.

4.2.3 Thin Lens, Pure FODO, Regular Arcs

For simplicity we assume thin lenses everywhere, even though, ultimately, thick lens formulas have to be applied, especially to the quadrupoles adjacent to the IP. Since the sextupole strengths S_1 and S_2 are determined only implicitly, they have to be determined to adjust the overall chromaticities to zero (or whatever nearby values are called for.) Let us assume that each FODO cell starts and ends with a vertically focusing half quad of strength q_1 (which is negative), the middle quad strength is q_2 (which is positive), and the half-cell lengths are l. The horizontal transfer matrix through the first half-cell is

$$\begin{pmatrix} 1 & 0 \\ -q_2 & 1 \end{pmatrix}\begin{pmatrix} 1 & l \\ 0 & 1 \end{pmatrix}\begin{pmatrix} 1 & 0 \\ -q_1 & 1 \end{pmatrix} = \begin{pmatrix} 1-q_1 l & l \\ -q_1 - q_2 + q_1 q_2 l & 1-q_2 l \end{pmatrix} \tag{4.13}$$

Momentum dependence can be built into this formula by the replacements $q_i \to q_i/(1+\delta)$.

Sextupoles can also be incorporated if they are superimposed on the quadrupoles. Decomposing the horizontal displacement as $x = x_\beta + \eta_x \delta$, the angular deflection caused by a quadrupole of strength q_i with a sextupole of strength S_i superimposed, would be

$$\begin{aligned} \Delta x' &= \left(\frac{q_i}{1+\delta} + S_i \eta_x \delta\right) x + \text{terms to be dropped} \\ &\approx (q_i + (S_i \eta_x - q_i)\delta) x \,. \end{aligned} \tag{4.14}$$

Let us therefore define the dimensionless parameters

$$\tilde{q}_1 = (q_1 + (S_1 \eta_{x1} - q_1)\delta) l, \qquad \tilde{q}_2 = (q_2 + (S_2 \eta_{x2} - q_2)\delta) l \tag{4.15}$$

which “wrap” or “hide” the functional dependencies on δ, the S's, η_x and l.

The horizontal transfer matrix through the full cell is given by

$$\begin{aligned} M_x(\delta) &= \begin{pmatrix} 1-2\tilde{q}_1 - 2\tilde{q}_2 + 2\tilde{q}_1\tilde{q}_2 & 2(1-\tilde{q}_2) l \\ 2(-\tilde{q}_1 - \tilde{q}_2 + \tilde{q}_1\tilde{q}_2)(1-\tilde{q}_1)/l & 1-2\tilde{q}_1 - 2\tilde{q}_2 + 2\tilde{q}_1\tilde{q}_2 \end{pmatrix} \\ &\equiv \begin{pmatrix} \cos\mu_x(\delta) & \beta_x(\delta)\sin\mu_x(\delta) \\ -\dfrac{\sin\mu_x(\delta)}{\beta_x(\delta)} & \cos\mu_x(\delta) \end{pmatrix} \end{aligned} \tag{4.16}$$

Here $\mu_x(\delta = 0)$ is the on-momentum horizontal phase advance per cell. The β-functions are obtained from $-M_{12}/M_{21}$,

$$\beta_{x1} = l\sqrt{\frac{1-\tilde{q}_2}{1-\tilde{q}_1}}\sqrt{\frac{1}{\tilde{q}_1+\tilde{q}_2-\tilde{q}_1\tilde{q}_2}}, \qquad \beta_{y1} = l\sqrt{\frac{1+\tilde{q}_2}{1+\tilde{q}_1}}\sqrt{\frac{1}{-\tilde{q}_1-\tilde{q}_2-\tilde{q}_1\tilde{q}_2}},$$
$$\beta_{x2} = l\sqrt{\frac{1-\tilde{q}_1}{1-\tilde{q}_2}}\sqrt{\frac{1}{\tilde{q}_1+\tilde{q}_2-\tilde{q}_1\tilde{q}_2}}, \qquad \beta_{y2} = l\sqrt{\frac{1+\tilde{q}_1}{1+\tilde{q}_2}}\sqrt{\frac{1}{-\tilde{q}_1-\tilde{q}_2-\tilde{q}_1\tilde{q}_2}}. \tag{4.17}$$

The phase advances are given by

$$\sin^2\frac{\mu_x(\delta)}{2} = \tilde{q}_1+\tilde{q}_2-\tilde{q}_1\tilde{q}_2, \qquad \sin^2\frac{\mu_y(\delta)}{2} = -\tilde{q}_1-\tilde{q}_2-\tilde{q}_1\tilde{q}_2. \tag{4.18}$$

To use relations (4.15) it is necessary to have formulas for the η_x functions;

$$\eta_{x1} = \frac{(1-|q|\,l/2)l\,\Delta\theta}{|q|^2\,l^2}, \qquad \eta_{x2} = \frac{(1-|q|\,l/2)l\,\Delta\theta}{|q|^2\,l^2} \tag{4.19}$$

For equal tunes these reduce to

$$\eta_{x1} = \frac{(1-q_2 l/2)l\,\Delta\theta}{(\sin^2\mu_x/2)}, \qquad \eta_{x2} = \frac{(1-q_1 l/2)l\,\Delta\theta}{(\sin^2\mu_x/2)} \tag{4.20}$$

Since these are already the coefficients of terms first order in δ, it is not necessary to allow for their momentum dependence. This means their values can simply be copied from the output of a lattice program. In fact, since the same comments can be made about the sextupole strengths, it will only be necessary to know the products $S_1\eta_{x1}$ and $S_2\eta_{x2}$. The most rudimentary, most local, form of chromatic correction is to choose

$$S_1 = \frac{q_1}{\eta_{x1}}, \qquad S_2 = \frac{q_2}{\eta_{x2}} \tag{4.21}$$

though, of course, this compensates only the arc chromaticity. Since η_{xi} is (almost) always positive, S_i will normally have the same sign as q_i. The following derivatives enter Eqs. (4.12):

$$\frac{d\tilde{q}_1}{d\delta} = (S_1\eta_{x1}-q_1)l, \qquad \frac{d\tilde{q}_2}{d\delta} = (S_2\eta_{x2}-q_2)l. \tag{4.22}$$

In these formulas the coefficients $S_1\eta_{x1}-q_1$ and $S_2\eta_{x2}-q_2$ can be regarded as the excess due to compensating also the IR chromaticity.

4.2.4 Preliminary Lattice Design and Performance

Using these formulas, I have succeeded in matching the above-mentioned β_y^*=0.01 m, β_x^*=1 m at the IP so as to satisfy Eqs. (4.4), with the free space from IP to first quad being 1 m. (More precisely the distance from the IP to the center of the first quad was taken to be 2 m.) The lattice functions are shown in Figures 1 and 2 and the lattice parameters are shown on the last page of this section. The on-momentum optics in this lattice are satisfactory and the peak beta functions near the IP are no greater than the maximum beta's in the arcs. Unfortunately the momentum acceptance is not quite 0.5%, which is a factor of two too small. Since my efforts at local chromaticity compensation have never increased this to more than 0.6%, I do not describe them in greater detail.

Because of these difficulties a more conservative IR design, having β_y^*=2.0 cm with distance from the IP to center of first quad was tried. The on-momentum 256 turn acceptance, for two-family chromaticity correction is shown in Fig. 3 which was obtained by tracking using TEAPOT. The axes are $x_{\max}/\sqrt{\beta_x}$ and $y_{\max}/\sqrt{\beta_y}$ which permits direct comparison with the advertised VLLC emittances, which are $\varepsilon_x = 0.83\times10^{-8}$ m and $\varepsilon_y = 0.0415\times10^{-8}$m. The 1 sigma points are at 0.91×10^{-4} m$^{1/2}$ horizontally and 0.20×10^{-4} m$^{1/2}$ vertically. The on-momentum acceptance of this lattice is therefore satisfactory.

The acceptance of the same lattice with chromaticity compensation performed using the five-cell noninterleaved achromat scheme (4.1) is shown in Figure 4. The behavior of the five-cell scheme was so far superior to the two-family scheme, that the δ -dependence was investigated over a $\pm1\%$ range. This is shown in Fig 4.

This good acceptance and near-satisfactory energy acceptance was observed in spite of a bad IR to arc mismatch $\beta_y{}^{peak}(0.008)\big/\beta_y{}^{peak}(0) = 1.7$ which can surely be improved. Since an r.m.s. bunch length less than 1cm is probably impractical, the lattice that has been described is very nearly adequate as it is. Of course, as well as seeking such improvement, a thick lens design is required.

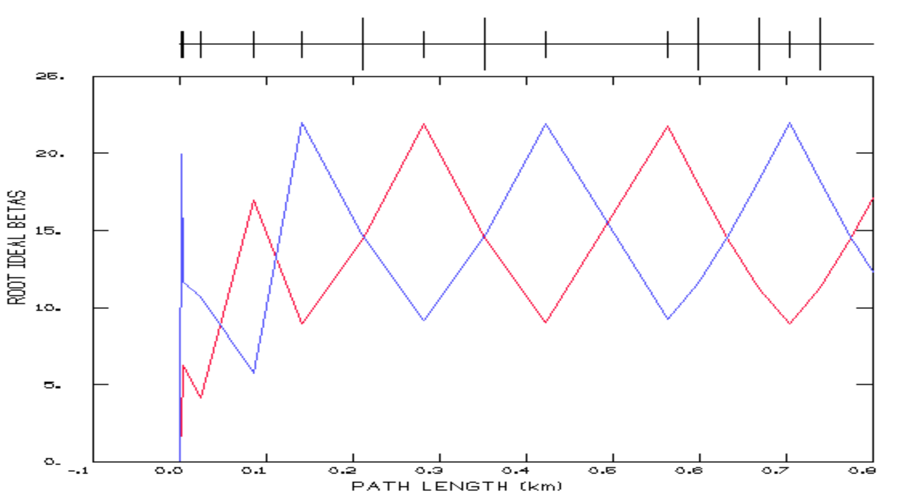

Figure 1: IR region β-functions. β_y^*=1.0cm. β_x^*=1.1m. Long hash marks above the graph mark dipole centers. Short hash marks are at thin quad locations. Dispersion suppression is performed by dipoles centered at 0.21km and 0.35km as well as missing magnets in the gap from 0.45km to 0.57km. First half cell of regular FODO arc runs from 0.57km to 0.705km.

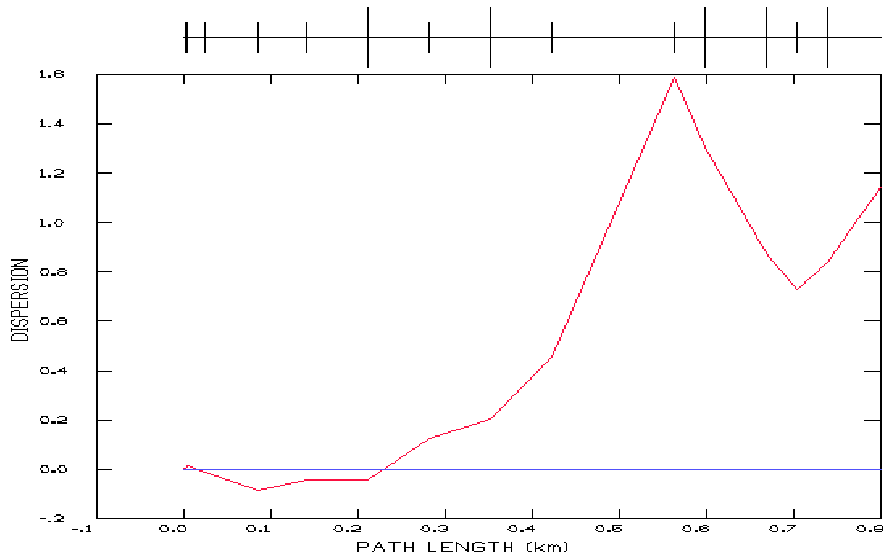

Figure 2: Dispersion (not quite tuned up) in same region as in Figure 1.

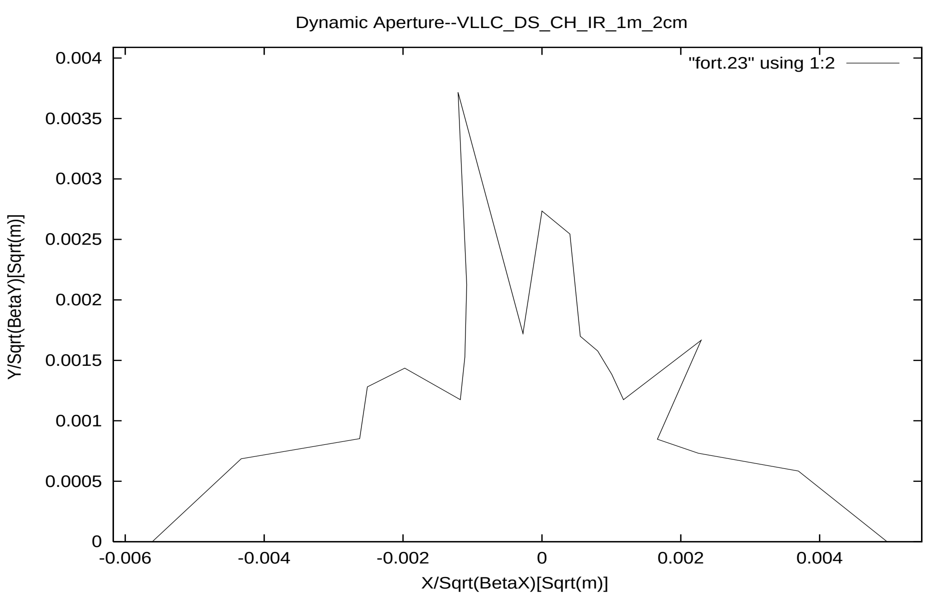

Figure 3: On-momentum dynamic aperture VLLC with two-family chromatic correction. TEAPOT 256 turn tracking. β_y^*=2.0cm**,** L_1=1m.

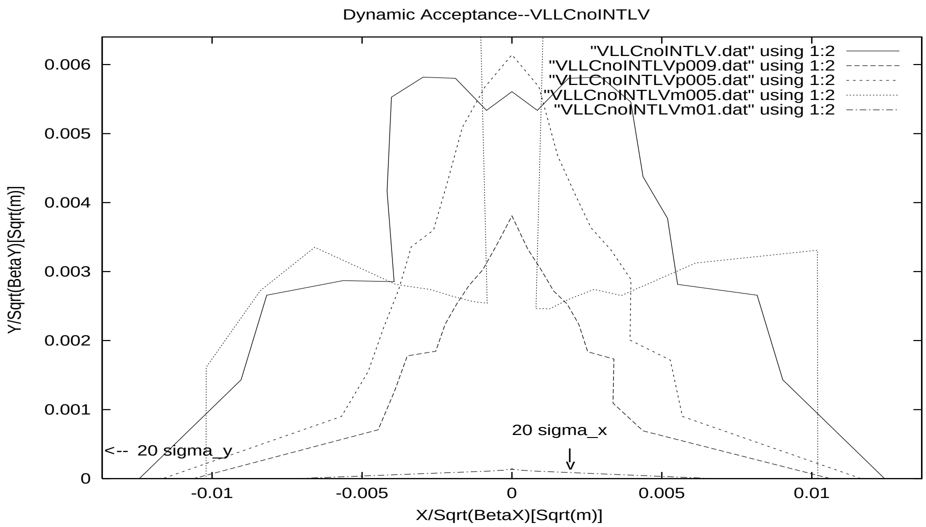

Figure 4: On-momentum dynamic aperture VLLC with five-cell,, noninterleaved, chromatic correction. TEAPOT 256 turn tracking. β_y^*=2.0 cm, L_1=1 m. The different curves correspond to δ=-0.01, -0.005, 0, 0.005, 0.009; they are identified by the key; e.g. ``p009'' indicates δ =0.009.

4.2.5 Appendix: Thin lens lattice parameters, IR through first arc cell

0 2.00001
1 -0.75 # quadrupole qir1p 2.000014087E+00
0 1.66632
1 0.423896 # quadrupole qir2p 3.666334838E+00
0 20.2816
1 0.00363442 # quadrupole qir3p 2.394789653E+01
0 2.818e-05
1 -0.0174589 # quadrupole qir1 2.394792471E+01
0 60.8067
1 0.0235631 # quadrupole qir2 8.475460230E+01
0 56.1151
1 -0.0136822 # quadrupole qir3 1.408697202E+02
0 2.81e-05
1 -0.0049597 # quadrupole quadhf 1.408697483E+02
0 70.4348
2 8.268589126E-08 # sbend dsbend1 2.113045339E+02
0 70.4348
1 0.00507469 # quadrupole quadvf 2.817393196E+02
0 2.81e-05
1 0.00507469 # quadrupole quadvf 2.817393477E+02
0 70.4348
2 8.268589126E-08 # sbend dsbend2 3.521741333E+02

```
0 70.4348
1 -0.0049597 # quadrupole quadhf 4.226089190E+02
0 2.81e-05
1 -0.0049597 # quadrupole quadhf 4.226089471E+02
0 140.87
1 0.00507469 # quadrupole quadvf 5.634784842E+02
0 2.81e-05
1 0.00507469 # quadrupole quadvf 5.634785123E+02
0 35.2174
2 5.465392191E-08 # sbend bendh 5.986959220E+02
0 70.4348
2 5.465392191E-08 # sbend bendh 6.691306849E+02
0 35.2174
1 -0.0049597 # quadrupole quadhf 7.043480946E+02
0 0 # 704.3480946
```

4.3 Experience with low β* values in LEP

Karel Cornelis
CERN, Geneva, Switzerland

Abstract
A summary of the operational experience in LEP with different β_y^* values.

4.3.1 Nominal insertion optics

During most of its life time LEP was operated with a kind of standard insertion optics for physics. The β_y^* was nominally 5 cm and $\beta_x^*$was 1.25 m. The first quadrupoles on each side of the IP were at about 3 m away (the position of the first quads was not exactly the same for all IP's). These quadrupoles were 2 m long, superconducting and sitting on a girder that was sticking them inside the detector. In the rest of the text they will be called QSC's.

4.3.2 Physics at 45 GeV

During the Z^0 running the $\beta_y^*$was brought to 3 cm on several occasions. In fact there were no fundamental problems to run the machine in this way. The reason why this optics was not used systematically was more pragmatic and political. The real β^* value and the exact longitudinal position of the beta-waist was found to be very sensitive to small errors in the QSC's. Errors in the order of a few 10^{-4} were sufficient to shift the waist by some cm's and to change the β^* by several mm. This could lead to luminosity differences of more than 30% between the four experiments, which was unacceptable for the physics community. In fact, the machine was so sensitive to small changes in the QS0, that after a session of several iterations on beta-measurements and corrections in all the IP's, the real β^* were found to be 4.2 cm instead of the theoretical 5 cm. This sensitivity increases for lower β^* and it was decided for practical reasons to stick to the nominal 5 cm.

The horizontal β^* was at some point increased from 1.25 m to 2.5 m. The reason for this was background in the experiments. This change allowed some horizontal collimators in the high beta region to be put in closer.

4.3.3 Running at 100 GeV

During the period when LEP was running at 100 GeV the horizontal β^* was put back to 1.25 m. Since the machine was not beam-beam limited, this was a straightforward gain in luminosity.

On one occasion the vertical β^* was squeezed to 4 cm without any problem. At that time it was more important to squeeze out the last bit of GeV rather than to optimize the luminosity and the effort was abandoned.

4.3.4 Conclusions

LEP has been running most of its history with a β_y^* of 5 cm. A β_y^* of 3 cm was certainly possible but was not used because of reproducibility problems.

4.4 Beam stability requirements on the aperture

Gerald Dugan

Laboratory of Nuclear Studies, Cornell University, Ithaca, NY 14850

4.4.1 Introduction

The transverse mode-coupling (TMCI) instability is expected to set the limit on the maximum single-bunch current in the machine. Broad-band impedances drive this instability. The single-bunch current threshold I_{th} associated with a collection of broad band impedances whose transverse loss factors are $k_{\perp,i}(\sigma_s)$, is given by

$$I_{th} = \frac{8 f_s}{\sum_i \beta_i k_{\perp,i}(\sigma_s)} \frac{E}{e} \tag{4.23}$$

in which f_s is the synchrotron frequency, E is the beam energy, e is the electron charge, σ_s is the rms bunch length, and β_i is the beta-function at the location of the ith impedance. The linear dependence of the threshold current on energy indicates that this instability is most severe at injection.

In LEP, the dominant sources of transverse broadband impedance are the RF cavities and the bellows. The loss factor for a single superconducting RF cavity, capable of delivering 10 MV to the beam, is about 2.3 V/pC/m at σ_s = 1 cm. The loss factor for a single bellows is about 0.41 V/pC/m at σ_s= 1 cm.

In the VLLC, these sources of broadband impedance will be present also. The required RF voltage is about 4500 MV, which implies about 450 10 MV RF cavities. Assuming the cavities are similar to those of LEP, the total loss factor due to the RF will be 1035 V/pC/m. The design of the vacuum chamber should minimize the number of bellows. In LEP, there is one bellows every 10 m; if this design were followed for the VLLC, there would be 22,800 bellows, and the total loss factor due to the bellows would be 9350 V/pC/m, dominating that of the RF system. We assume here that the vacuum chamber can be designed so that the impedance of the bellows is much less than that of the RF system. For example, one bellows every 900 meters would give a total transverse loss factor of 100 V/pC/m.

4.4.2 Resistive Wall Impedance

In the VLLC, in addition to these sources of impedance, the large radius of the ring results in a significant contribution to the broad-band impedance coming from the resistive wall of the vacuum chamber itself. Written in terms of the transverse impedance, $Z_\perp(\omega)$, rather than transverse loss factor, the single-bunch current threshold I_{th} associated with a broad band impedance is given by

$$I_{th} = \frac{16\pi Q_s}{\beta \left|\mathrm{Im}\left[Z_{\perp,eff}\right]\right|} \frac{E}{e} \frac{\sigma_s}{C} \tag{4.24}$$

in which β is the beta function at the impedance, C is the machine circumference, and the effective impedance is given by integrating $Z_\perp(\omega)$ over the bunch spectrum. Assuming a Gaussian bunch, we have

$$\mathrm{Im}\left[Z_{\perp,eff}\right] = \frac{\int_{-\infty}^{\infty} d\omega \exp\left(-\frac{\omega^2\sigma_s^2}{c^2}\right)\mathrm{Im}[Z_\perp(\omega)]}{\int_{-\infty}^{\infty} d\omega \exp\left(-\frac{\omega^2\sigma_s^2}{c^2}\right)} \qquad (4.25)$$

For a cylindrical vacuum chamber, the resistive wall transverse impedance is given by

$$Z_\perp(\omega) = \frac{cC}{\pi}\left(1 - i\,\mathrm{sgn}(\omega)\right)\frac{1}{b^3}\sqrt{\frac{\mu_0\rho}{2|\omega|}} \qquad (4.26)$$

in which b is the vacuum chamber radius, and ρ is the resistivity of the vacuum chamber material.

For an *elliptical* chamber, the effective transverse impedance is a rather complicated subject (see, e.g., L. Palumbo and V. Vaccaro, **Nuovo Cimento** 89 A(1985), p 243-256). Here, we will gloss over that complexity. For an elliptical vacuum chamber, in which a and b are the horizontal (semi-major) and vertical (semi-minor) axes, we will simply make the replacement $\frac{1}{b^3} \to \frac{1}{2}\left(\frac{1}{b^3} + \frac{1}{a^3}\right)$ in Eq.(4.26), giving the approximate result

$$Z_\perp(\omega) \approx \frac{cC}{2\pi}\left(1 - i\,\mathrm{sgn}(\omega)\right)\left(\frac{1}{a^3} + \frac{1}{b^3}\right)\sqrt{\frac{\mu_0\rho}{2|\omega|}}. \qquad (4.27)$$

In the future, the exact results, which can be found the paper cited above, should be used for a more accurate estimate.

Inserting Eq. (4.27) into Eq. (4.25) and doing the integration gives

$$\mathrm{Im}\left[Z_{\perp,eff}\right] = \frac{\Gamma\left(\frac{1}{4}\right)}{\sqrt{\pi}}\mathrm{Im}[Z_\perp\left(\frac{c}{\sigma_s}\right)] \approx -\frac{\Gamma\left(\frac{1}{4}\right)}{2\sqrt{2\pi^3}}\left(\frac{1}{b^3} + \frac{1}{a^3}\right)C\sqrt{c\mu_0\sigma_s\rho} \qquad (4.28)$$

Using Eq. (4.28) in Eq. (4.24) gives for the threshold current:

$$I_{th} \approx \frac{64\sqrt{2\pi^7}}{\Gamma\left(\frac{1}{4}\right)}\sqrt{\frac{\sigma_s}{c\rho\mu_0}}\frac{1}{\left(\frac{C}{a}\right)^3 + \left(\frac{C}{b}\right)^3}Q_x Q_s \frac{E}{e} \qquad (4.29)$$

in which we have replaced β with $\langle\beta\rangle = \frac{C}{2\pi Q_x}$. In engineering units, for ρ = 1.7x 10^{-8} Ω-m (copper), Eq. (4.29) is

$$I_{th}[\mathrm{mA}] \approx 54.2 \frac{\sqrt{\sigma_s[\mathrm{cm}]}}{(C[\mathrm{km}])^3} \frac{1}{\left(\frac{1}{b[\mathrm{cm}]}\right)^3 + \left(\frac{1}{a[\mathrm{cm}]}\right)^3} Q_x Q_s E[\mathrm{GeV}] \tag{4.30}$$

This expression shows that the threshold current shrinks with the cube of the machine circumference, if the other parameters are fixed. For a machine with a circumference of the VLLC, 10 times that of LEP, this is a factor of 1000 reduction in the threshold current. Although the threshold current due to the resistive wall is quite large in LEP, for the VLLC it is much reduced and is comparable to that due to the RF cavities. Because of the strong dependence on the vacuum chamber radius, this effect sets a fairly stringent lower limit on the chamber radius. From Eq. (4.29), it can be seen there is a weak dependence on the material of the vacuum chamber (a thin copper coating on the chamber wall, with a thickness of order the skin depth at $\omega = c/\sigma_s$ helps). Increasing the bunch length at injection (with wigglers), increasing the injection energy, and using a large synchrotron tune at injection may also raise the threshold current.

4.4.3 Threshold current estimates

We consider two cases: injection and collision energy. Table 1 gives the parameters used in each case. For both cases, the chamber wall is taken to be copper, the circumference to be 233 km, and the betatron tune to be $Q_x = 215$. The aspect ratio of the elliptical vacuum chamber is fixed at $a/b = 2.5$.

Table 1: Parameters used in injection and collision to calculate the threshold currents

Parameter	**Collision**	**Injection**
Beam energy	184 GeV	45 GeV
Bunch length	0.7 cm	1.0 cm
Synchrotron tune	0.115	0.13

Fig. 1, the threshold current at the injection energy, due to the resistive wall impedance, is calculated from Eq. (4.30), as a function of the vacuum chamber half-height, using the parameters cited above and given in Table 1. The solid line at 0.2 mA represents the design bunch current (0.1 mA) times a safety factor of 2. As the figure shows, the threshold current can be kept above 0.2 mA for chamber half-heights in excess of about 3.5 cm.

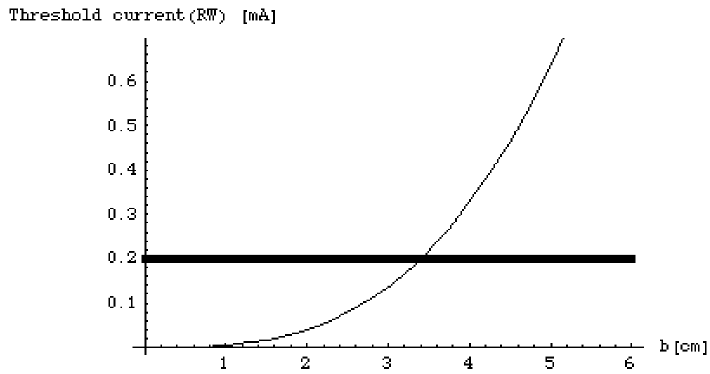

Fig. 1.Threshold current at the injection energy, due to the resistive wall impedance, calculated from Eq. (4.30), as a function of the vacuum chamber half-height.

However, the resistive wall impedance is not the only impedance in the machine. As noted above, there will also be contributions to the threshold current from the bellows and RF impedances. The total threshold current is $I_{th,tot}$, given by

$$I^{-1}_{th,tot} = I^{-1}_{th,bellows} + I^{-1}_{th,RF} + I^{-1}_{th,RW} \tag{4.31}$$

in which the threshold currents for the bellows and for the RF are given by Eq. (4.23) and that for the resistive wall from Eq.(4.30). We have assumed, as noted above, the same impedance as for the LEP RF cavities, with 450 cavities, and one LEP-style bellows every 900 meters.

In Fig. 2, the total threshold current at injection energy is calculated from Eq.(4.31), as a function of the vacuum chamber half-height. The solid line at 0.2 mA again represents the design bunch current (0.1 mA) times a safety factor of 2. Now we see that the threshold current can be kept above 0.2 mA only for chamber half-heights in excess of about 4.8 cm.

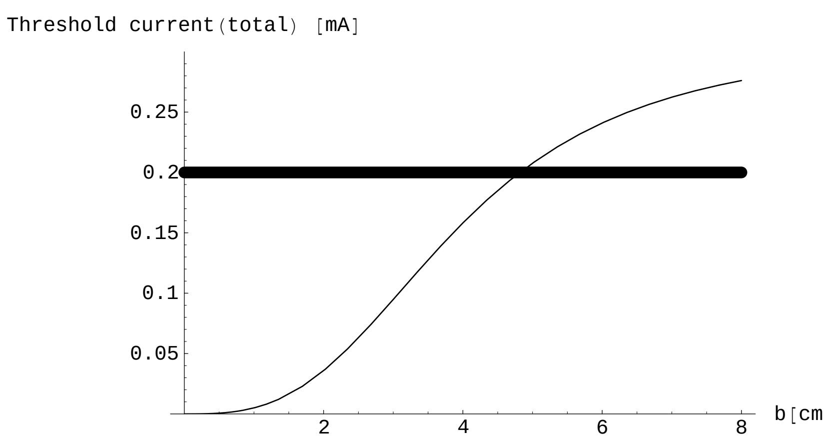

Fig. 2.Total threshold current at injection energy, calculated from Eq. (4.31), as a function of the vacuum chamber half-height.

Fig. 3 shows the total threshold current at collision energy. At this higher energy, the threshold current is increased, so that a chamber half-height of only about 2.5 cm would suffice for a safety factor of two.

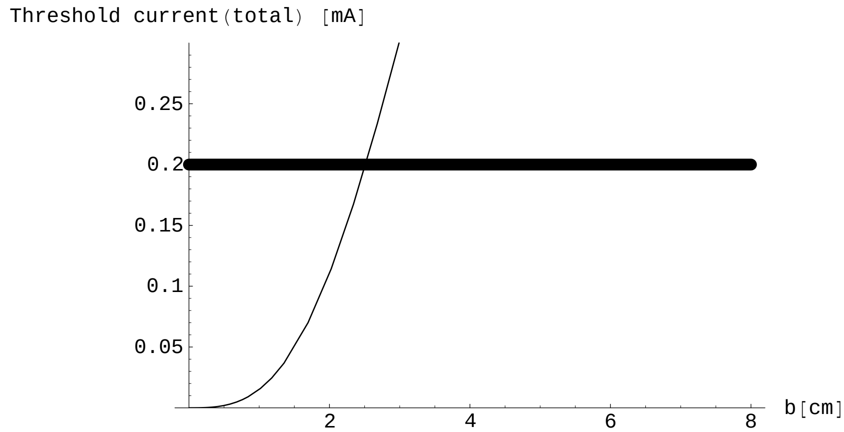

Fig. 3.Total threshold current at collision energy, calculated from Eq. (4.31), as a function of the vacuum chamber half-height.

4.4.4 Conclusions

The conclusion is then the following. We have assumed an elliptical chamber, with a thin copper coating, and a horizontal-to-vertical aspect ratio of 2.5, with beam parameters as shown in Table 1. At 45 GeV injection energy, a vacuum chamber half-height of at least 4.8 cm is required to allow a safety factor of 2 between the threshold current for the TMCI instability and the required bunch current (0.1 mA) in the machine.

4.5 Distribution of the RF System in a Very Large Lepton Collider

Eberhard Keil
CERN, Geneva, Switzerland

Abstract

The consequences for the beam dynamics are discussed of concentrating the radio-frequency accelerating system of a very large circular e^+ e^- collider VLLC in a few places around the circumference. As a specific example, a VLLC with four long straight sections with RF systems and possibly interaction points and four arcs is used. At 184 GeV beam energy, each RF system accelerates the two beams by about 1 GeV, and causes energy variations between ± 0.27% around the circumference. By arranging the RF systems symmetrically around the interaction points, the center-of-mass energies there are all equal to twice the beam energy. In a VLLC model without low-β insertions, the effects of this sawtooth energy variation on the mismatch of the horizontal orbit and dispersion, and the amplitude functions are all rather small.

4.5.1 Introduction

This brief note contains a discussion of the consequences of concentrating the radio-frequency accelerating system in a few places around the circumference of a very large circular collider VLLC [1]. The purpose of the RF system is compensating the synchrotron radiation losses that amount to about 4 GeV on a turn, or about 2.174% of the beam energy E=184 GeV. I assume that the RF systems are installed in the long straight sections close to the interaction points, and that the dispersion vanishes there. There are several very good reasons for this choice. In the specific context of this note, it avoids exciting synchro-betatron resonances by the RF system. The long straight sections contain the same focusing arrangement as the arcs, i.e. FODO cells with length L_p, phase advance μ in units of 2π, and focal length f of the quadrupoles as shown in Table 1.

4.5.2 Layout of a super-period

A super-period starts and finishes at an interaction point IP. Next to the IP are low-β insertions and associated matching sections, that match the low-β insertions to the FODO lattice in the rest of the VLLC. I have not studied these sections, and simply replaced them by three FODO cells for the purposes of this note. The RF systems are installed in the drift spaces between the quadrupoles of the following FODO cells. Each half cell of the lattice contains 40 RF cavities, that operate at about 400 MHz, are about 2 RF wavelengths long, and have about 6.7 MV peak voltage. The remainder of the long straight section is used for separating the two beams into two different magnetic channels [3]. Installing the RF system in the straight section common to the two rings halves the number of cavities, but does not change the RF power needed. Installing the RF system symmetrically around the interaction points has two beneficial effects: (i) it minimises the distance between bunches in the VLLC, and hence maximizes their number, and (ii) it ensures that the center-of-mass energies of the beam-beam collisions have the nominal value by symmetry [4]. Fig. 1 shows the layout of a FODO cell with the RF system. The arcs in a super-period are surrounded by dispersion suppressors. The far end of a super-period contains FODO cells for beam separation, an RF system, the matching and low-β insertions.

The number of super-periods must be at least two, resulting in a VLLC of racetrack shape. The RF systems in the two long straight sections must each accelerate the beams by about 2 GeV. The energy offsets at the entrances and exits of the arcs are then about ±1 GeV, or about ±0.54% of the beam energy.

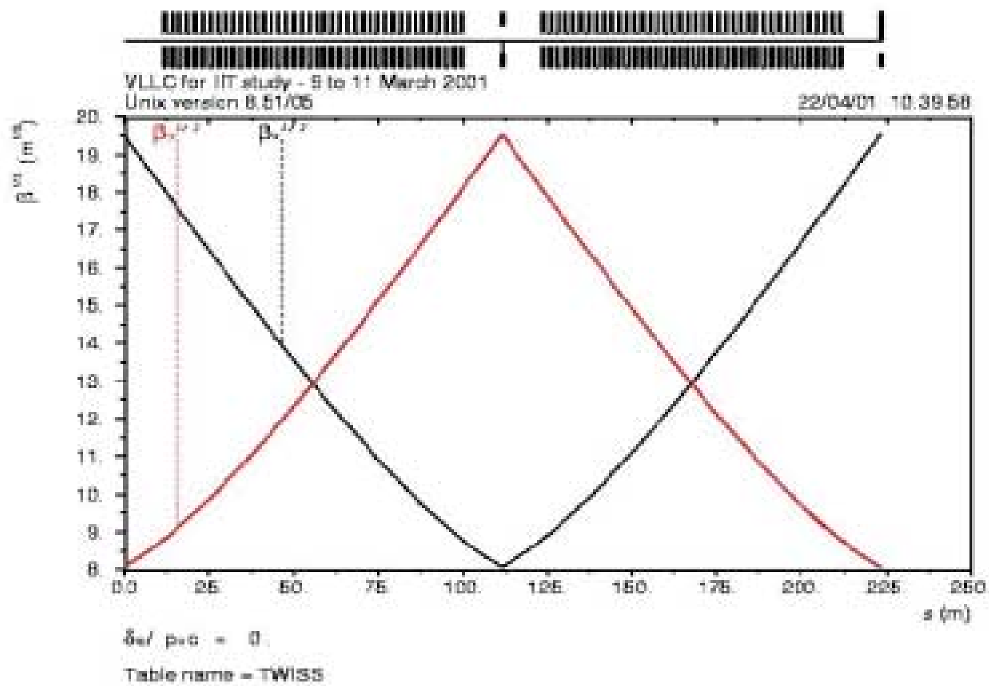

Figure 1: Schematic layout of a lattice cell with 40 RF cavities in each half cell, and orbit functions $\sqrt{\beta_x}$ and $\sqrt{\beta_y}$

4.5.3 RF System Design

The total peak RF voltage V_{RF} follows from the requirement that the quantum lifetime must at least be τ_q = 24 h. The calculation [2] yields V_{RF} =4.27326 GV. If the whole RF system consisted of cavities similar to the super-conducting LEP cavities, each having about 10 MV peak accelerating voltage, at least about 432 cavities would be needed in total.

Table 1: VLLC Parameters

Collision energy E	184 [GeV]
FODO period length L_p	223.464 [m]
Phase advance $\mu/2\pi$	0.25
Focal length of quadrupoles f	$\pm$ 79.3774 [m]
Max. amplitude function β_x	383.268 [m]
Max. horizontal dispersion D_x	1.12054 [m]
Frequency of RF system f_{RF}	399.989 [MHz]
Number of RF cavities	640
Peak RF voltage V_{RF}	4273.26 [MV]
Stable phase angle $\varphi_s/2\pi$	0.308234
Relative bucket height	$5.98466 \cdot 10^{-3}$

4.5.4 Orbital effects

In my calculations, I assume that the VLLC has four super-periods, and resembles a square with rounded corners. I install one lattice period with 80 RF cavities on either side of all four centers of long straight sections, whether they are interaction points or not. In this case, the total number of RF cavities is 8×80=640, and the peak accelerating voltage is 6.68 MV. Fig. 2 shows the relative momentum error δ, and demonstrates the variation of the beam energy along the orbit in sawtooth fashion. The relative momentum error δ vanishes near the interaction points at either end of the super-period. It rapidly increases in the RF system to the left of the graph, reaching about 0.5 GeV or about 0.27%, stays constant in the rest of the long straight section, and then drops through the arc. In the long straight section at the right edge of the graph, it stays constant again, and rises steeply in the second RF system. Fig. 3 shows the horizontal orbit offset along a super-period, if I do not take steps to adapt the strengths of the dipoles to the variation of the beam energy. The peak value of x is comparable to the RMS beam radius in a horizontally focusing quadrupole in the arcs $\sigma_x \approx 2$ mm. Note the little orbit wiggles in the long straight sections at either edge of the graph. One can argue that an orbit correction system will re-center the horizontal orbit, by adding bending power at the entrance of the arcs where $\delta>0$, and subtracting bending power at their exits where $\delta<0$. If there are horizontal correctors next to every horizontally focusing quadrupole, then their strength must be about 0.0123 Tm for only correcting the energy sawtooth. This strength corresponds to a 0.5 m long corrector with the field of a standard arc dipole.

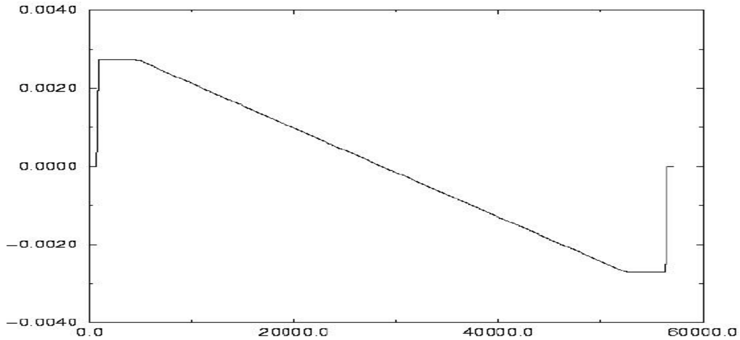

Figure 2: Relative momentum error δ along a super-period of VLLC.

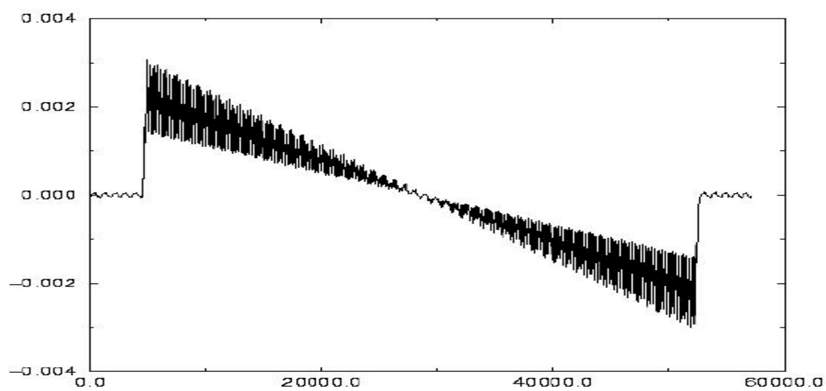

Figure 3: Horizontal orbit offset *x* in metres along a super-period of VLLC

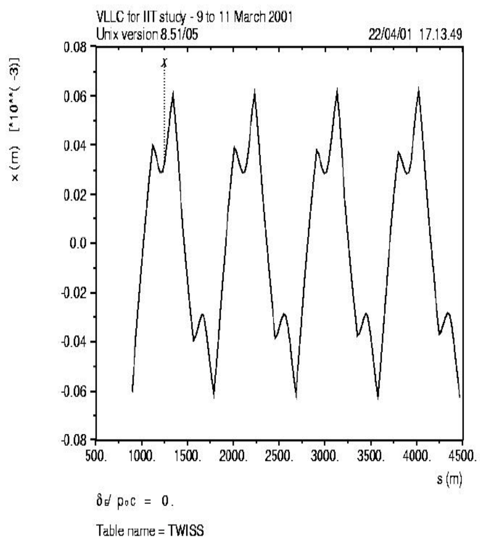

Figure 4: Horizontal orbit offset *x* in meters along 16 lattice periods in the long straight section of VLLC

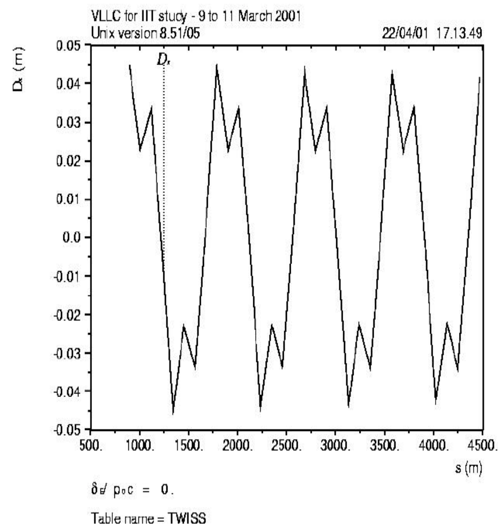

Figure 5: Horizontal dispersion D_x in meters along 16 lattice periods in the long straight section of VLLC

Figs. 4, 5, 6, and 7 show closer views of the horizontal orbit offset *x*, the horizontal dispersion D_x, and the orbit functions $\sqrt{\beta_x}$ and $\sqrt{\beta_y}$ through 16 lattice periods in the long straight section between the RF system and the arc. All these functions repeat themselves since the phase advance through a lattice period is $\pi/2$, the former two four times, the latter two eight times. The horizontal offset *x* in the long straight sections is about 60 μ-m at most, only about 3% of the RMS beam radius. The dispersion D_x in the long straight sections is about 40 mm at most, less than 4% of the arc value. The beating of $\sqrt{\beta_x}$ and $\sqrt{\beta_y}$ is also surprisingly small, only a few percent. It is caused by the chromaticity correction.

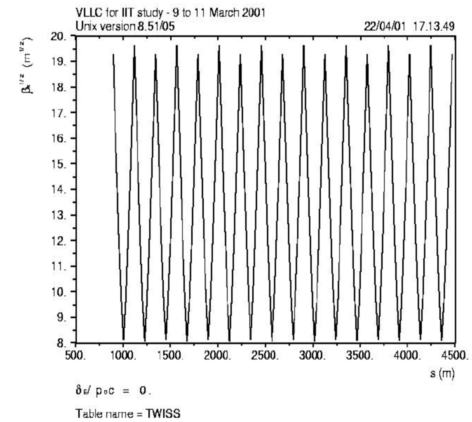

Figure 6: Horizontal orbit function β_x along 16 lattice periods in the long straight section of VLLC

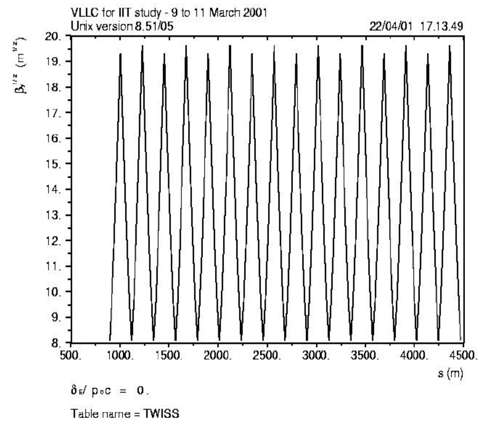

Figure 7: Vertical orbit function β_y along 16 lattice periods in the long straight section of VLLC.

4.5.5 Conclusions

The consequences for the beam dynamics are discussed of concentrating the radio-frequency accelerating system of a very large circular e^+e^- collider VLLC in a few places around the circumference. As a specific example, a VLLC with four long straight sections with RF systems and possibly interaction points and four arcs is used. At 184 GeV beam energy, each RF system accelerates the two beams by about 1 GeV, or 0.54% of the beam energy, and causes energy variations between ±0.27% around the circumference. By arranging the RF systems symmetrically around the interaction points, the center-of-mass energies there are all equal to twice the beam energy. In a VLLC model that does not contain low-β insertions, the effects of this sawtooth energy variation on the mismatch of the horizontal orbit, the horizontal dispersion, and the amplitude functions are all rather small. In a VLLC with only two long straight sections and two half-circular arcs they would be twice as large.

The VLLC parameters are computed in my *Mathematica* notebook [2]. It writes a short file with data for MAD [5]. In turn, MAD does the matching for elements of finite length, computes the orbit parameters, and prepares the graphs. This scheme allows an easy adaptation to changes in the VLLC parameters.

4.5.6 References

[1] T. Sen and J. Norem, A Very Large Lepton Collider in the VLHC Tunnel, to be published. (Preprint in Appendix 2 of this report)

[2] E. Keil, A Very Large Lepton Collider, http://wwwslap.cern.ch/~keil/Math/vllc.nb, (2001).

[3] E. Keil, Beam Separation in a Very Large Lepton Collider, CERN-SL-Note-2001-017 (AP) (2001)

[4] J.M. Jowett, Consequences of less symmetrical locations of the polarization wigglers, LEP Note 616 (1988)
[5] H. Grote and F.C. Iselin, The MAD Program, Version 8.16, User's Reference Manual,CERN SL/90-13 (AP) Rev.4 (1995).

4.6 Beam Separation in a Very Large Lepton Collider

Eberhard Keil
CERN, Geneva, Switzerland

Abstract

A scheme is described for feeding the two beam of a very large circular e^+ e^- collider (VLLC) into two separate magnetic channels. Electrostatic separators launch the separation. Their excitation is chosen such that half a lattice period later the two beams are separated enough to be in separate apertures of magnetic septa which complete the separation another half lattice period later.

4.6.1 Introduction

This brief note contains a design of the initial stages of beam separation in a very large circular e^+e^- collider VLLC [1]. The purpose of beam separation is feeding the two beams into the two separate magnetic channels of the two-ring design of VLLC. I assume that the separation is launched in the straight section close to the interaction point. It contains the same focusing arrangement as the arcs, i.e. FODO cells with length L_p, phase advance μ in units of 2π, and focal length f of the quadrupoles as shown in Table 1. I design the separation scheme at the operating energy, E, in the horizontal plane, for the normalized horizontal emittance ε_x. I do not consider any other operating energy. In the calculations, I assume that the lengths of all components vanish.

4.6.2 Electrostatic Separators

I launch the separation with an electrostatic separator that is placed next to a horizontally focusing quadrupole. Its integrated field is adjusted such that the beams have offsets of $\pm N_\sigma$ RMS beam radii σ_D at the next downstream, horizontally defocusing, quadrupole. The deflection angle φ_e and integrated electric field El_e are

$$\varphi_e = 2N_\sigma\sigma_D \;/ L_p, \qquad\qquad El_e = \varphi_e E$$

Table 1 shows the parameters of the electrostatic separation. A typical LEP2 separator [3] has 4 m long electrodes, and a nominal field of 2.5 MV/m over a gap of 0.11 m. Hence, its integrated field is 10 MV. About two typical LEP2 separators are all that is needed for the VLLC. Horizontal separators have high-voltage plates on either side of the beam aperture. In order to avoid beam-induced sparking, they must be protected from the synchrotron radiation of nearby quadrupoles either by masks or by a slot in the plates along the median plane. It does not seem excessively difficult to ask for a larger electrostatic separation, and thus to obtain a current sheet of finite thickness in the magnetic septum.

4.6.3 Magnetic Septa

The defocusing quadrupole enhances the slope of the trajectories. Downstream from it are d.c. magnetic septum magnets with opposite vertical fields on either side of a current sheet. They add enough to the slope of the trajectories, such that they are in separate magnetic channels at the next, horizontally focusing, quadrupole. For a half separation d_m between the two channels at that quadrupole, the deflection angle φ_m in that septum magnet and its integrated magnetic field $B\,l_m$ are, with the speed of light c, and the electrostatic separation x_s at the defocusing quadrupole with focal length f

$$\varphi_m = \frac{2(d_m - x_s)}{L_p} - (\varphi_e + \frac{x_s}{f}), \qquad Bl_m = \varphi_m E / c$$

The bracket in the numerator takes into account that the beams are already electro-statically separated at the magnetic septum. The bracket in the second term takes into account the slope of the beams in front of the defocusing quadrupole and its enhancement by it. Table 1 shows the parameters of the magnetic separation. The quadrupoles could be particularly slim and/or staggered such that the beam pipe for the other beam passes just along the outer edge of a quadrupole with little perturbation to the optics. If I assume that the total length of magnetic septa is about 10 m, I need a field B_m ≈ 0.25692 T. Neglecting the permeability of the steel yoke, this implies a linear current density j ≈ 400 A/mm in the septum. Note that this value is twice that in a septum magnet with a single aperture and the same field. Septum magnets with about 60 A/mm^2 current density are operated d.c. in the SPS [4]. Hence, the thickness of the septum needed here is less than 7 mm.

Table 1: VLLC Beam Separation Parameters

Collision energy E Normalized emittance ε_x FODO period length L_p Phase advance $\mu/2\pi$ Focal length of quadrupoles f	184 [GeV] 2.72039 [mm] 223.464 [m] 0.25 ±79.3774 [m]
Hor. RMS beam radius at F quadrupole σ_F Hor. RMS beam radius at D quadrupole σ_D Deflection angle in separator φ_e Integrated separator field El_e Electrostatic separation at D quadrupole x_s	2.03053 [mm] 0.88136 [mm] 78.5125 [μrad] 14.4463 [MV] 8.81355 [mm]
Half distance between channels d_m Deflection angle in magnetic septum φ_m Integrated septum field Bl_m	0.5 [m] 4.18602 [mrad] 2.5692 [Tm]

4.6.4 Conclusions

A scheme is described that horizontally separates the two beams in a VLLC, consisting of two rings. Its length is about a period length. Table 1 shows all parameters. The separation is launched by electrostatic separators, and completed by magnetic septa, once the two beams are in different apertures. The formulae in the text and in my *Mathematica* notebook [2] allow an easy adaptation to changes in the VLLC parameters.

A vertical separation scheme would be less demanding on the electrostatic separators, because even the fully coupled vertical RMS beam sizes are smaller than the horizontal ones. In order to avoid exciting the vertical dispersion around the whole VLLC, and hence the vertical emittance due to quantum excitation, a two-level separation as for the SSC [5] might be appropriate. In the case of horizontal separation, the compensation of the horizontal dispersion, caused by the separation, can be integrated into the dispersion suppressors at the end of the arcs, but some dispersion would remain between the separation scheme close to the interaction point and the arcs.

I only consider how to feed the two beams into separate rings at the operating energy with the apertures needed there. I do not include a scenario covering injection and acceleration to the collision energy. I do not study schemes that separate the two beams at the interaction points from injection through acceleration, and finally bring them into collision.

4.6.5 References

[1] T. Sen and J. Norem, A Very Large Lepton Collider in the VLHC Tunnel, to be published.(Preprint in Appendix 2 of this report)

[2] E. Keil, A Very Large Lepton Collider, http://wwwslap.cern.ch/~keil/Math/vllc.nb (2001).

[3] The LEP2 Team, LEP Design Report -- Vol. III: LEP2, CERN-AC/96-01(LEP2) (1996)

[4] E. Weisse, CERN, private communication (2001).

[5] SSC Central Design Group, Superconducting Super Collider -- Conceptual Design, SSC-SR-2020 (1986)

4.7 Equilibrium Degree of Radiative Spin Polarization in a Very Large Lepton Collider

Ralph W. Assmann
CERN, Geneva, Switzerland

Abstract

Electron-positron storage rings offer the unique advantage that the circulating beams can self-polarize due to spin-flip synchrotron radiation. This so-called Sokolov-Ternov effect is counter-acted by depolarizing spin resonances that reduce the achievable equilibrium degree of polarization to below its ideal value of 92.4%. Depolarizing effects grow at least with the fourth power of beam energy. Based on the theory by Derbenev and Kontratenko and the measurements at the Large Electron-Positron collider LEP at CERN, the achievable equilibrium degree of polarization is predicted for a Very Large Lepton Collider with beam energies above LEP.

4.7.1 Introduction

Well-controlled polarization of colliding particle beams can be an important ingredient to particle physics experiments. In addition, polarization provides the most accurate tool to determine the beam energy in storage rings [1]. The precise knowledge of the beam energy allows high precision measurements of particle properties, as performed in LEP for the mass and width of the Z and the W bosons [2]. All studies for future e^+e^- colliders include polarization as an important design feature. Circular e^+e^- colliders have reached 104.5 GeV maximum beam energy at the Large Electron Positron collider LEP at CERN [3, 4, 5]. Transverse spin polarization was extensively studied at LEP with measurements covering a range of beam energy from 45 GeV to 100 GeV [6]. Presently, the prospects for a Very Large Lepton Collider (VLLC) with beam energies of up to 184 GeV are being evaluated. Preliminary design considerations are given in [7]. Based on polarization theory and the experience from LEP, the possibility of transverse spin polarization at VLLC is discussed. This study is based on the VLLC parameters as given in Table 1.

Table 1: Relevant VLLC parameters [7].

Parameter		Value	Remark
Circumference		228 km	
Bending radius	ρ	25.411 km	
Revolution frequency	f_{rev}	1.315 kHz	
Maximum beam energy	E_{max}	184 GeV	
Synchrotron tune	Q_s	1/7 = 0.143	Adjusted from 0.133 as in [7]
Relative energy spread	σ_E/E	1.0 10^{-3}	Rms at 184 GeV

4.7.2 Radiative Polarization at Ultra-High Energies

Electron and positron beams in planar storage rings spontaneously polarize due to the Sokolov-Ternov effect [8]. A polarization build-up time τ_p and an ideal final polarization degree of 92.4% characterize the process. The equilibrium polarization vector points into the vertical direction and, for physics purposes, can be rotated into the longitudinal direction in the interaction point.

The polarization rate λ is the inverse of the build-up time τ_p and is often expressed in units of the revolution frequency. It is given by

$$\lambda = \frac{1}{\tau_p} = \frac{5\sqrt{3}}{8}\left(\frac{\hbar e^2}{m_e c^2}\right)\frac{\gamma^5}{\rho^3} \tag{4.32}$$

With the well known constants we see that the build-up time is proportional to the third power of the bending radius ρ and inversely proportional to the fifth power of the energy $E = \gamma mc^2$. The polarization build-up lengthens rapidly with increasing bending radius and constant beam energy. The spin tune is the precession frequency of the spin vectors and can be expressed via the beam energy E:

$$\nu = a\gamma = \frac{E}{440.6486\ \mathrm{MeV}} \tag{4.33}$$

Unavoidable imperfections in the vertical orbit cause depolarization. It turns out that synchrotron radiation drives both polarizing and depolarizing processes. The depolarization is characterized by a depolarization time τ_d and the asymptotic degree of polarization is reduced to:

$$P = \frac{92.4\%}{1 + \tau_p / \tau_d} \tag{4.34}$$

Polarization theories aim at estimating the depolarization term τ_d. Depolarization is a resonant phenomenon. Spin resonances occur at spin tunes ν_{depol} that are the sum of an integer plus multiples of the betatron tunes Q_x, Q_y and the synchrotron tune Q_s:

$$\nu_{depol} = k \pm k_x Q_x \pm k_y Q_y \pm k_s Q_s\,, \qquad k, k_x, k_y, k_s \in N \tag{4.35}$$

The machine tunes and the spin tune ν are set to values that maximize the distance of the spin tune to all significant depolarizing resonances. Typically, ν is set close to a half-integer. However, the polarization degree for such an optimized working point can still be significantly reduced due to the large width of the depolarizing resonances in electron-positron storage rings. For estimation of the expected polarization degree we follow the original theory by Derbenev, Kondratenko and Skrinsky, as described in a summary paper in 1979 [9], recently discussed in [10].

4.7.2.1 BASIC QUANTITIES

A few basic beam and machine parameters determine the behavior of polarization in very high energy e^+e^- storage rings:

The *spin tune* ν describes the energy dependence of polarization.

The *polarizing rate* λ determines the speed of polarization buildup.

The *synchrotron tune* Q_s gives the distance between synchrotron sidebands of spin resonances.

The *spin tune spread* σ_ν causes a smearing out of spin precession frequencies so that they eventually overlap Q_s sideband resonances.

We assume for a moment that the average spin tune ν_0 of a particle ensemble is on no spin resonance. Particles perform synchrotron oscillations around the average spin tune: $\nu = \nu_0 + \delta\nu$. Depending on the spin tune spread some particles might be on a spin resonance, for example $\nu = k \pm n \cdot Q_s$. During a large number of subsequent turns the particles will periodically cross the spin resonance. In order to evaluate the depolarizing effect on the ensemble polarization, it must be determined whether subsequent passings of a spin resonance are correlated or not. As shown by Derbenev, Kondratenko and Skrinsky, the criterion for correlated passings is:

$$\alpha = \frac{\nu^2 \lambda}{Q_s^3} << 1 \qquad (4.36)$$

If subsequent passings are correlated then spin rotations can average out to some extent and their effect is less severe.

4.7.2.2 CORRELATED SPIN RESONANCE PASSINGS

The following theory applies if the correlation criterion in Equation (4.36) is true. Polarization can be described with:

$$\frac{\tau_p}{\tau_d} = \frac{11}{18} \nu^2 \sum\nolimits_{k,m} \frac{|w_k|^2 < T_m{}^2(\Delta / Q_s) >}{[(k - \nu - mQ_s)^2 - Q^2{}_s]^2} \qquad (4.37)$$

Here, w_k is the complex strength of the spin resonance at integer k, ν is the spin tune averaged over the ensemble, and *m* is an integer giving the order of the synchrotron sideband resonance. The equation contains a Bessel function term T_m. Assuming a Gaussian distribution over squared amplitudes Δ of synchrotron oscillations one obtains:

$$< T_m^2 > = I_m\left(\frac{\sigma_\nu^2}{2Q_s^2}\right) \exp\left(-\frac{\sigma_\nu^2}{2Q_s^2}\right) \qquad (4.38)$$

The I_m are the modified Bessel functions. The spin tune spread is of central importance for the strength of the T_m term. The above equations are valid in the approximation of high energy. Note that betatron spin resonances with the transverse tunes Q_x and Q_y do not appear. For high energy lepton storage rings they are much weaker than synchrotron resonances and are therefore neglected.

Two regimes are distinguished in the regime of correlated spin resonance passings. If the spin tune spread is much smaller than the synchrotron tune then higher order synchrotron sidebands are not important and only the linear spin resonances ($k \pm Q_s$) affect the achievable polarization degree. This is called the "linear" theory. If the spin tune spread becomes larger than the synchrotron tune then the higher order synchrotron sidebands limit the achievable polarization degree. This is referred to as "higher-order theory".

4.7.2.3 UNCORRELATED SPIN RESONANCE PASSINGS

A different situation is encountered if subsequent passings of spin resonances are uncorrelated. They are uncorrelated if the criterion from Equation (4.36) is not true and in addition $\sigma_\nu >> Q_s$. In this case passings of synchrotron resonances are completely uncorrelated. For LEP uncorrelated passings are always completely uncorrelated. With $\sigma_\nu << 1$ the polarization can be calculated from:

$$\frac{\tau_p}{\tau_d} = \frac{11\pi^4}{54}\, \nu^2\, |w_{[\nu]}|^2 \left[1 + \frac{108\exp(-2\sigma^2{}_\nu)}{11\pi^3\sqrt{\pi}\nu^2\lambda}\right] \tag{4.39}$$

In the case of $\sigma_\nu >> 1$ Derbenev, Kondratenko and Skrinsky have obtained a quite remarkable result for the expected depolarization:

$$\frac{\tau_p}{\tau_d} = \frac{\pi |w_k|^2}{\lambda} \tag{4.40}$$

Polarization does not show any resonant dependence on beam energy in this regime, but exhibits an increase with energy, as the polarizing rate λ becomes large for highest energies. In this regime the spin tune spread σ_ν is very large and particles constantly sweep over spin resonances. As the polarization rate increases, depolarization does not increase as rapidly any more.

The theory by Derbenev, Kondratenko and Skrinsky does not include the additional energy sawtooth due to continuous energy losses along the arcs and energy gain localized in the RF sections. For LEP the sawtooth at 100 GeV was about ± 500 MeV. This is larger than the distance between integer spin resonances (440 MeV) so that the particles constantly cross the integer and linear spin resonances. The crossings in LEP were about 40 times faster than the synchrotron oscillation. Therefore, the sawtooth crossings of spin resonances for LEP might have been fully correlated, causing little depolarization. However, the consequences of the sawtooth on the spin motion are not entirely clear and require further study.

4.7.3 Studies at LEP

The polarization build-up time for LEP at 45 GeV was 5.7 hours, dropping to 6 minutes at 100 GeV. The LEP beams therefore allowed studying the behavior of polarization in a unique range of high beam energies [6]. Measurements at LEP and other lepton storage rings are summarized in Fig. 1. It is seen that the measurements at LEP cover a range from about 40 to 100 GeV that was not accessible with other storage rings before.

The LEP measurements were compared to theoretical predictions in detail. For a Q_s of 1/9 we see with Equation (4.36) that spin resonance passings were correlated ($\alpha < 1$) up to about $\nu = 166$ (73 GeV). The spin tune spread for this spin tune is still smaller than the distance between integer spin resonances (σ_ν = 0.19). We can then predict the polarization with Equations (4.37) and (4.38).

The relevant input parameters for LEP are summarized as follows:

$$\begin{aligned} \lambda = \frac{1}{\tau_p} &= 3.9\times10^{-19}\,\nu^5 \\ |w_k|^2 &= 1.94\times10^{-10}\,\nu^2 \\ \sigma_\nu &= 6.76\times10^{-6}\,\nu^2 \\ Q_s &= 1/9 \end{aligned} \tag{4.41}$$

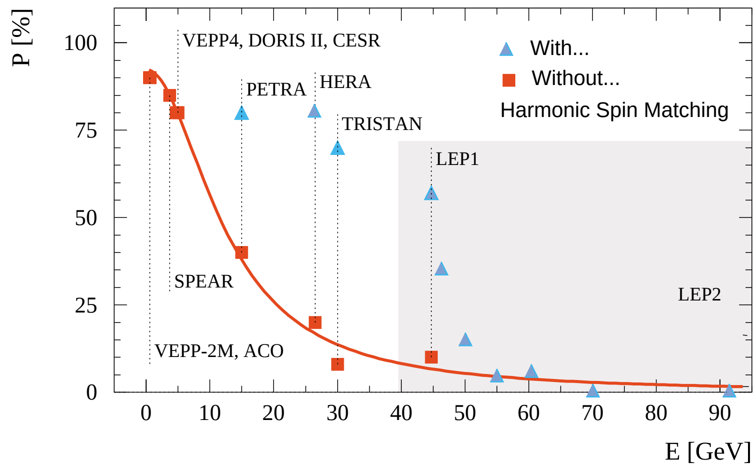

Figure 1. Overview of highest measured polarization degrees in electron-positron storage rings. Measurements with (triangle) and without (square) Harmonic Spin Matching are shown. The gray area indicates the energy range of the LEP collider. From [6].

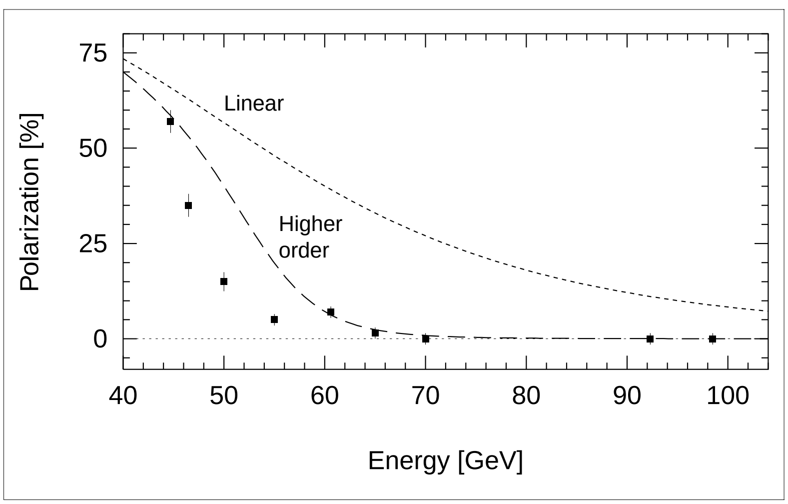

Figure 2. Maximum polarization levels measured for different energies in LEP. Note that the measurements at 44.7 GeV and 60.6 GeV were fully optimized. Measurements at other energies below 60.6 GeV were used for energy calibration purposes and are only partially optimized. The theoretically expected energy dependence of polarization is shown with $|w_k|^2 = 2\times10^{-10}\cdot\nu^2$ for both linear and higher order theory. From [6].

The resonance strength w_k is calculated from the highest observed polarization in LEP (57% at 44.7 GeV [6]) and includes the application of advanced Harmonic Spin Matching methods [6,11,12,13]. Figure 2 shows the measured data points and the calculated polarization in linear and higher order theory versus beam energy. A very good agreement is found with the complete higher-order theory. In particular, the suppression of radiative spin polarization in LEP at higher beam energies is well explained with the theory of depolarization and correlated spin resonance passings. The theory was also confirmed with dedicated machine experiments [6].

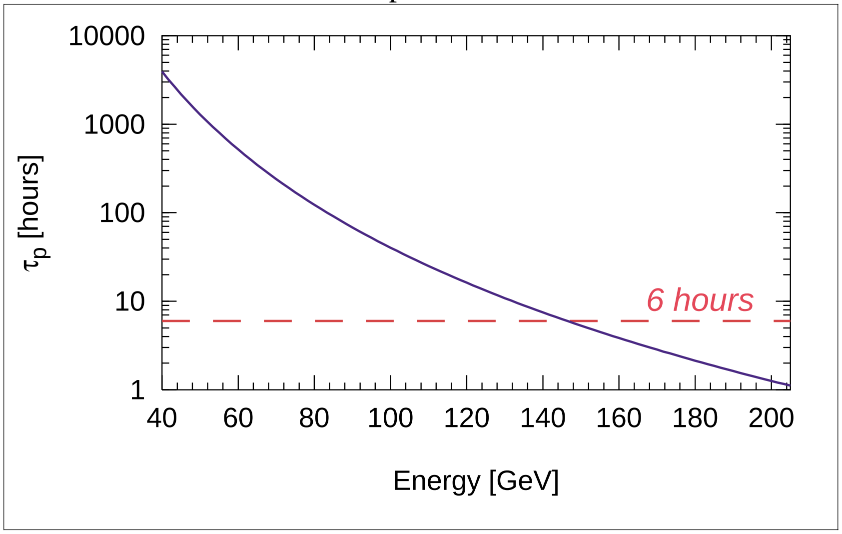

Figure 3. The polarization build-up time in the VLLC is shown versus beam energy. Practical build-up times of six hours or less are only reached at energies above 146 GeV.

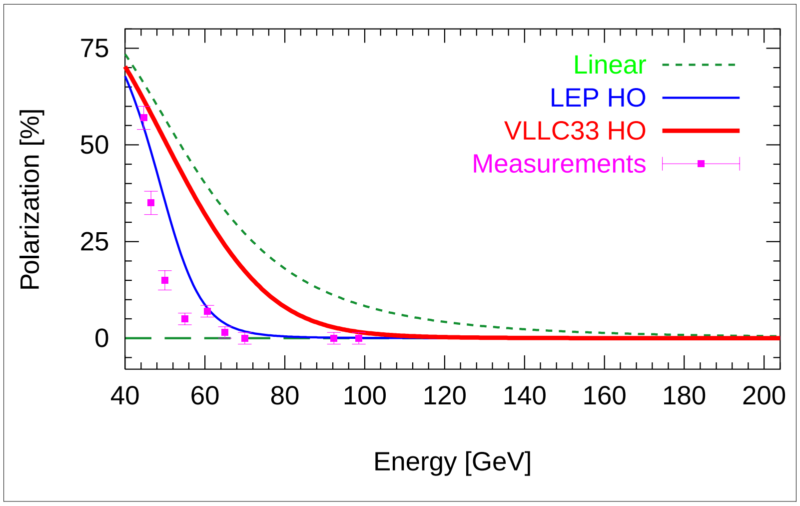

Figure 4. The linear and higher-order (VLLC33 HO) predictions for polarization at the VLLC are shown versus beam energy. Note that the linear curve is the same as for LEP, as the same resonance strength after correction is assumed. For comparison, the LEP measurements and the LEP higher-order prediction (LEP HO) are indicated as well.

4.7.4 Expectations for a Very Large Lepton Collider

In view of the excellent agreement between the experimental LEP results and the theoretical predictions by Derbenev and Kontratenko we can use their theory to predict the expected polarization at the VLLC. The relevant input parameters for estimating the equilibrium spin polarization in VLLC are:

$$\begin{aligned} \lambda = \frac{1}{\tau_p} &= 8.7\times10^{-21}\,\nu^5 \\ |w_k|^2 &= 1.94\times10^{-10}\,\nu^2 \\ \sigma_\nu &= 2.4\times10^{-6}\,\nu^2 \\ Q_s &= 1/7 \end{aligned} \tag{4.42}$$

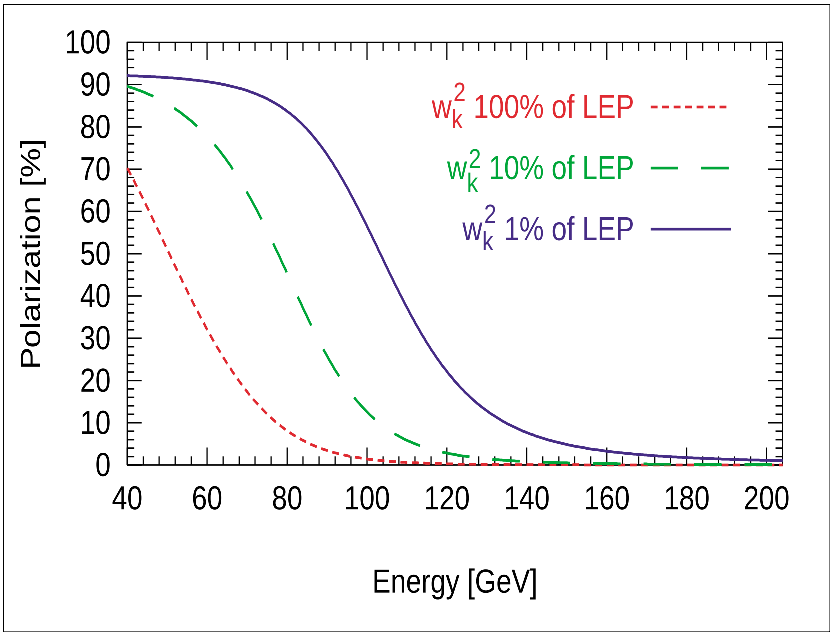

Figure 5. Higher-order predictions for polarization at the VLLC are shown for different values of the resonance strength after Harmonic Spin Matching.

Note, that the polarization build-up time is here given in units of the revolution period. With a beam energy of 184 GeV we arrive at a spin tune ν = 417.5, a polarization build-up time τ_p = 1.9 h, and a spin tune spread σ_ν = 0.42 for VLLC. The synchrotron tune is assumed to be 1/7. Choosing the value of one over an odd integer we maximize the distance of the working point (half integer spin tune) to the most important spin resonances.

The polarization build-up time is shown in Figure 3 versus beam energy. It is observed that the polarization build-up time can be prohibitively long for any practical use. Practical build-up times of six hours or less are only reached at energies above 146 GeV.

The expected equilibrium polarization in VLLC has been calculated and is shown in Figure 4 versus beam energy. The linear prediction is the same as for LEP in Figure 2, because the same residual resonance strength is assumed. This assumption means that the same absolute accuracy of Harmonic Spin Matching is achieved in VLLC (in spite of more error sources and a much longer polarization build-up time than LEP at the same beam energy). We conclude from Figure 4 that a transverse polarization of up to 5% might be feasible in VLLC up to beam energies around 90 GeV. However, the polarization build-up time at 90 GeV is about 68 hours, which would make polarization unpractical. The build-up time would reach a practical 6 hours only at around 146 GeV. At this beam energy the predicted degree of polarization is zero.

It is not excluded that the residual resonance strength in VLLC can be reduced to values below the LEP value. The calculated higher-order polarization is shown in Figure 5 for three different values of $|w_k|^2$, namely the same as in LEP, 10 times smaller and 100 times smaller. If the residual resonance strength in VLLC is reduced to about 1% of the LEP value it can be hoped to find a polarization of about 5% at 146 GeV. Since the build-up time is sufficiently short (6 hours) it could be hoped to use transverse spin polarization at this energy for precise calibration of the absolute beam energy. However, additional optimization might be needed to achieve this (compensation of harmonics from vertical dispersion in addition to vertical orbit).

A potential solution to the depolarization at high energies could come from Equation (4.40). It predicts that polarization starts rising with beam energy for very strong synchrotron radiation. The energy spread should be such that the spin tune spread becomes larger than 1. This condition is not true for the VLLC, even at highest beam energies, as it was not true for LEP. In addition, the spin dynamics in this special regime is not well understood and would require further studies before one would rely on this effect.

4.7.5 Non-Radiative Sources of Beam Polarization

It has been shown above that radiative spin polarization in VLLC has either an impractical long build-up time at lower beam energies or is strongly suppressed at higher beam energies. We do therefore consider options for obtaining polarized beams from other sources than the Sokolov-Ternov effect:

4.7.5.1 INJECTION OF POLARIZED BEAMS

It can be envisaged that polarized beams are injected into the VLLC. However, even if fully polarized beams are injected, the beams will be depolarized with the polarization degree approaching the equilibrium level that was derived above. The depolarization time can be calculated from Equation (4.34):

$$\tau_d = \left(\frac{92.4\%}{P} - 1\right)^{-1} \tau_p \qquad (4.43)$$

For an equilibrium level of polarization of 8%, the depolarization time will be ten times shorter than the build-up time. With Figure 3 we find that the depolarization time at 45 GeV would then be about 200 hours. If polarized beams would be injected at 45 GeV the polarization would be indeed preserved for a time much longer than the length of a physics fill. Polarized beams, if injected, could efficiently be used at 45 GeV.

Hypothetically considering injection at 120 GeV, we find that the depolarization time would be about 2 hours for an equilibrium polarization degree of 8%. However, with a 10 times improved Harmonic Spin Matching compared to LEP, we do only expect an equilibrium polarization level of about 3% (see Figure 5), corresponding to a depolarization time of about 40 minutes.

4.7.5.2 INJECTION OF POLARIZED BEAMS WITH SUBSEQUENT ACCELERATION TO HIGHER BEAM ENERGIES

The option to accelerate polarized lepton beams to higher energies, while preserving the polarization level, is much harder than in proton storage rings, where spin resonances have a much smaller width than in e^+e^- rings. Acceleration from 45 GeV to 115 GeV would require the crossing of 315 integer spin resonances including the very broad synchrotron satellites. The broadness of the spin resonances has the immediate consequence that the spin resonance crossing is slow, making resonance crossings with spin flip, as described by Froissart-Stora, impossible. A system of Siberian snakes able to preserve the polarization level in this situation remains to be proposed. Further studies are required.

4.7.5.3 POLARIZATION THROUGH INTERACTION WITH POLARIZED LASER LIGHT

Ideas exist to generate beam polarization by interaction of the particle beams with polarized laser light. In order to be effective, this process must be stronger than the depolarizing process due to synchrotron radiation. At 184 GeV the depolarization time would be as short as about 30 seconds for 0.5% equilibrium polarization level. In addition, the proposed schemes to generate polarized particle beams with laser light are often destructive to the particle beam, with most particles lost. However, it cannot be excluded that a proper mechanism can be invented and further studies are required.

4.7.6 Conclusions

Lepton storage rings provide self-polarizing beams due to the Sokolov-Ternov effect. However, the synchrotron radiation drives both polarizing and depolarizing processes. The ratio of polarizing time to depolarizing time grows with at least the fourth power of energy. Depolarizing processes therefore become very strong at higher beam energies and overtake the strength of polarizing processes. As a result radiative spin polarization is being suppressed for very high energy e^+e^- storage rings. A long-standing theory of depolarization at high energies was experimentally confirmed at the Large Electron Positron collider LEP at CERN. This theory explained the observed suppression of radiative polarization at higher LEP energies in detail.

Based on the confirmation with LEP data we can use the theory by Derbenev and Kontratenko to predict the achievable equilibrium degree of polarization at a Very Large Lepton Collider VLLC. For a 228 km ring we find that the polarization build-up times are prohibitively long at lower beam energies. Only above 146 GeV the build-up time becomes a practical 6 hours. However, at those high beam energies polarization is strongly suppressed. In a very optimistic case a polarization level of about 5% can be achieved at 146 GeV, if the residual spin resonance strength in VLLC is reduced to about 1% of the LEP value. Polarization would be lower at higher beam energies.

The injection of polarized beams at 45 GeV seems feasible and the injected level of polarization could be maintained over sufficiently long times, even if the equilibrium degree of polarization is small. The acceleration of injected polarized beams to higher beam energies is much harder than in proton storage rings and no working scheme has been designed and studied yet. The generation of polarized beams through interaction of the beams with polarized laser light must be faster than the depolarization time and must preserve the important beam properties. There is no design for such a solution yet.

4.7.7 References

[1] L. Arnaudon et al, “Accurate Determination of the LEP Beam Energy by Resonant Spin Depolarization”, Z. Phys. C66(1995)45.

[2] R. Assmann et al, “Calibration of Center-of-Mass Energies at LEP1 for Precise Measurements of Z Properties”, CERN-SL/98-12.

[3] S. Myers. CERN Yellow Report 91-08.

[4] D. Brandt et al., “Accelerator Physics at LEP”, Reports on Progress in Physics, **6**3, 939 (2000).

[5] R. Assmann, “LEP Operation and Performance with Electron-Positron Collisions at 209 GeV”. Proc. of the 11th Chamonix Workshop. January 15-19, 2001, Chamonix, France. CERN-SL-2001-003 DI.

[6] R. Assmann et al, “Spin Dynamics in LEP with 40-100 GeV Beams”. Proc. Int. Spin Symposium SPIN2000. September 16-20, 2000, Osaka, Japan.

[7] T. Sen and J. Norem, “A Very Large Lepton Collider in the VLHC Tunnel”. To be published. (Preprint in Appendix 2 of this report)

[8] A.A. Sokolov and I.M. Ternov, “On Polarization and Spin Effects in the Theory of Synchrotron Radiation”, *Sov. Phys. Dokl.* 8(1964)1203.

[9] Ya.S. Derbenev, A.M. Kondratenko and A.N. Skrinsky, “Radiative Polarization at Ultra-High Energies”. *Part. Acc.* 1979, Vol. 9, pp. 247-266.

[10] R. Assmann. “The regimes of polarization in a high energy e+e- storage ring”. PAC99.

[11] V.N. Baier and Yu.F. Orlov, “Quantum Depolarization of Electrons in a Magnetic Field”. *Sov. Phys. Dokl.* 10(1966)1145.

[12] R. Rossmanith and R. Schmidt, “Compensation of Depolarizing Effects in Electron Positron Storage Rings”. *Nucl. Instr. Meth.* A236(1985)231.

[13] D.P. Barber et al, “High Spin Polarization at the HERA Storage Ring”. *Nucl. Instr.Meth.* A338(1994)166-184.

5 ACCELERATOR SYSTEMS

5.1 Magnets and vacuum chamber

Jim Norem, Lee Teng , Sushil Sharma
Argonne National Lab, Argonne, IL 6043
Oswald Grobner
CERN, Geneva, Switzerland

5.1.1 Introduction

The design of the magnet arcs is primarily determined by a number of constraints set by the operational requirements of the machine.

- The vacuum chamber aperture must be sufficient for beam stability.
- A number of vacuum requirements must be met. The synchrotron radiation power must be absorbed and chamber must be cooled, but the shape as seen by the beam must be continuous. The first beam must circulate for one hour. Thermal expansion must be allowed but the number of bellows must be minimized. Desorbed gas must be pumped.
- The use of one ring or two is determined by the allowable amplitude of emittance growth due to parasitic collisions.
- Magnetic shielding requirements are set by the magnitude of the assumed field external to the magnet yoke B_{ext} = 0.00005 T for the earth's field and ~0.0700 T if the proton ring is operational.
- The magnet design is determined by the injection energy, the maximum required bending field, the steel used, and its magnetic properties.
- Assembly and maintenance must be simplified and done robotically.
- Costs must be minimized.

These requirements will then generate a design which can be used to estimate the pumping, cooling, magnet power, magnet size and ultimately the cost and complexity of the arcs.

We have assumed that the overall ring would be a racetrack (or square with rounded corners), whose shape must be compatible with the requirements for the VLHC. The ring would have two longer straight sections, one of these would be primarily occupied by the experimental interaction point, and the other could be used for rf systems injection, scraping, dumping etc. The rf is located in the two (perhaps 4) dispersion free regions of the straight sections. The straight sections would also contain optics for beta matching and emittance suppression. Since the bunch spacing can be decreased to the length of the rf straight sections, there is some incentive to minimize this.

Maximizing the luminosity at the lower range of energies is important enough to want many bunches in the ring, and minimizing the parasitic collisions of these bunches can be done most easily with two rings through the arcs, one for e^+ and one for e^-. This requirement doubles the cost of the magnets, power supplies and vacuum systems, and requires the addition of electrostatic and magnetic separators to separate and combine the beams at the ends of the straight sections. The beam separator systems have been described by Keil and consist of roughly 10 m of electrostatic separators with 2.5 MV/m followed by magnetic septa with a field of 0.25 T and a length of 10 m.

The use of the machine as an ep collider has been considered, and the cost of the magnetic shield to isolate the low field electron ring from the strong fringe fields generated by the proton ring has been considered.

5.1.2 Vacuum System Design

The design of the vacuum system relies heavily on the experience and successful operation of the LEP vacuum system over the 14 years this machine was used. The general principles of the design of this system are described in Chapter 10 of the LEP design report Vol III. The primary design issues are: 1) the size of the vacuum chamber, which also determines the size and cost of the magnet and magnet power supplies, 2) achieving a useful vacuum without the use of bake-out and the bellows this process requires, 3) absorbing the synchrotron radiation power produced by the beam.

The internal dimensions of the vacuum chamber have been determined from the requirements for maximizing the threshold for transverse mode coupling instability. The half height determined by this requirement, for this study, is 4.8 cm, with an aspect ratio of 2.5, giving a horizontal half width of 11.5 cm. Since the beam sizes in the arcs are only σ_x = 1.52 mm and σ_y = 0.63 mm at the maximum energy, the vacuum chamber becomes much larger than the 1.5 – 2.5 cm required by the usual rules of 10σ + 1 cm for steering errors. In addition we assume an antechamber will be required to separate the synchrotron radiation from the beam.

The initial requirement for useful operation is that the partial pressures in the machine be low enough so the beam can circulate for a time that is useful both for evaluating the beam optics and to begin scrubbing the walls of the vacuum chamber using synchrotron radiation from the beam. We arbitrarily define 1 hour as a useful time to begin these two operations. Since the beam lifetime is

$$\tau(h) = 3 \cdot 10^8 / P_{N_2}(\text{Torr}),$$

the equivalent nitrogen pressure vacuum chamber must be below $3 \cdot 10^{-8}$ Torr. The usual way of insuring that this pressure could be reached would be to allow for an in-situ bake of large sections of the vacuum chamber, however the thermal expansion that must be absorbed in 100 m of aluminum chamber, with a 100 ^{O}C bake, would be 24 cm. We have tried to eliminate this process and the large bellows required for it. The requirements for minimizing the loss factors due to bellows have encouraged us to look at the option of pre-baking sections of the vacuum chamber, filling these with nitrogen, welding them in-situ, and using them without an in-situ bake.

Pumping will be done primarily using Ion Pumps located near the lumped absorbers. These will pump the vacuum chamber slowly through the conductance offered by the vacuum chamber and the antechamber. Turbo pumps will be used for rough pumping, and NEG pumps may be used in the antechamber if needed. Note that the size of this project effectively insures that significant lengths of the vacuum chamber will be installed and operational before the final sections are pumped down. The constraint that the vacuum must be below $3 \cdot 10^{-8}$ Torr for a one hour beam lifetime applies to the average vacuum around the ring. The sections which have been pumped for years would be at lower pressures, and would loosen the vacuum requirements on the components that had been recently installed.

The spectrum of synchrotron radiation produced by the beams changes dramatically over the design energy range of the collider ring. At 45 GeV, the critical energy of the protons is 6.5 keV, but at 185 GeV, the critical energy of the photons is 145 keV. At low energies the photons are almost entirely absorbed by the aluminum chamber, but at the highest beam energies, the photons easily penetrate through the aluminum chamber and scatter freely around in the accelerator tunnels. The transmission of the vacuum chamber to these photons is shown in Figure 1.

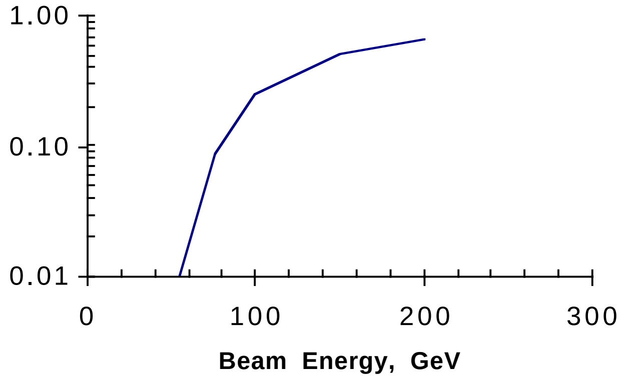

Figure 1. The transmission of a 1 cm aluminum window for the synchrotron radiation spectrum.

It is useful to note that 500 keV photons are not absorbed by atomic processes, and will diffuse through all materials, causing a variety of complications to the control electronics, electrical insulators and vacuum equipment. These high energy photons will be a diffuse source of gas over a large volume downstream of the lumped absorbers. The pumping requirements are set by the molecular desorption yield as a function of the x ray or electron beam energy. At LEP these yields were seen to increase rapidly at high energies, presumably due to the multiple traversals of the metallic surface by the synchrotron photons and its Compton secondaries.

The overall design of the vacuum chamber is shown in Figure 2. The chamber is extruded aluminum, with a channel for the beam, an antechamber for pumping, cooling channels and a mounting bracket. At intervals of about 50 m, an x-ray window, absorber and pumping chamber assembly are attached to this extrusion. This must be done at intervals in the bending magnets and before any of the quadrupoles. The primary high energy synchrotron absorber would be made of copper and located in air so that x-ray induced outgassing would not affect the machine vacuum. In addition to absorbing the synchrotron power, it is highly desirable to have these absorbers absorb as large a fraction of the x-rays as possible to eliminate these from scattering back into the chamber and re-producing desorbed gasses from the vacuum chamber surface. Some high Z shielding around the absorbers would be useful for accomplishing this.

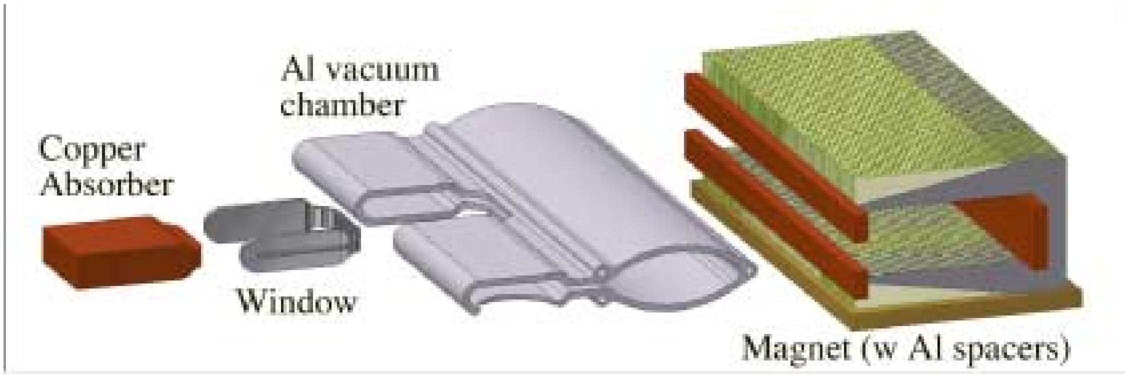

Figure 2. The vacuum chamber and synchrotron radiation absorbers.

Cooling of the vacuum chamber is done with water cooling channels along the length of the extrusion and in the window insert. The copper x ray absorber is separately cooled. Although the major source of thermal expansion has been eliminated, it is still necessary to allow for some thermal expansion with well designed minimum-range bellows. These bellows must be distributed around the circumference. It is also necessary that some motion must be allowed between the magnet and vacuum chamber.

5.1.3 Design of the Arc Magnets

The magnet design, is to a large extent, determined by the shape of the vacuum chamber, and is shown in Figure 3. The magnet/vacuum chamber assembly requires an external support structure for mechanical stability and also for magnetic shielding. We assume that the structure would be a fairly light space frame, which could be made from iron and capable of helping to conduct the earth's field around the magnets. If the electron ring were used with a high energy proton ring for *ep* collisions, the fields would be very much larger and the volume of iron required would be significant. Reducing the field inside the cylindrical box by a factor of 500 – 1000 (i.e., from 700 G to ~1 G) would require a shield thickness on the order of on tenth of the shield radius, and a mass many times that of the magnet / vacuum chamber assembly. Thus we assume that the proposed ring would be used only for electron collisions. The magnet and vacuum chamber would be mounted independently on the support structure to allow for precision locating of the magnet ring and some relative motion of the vacuum chamber, which will be subject to thermal motion at some level. The support structure will be attached to the side or top of the tunnel at intervals.

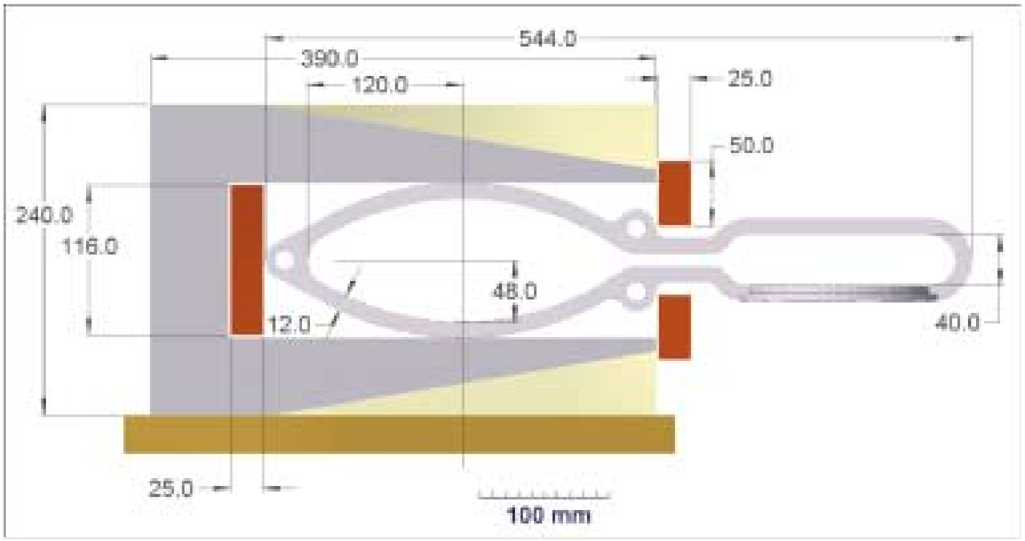

Figure 3. The magnet, vacuum chamber and support / shield structure.

The dipole gap distance of 11 cm requires 2100 A to reach full field. This excitation current is carried by conductors on the inside and outside of the iron lamination. These conductors and the laminations are supported by spacers made of die cast aluminum. The total power requirement for the dipoles is then found to be roughly 11 MW, or 48 W/m. While it might be possible to remove this amount of power using air cooling, the conductors would heat up by about 15 ^{o}F and thermal expansion of the conductors could tend to induce stresses on the magnet. We assume that water cooling channels could be extruded into the conductors which could easily remove this power.

The bending magnets required for the arcs will operate at low fields, from 0.0057 T at injection, to 0.0238 T, at full field. These low fields cause make the optics particularly susceptible to external error fields, either due to the earth's 0.00005 T field or the fringe fields from the low field VLHC magnets. Ideally the error fields in accelerator magnets should be on the order of 10^{-3} – 10^{-4} times the dipole field. The external fields will be naturally attenuated by two mechanisms: 1) the structure required to support comparatively fragile magnet and vacuum chamber assembly can be made from iron, which will shield the magnets inside from external fields, and 2) the yokes of the magnets are a low reluctance path to guide external magnetic fields around rather than through the vacuum chamber. Data taken with a model magnet have shown that the external fields drop off like $e^{-7x/g}$, where g is the gap height and x is the distance into the magnet. These data are consistent with calculations by Enge and others on magnet edge effects.

In addition to the external fields, the iron yokes will be a source of magnet field errors. The remnant fields produced in iron after the excitation fields have been removed, the source of hysteresis losses, can cause error fields in the magnet. There are a wide variety of magnetic materials which have varying hysteresis losses, permeability curves and costs. Perhaps the most useful material for our purposes is iron with very low carbon content. As the carbon is removed, the hysteresis losses decrease in a nonlinear way, but drop by approximately an order of magnitude from commercial 1010 steel, with 0.10% carbon, as shown in Figure 4. The low carbon steel is produced by vacuum annealing, a process which is fairly commonly available and seems to add only about 10% to the cost of the steel. While the steel becomes somewhat softer, it can be fairly easily worked and stamped. A local source for this material is ISPAT/Inland steel, in Gary Indiana. Figure 4 shows the hysteresis loss, proportional to the remnant field, for this steel.

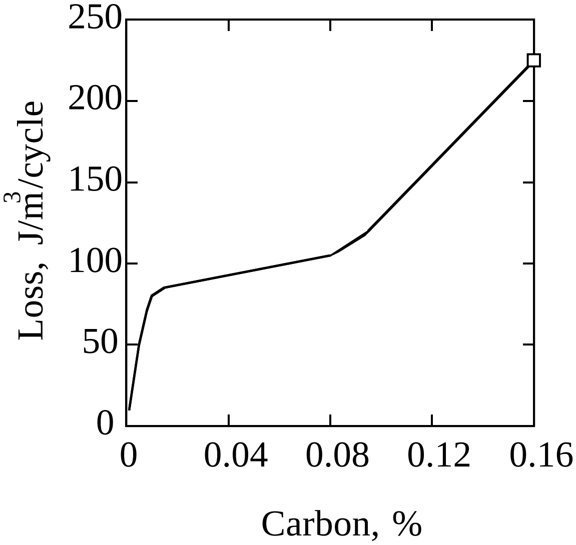

Figure 4. Hysteresis losses as a function of carbon content in steel. Standard "low carbon" 1010 steel has 0.10% carbon content.

The comparatively large aperture of the vacuum chamber affects the design of the quadrupole magnets primarily in two ways: the field quality close to the axis is almost independent of the placement of the iron and conductor, and the required excitation current is proportional to the pole radius squared, so the power requirements of the quadrupoles increases.

The actual design of the quads is not highly constrained. In order to reduce the current requirements it seems desirable to make the magnets on the order of a few meters long. It seems desirable to design the quadrupoles with many turns/pole and connect them in series off of separate supplies from the dipoles since this will permit more flexible tuning of the machine, The current could be carried around the arcs in somewhat oversized busses with minimal power losses. Local tuning could be done with additional current would be provided from trimming supplies or short independent tuning quadrupoles.

At 185 GeV, the quadrupole gradient*length should be 7.7 T, and this number, the conductor area and the number of quads determine the total power consumed by the arc quads. The conductor area is constrained somewhat by separation of the two rings, but the quadrupole power dissipation is much smaller than the dipoles.

The maximum gradient of the quadrupoles is constrained by radiative synchro-betatron coupling, which causes electrons at large betatron amplitudes to radiate too much energy to stay in the bucket. The maximum gradient is approximately set by the requirement that the *B* field seen at 1σ ($= 0.0015$m) is less than the *B* field in the arcs (0.0238 T), or $B' = 0.0238 / 0.0015 = 15$ T/m. The constraint is not severe, since the required gradient is inversely proportional to the length, and the lattice can accommodate very long quadrupoles.

5.1.4 Design of the RF Systems (Civil engineering)

At the highest energies, the total energy loss per turn is 4 GeV out of 185 GeV, or 2.2%. This large energy loss results in a distorted orbit, (energy sawtooth), through the arc magnets unless the rf structures, and the power they provide, is distributed around the ring. Thus we will require a number of zero dispersion straight sections at intervals around the ring.

5.1.5 Design of the Cooling Systems

The cooling requirements of the facility are determined by the synchrotron loss, the dipole design and the rf efficiency. While the synchrotron losses are more or less constant through the arcs, the magnet power supplies can be almost anywhere and the rf cooling can be located wherever these are placed. Although lumped absorbers will be used, the actual temperatures reached in these absorbers will be fairly low. Likewise the temperature range allowed in the magnets and vacuum chambers will also be low since thermal expansion is undesirable. Thus the final temperature of the cooling water will probably be only a few degrees above the input temperature. This small range of temperatures implies that the cooling water will not be hot enough to permit energy recovery or other useful benefits to be obtained from the elevated temperature. Cooling towers seem to be required at intervals around the ring.

5.1.6 Power requirements

The majority of the power goes to replace the synchrotron radiation losses. Other systems, however, also use a considerable amount of power. We list the major contributions in Table 1. When the klystron input power, the rf losses and the cooling requirements for the rf cavities are considered, the effective efficiency drops to about 0.5. The majority of the power goes to replace the presumably constant 100 MW of synchrotron power, but the cryogenic load depends on the total voltage of the rf system and the magnet currents depend on the beam momentum, thus the total power requirements decrease somewhat at lower energies. It is difficult to reduce the power requirements without significantly reducing the performance of the machine. This power must be supplied at widely separate locations, and the cost of transmission to these locations has not been considered.

Table 1. Power Requirements (MW)

RF System	100 MW/ε_{rf} = 157
Bending magnets	11
Quadrupoles	??
Cryogenic system	42
Total	210

5.1.7 Cost Optimization

In order to optimize the magnet and vacuum chamber design, we started a very primitive cost minimization for the materials and power costs. Since the cost of the conductor is proportional to the cross sectional area, and the dissipated power and thus the operating cost are proportional to the inverse of the area, the approximate minimum will be at the point where the two are roughly equal. We used the bulk cost for iron, aluminum and copper and the marginal cost for high volume Con Ed consumers, to estimate the power cost for operating the ring of dipoles for 10 years. This exercise determined that aluminum conductors with a 50 cm^2 cross section were a realistic first iteration for the dipole magnets, and aluminum seems to be the lowest cost material.

The same exercise was used to estimate the cost of raw materials in the magnet and vacuum system. The iron laminations are only a small fraction of the volume and mass of the magnet system and since the cost of iron is small compared to other metals, the magnet structure cost is primarily determined by the structure required to keep the laminations in place.

Since no design exists, it is not possible to estimate the cost of the facility with any precision. Nevertheless it is possible to look at the raw materials (used in optimizations) and estimate an order of magnitude for the final total cost. We believe that for such a large, simple magnet, robotic assembly is possible and the construction cost can approach the raw materials costs, and these arguments are the basis of an approximate cost estimate.

5.2 VLLC RF system

Sergey Belomestnykh
Laboratory of Nuclear Studies, Cornell University, Ithaca, NY 14850

5.2.1 Introduction

The total voltage of 4.66 GV required to support VLLC beams is 33% higher than that of LEP-II (3.5 GV) [1, 2]. The only way to keep the size of accelerating structure reasonable is to use superconducting RF technology as it was done at LEP. Although sheet metal niobium cavities are capable to deliver very good performance [3], we propose to use niobium sputtered on copper technology developed at CERN. There are several advantages of using this technology: i) higher thermal conductivity of copper provides better stability against quenching as compared with sheet Nb; ii) higher Q factor than that of bulk Nb; iii) insensitivity to small magnetic fields, and finally iv) saving on the cost of raw material.

5.2.2 Choice of frequency and gradient; cost optimization

For a large scale accelerator complex capital cost optimization determines the accelerating gradient [4]. RF frequency choice is dictated by desirable operating temperature and availability of high average power klystrons. 4.5 K operation is preferable due to simpler cryostat design, cheaper and more reliable and simpler refrigerator components. This leads us to the frequency range of 300 – 500 MHz. RF losses per unit length increase with square of the gradient:

$$P_m = \frac{E_{acc}^2}{\left(R/Q\right)_m \cdot Q_0},$$

Here P_m is the RF power per unit length, E_{acc} is the accelerating gradient, $(R/Q)_m$ is the characteristic impedance per unit length, and Q_0 is the quality factor of the cavity. The total active length of the structure is $L = V_{RF}/E_{acc}$, where V_{RF} is the total RF voltage.

The refrigerator power needed is the sum of the static losses, the fundamental RF losses, HOM induced losses and distribution system losses. To first order the fundamental RF losses is the dominant part. Then the refrigerator power and thus the investment cost is proportional to the accelerating gradient (if Q_0 is independent of gradient):

$$C_{refr} = k_{refr} \cdot \left(P_m \cdot L\right) \propto E_{acc}$$

For this optimization we used the cost factor k_{refr} of 1.7 k$/W for refrigerator operating at 4.5 K and 3.4 k$/W for 2.5 K. Also, we took into account quality factor dependence on accelerating gradient as measured for LHC [5] (400 MHz) and LEP [2] (352 MHz) cavities (Figure 1).

The cryomodule cost scales approximately linearly with total length of the RF structure and thus inversely with the accelerating gradient [6]:

$$C = k_{cryo}(0.8)^{\log(L)}\sqrt{\frac{1300}{f[MHz]}}\cdot L \propto \frac{1}{E_{acc}},$$

Here we used the cost factor k_{cryo} of 200 k$/m for 4.5 K and 250 k$/m for 2.5 K.

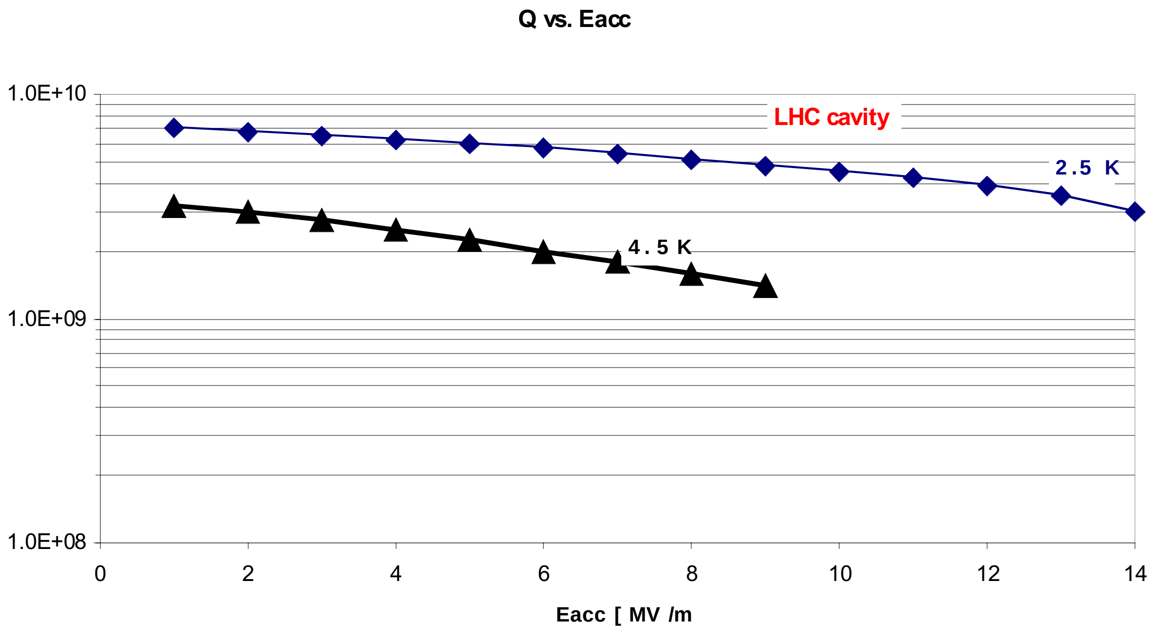

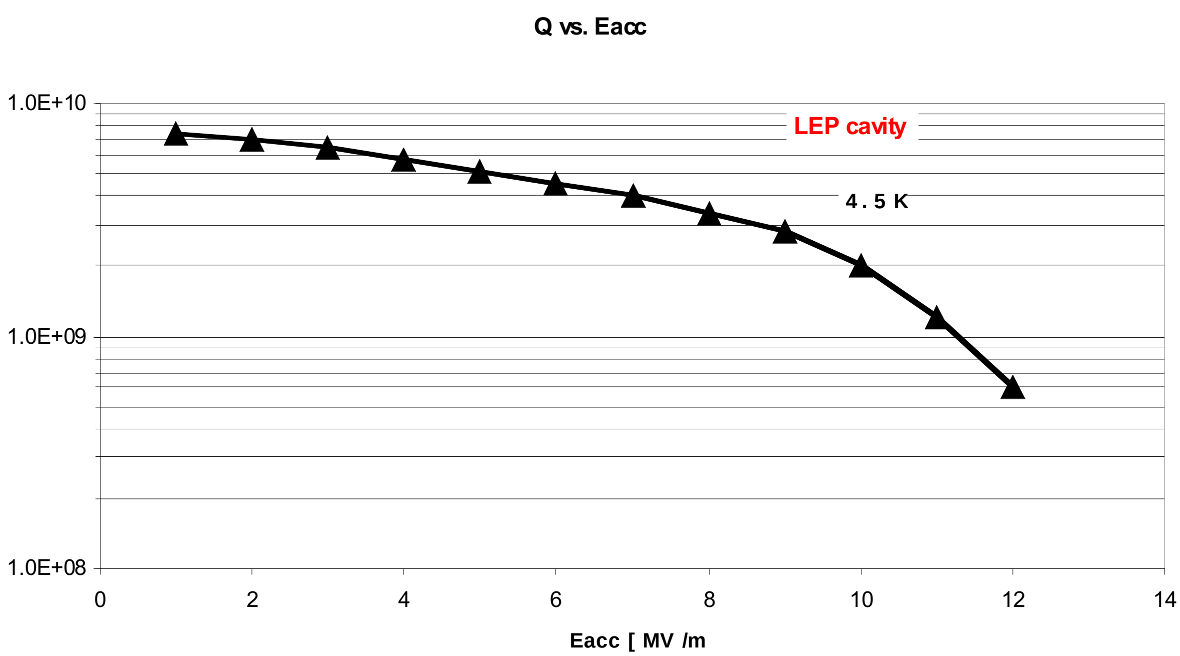

Figure 1: Q factor dependence on accelerating gradient for LHC [5] and LEP [2] cavities.

The total cost then is dominated by the RF structure cost at low gradients and by cryogenic cost at high gradients. We chose 400 MHz and 4.5 K as a baseline for optimization. There is a rather broad minimum in the range from 4 to 8 MV/m (Figure 2). It is worthwhile to see if one can gain by operating at lower (2.5 K) temperature or by choosing lower (352 MHz) frequency. Plots in the Figure 3 show that lower temperature operation can allow us to use higher gradients and hence fewer number of cryomodules. The total cost at the minimum does not change too much though.

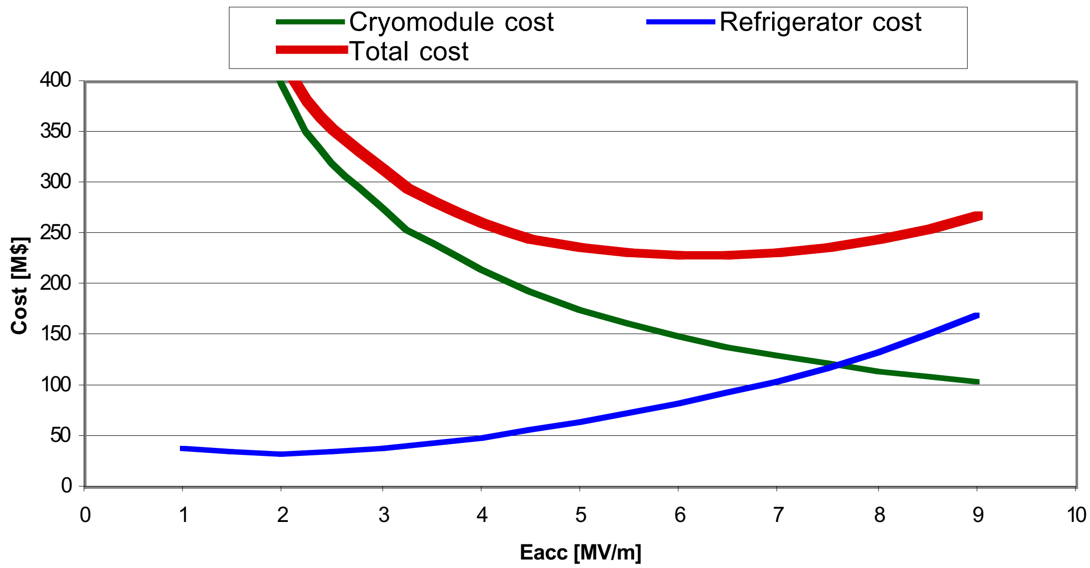

Figure 2: Cost optimization for 400 MHz LHC-type cavities.

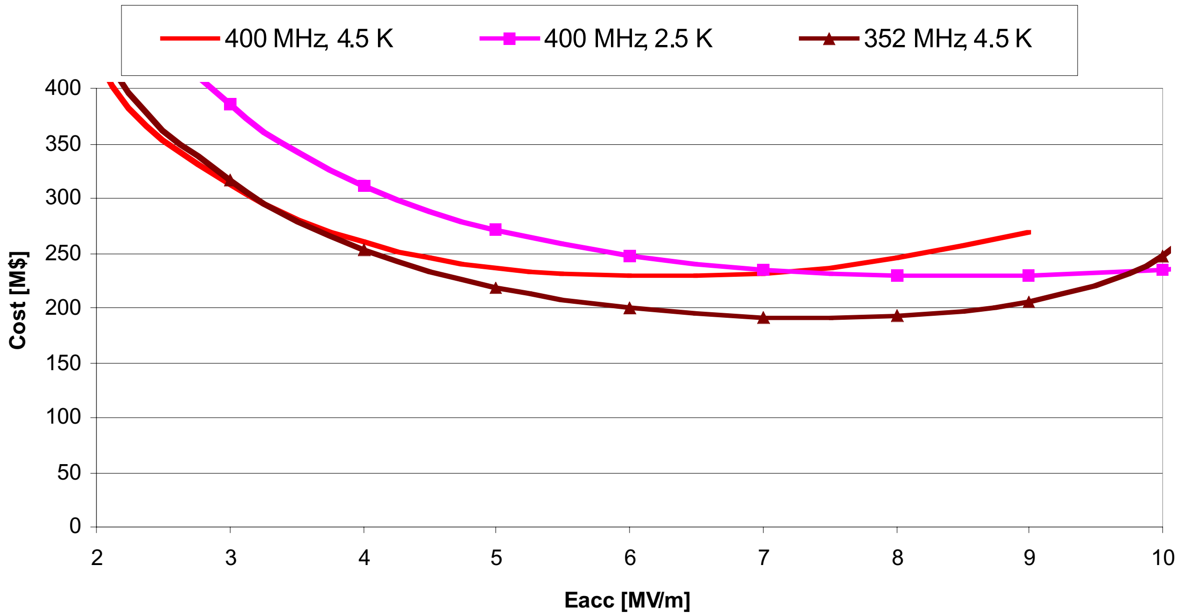

Figure 3: Comparison with lower temperature operation and with 352 MHz LEP-type cavities.

On the other hand, choosing lower RF frequency can significantly decrease total capital cost of the system. Therefore for further considerations we decided to set RF frequency to 352 MHz and gradient to 8 MV/m. The latter value should be relatively easy reachable: LEP-II cavities were routinely operating in 2000 with average gradient of 7.5 MV/m. This immediately determines following parameters:

number of cells *N*cell = 1376
number of cells per cavity *N*cell/cav = 4
number of cavities per cryomodule *N*cav/cryomodule = 4 (similar to LEP)
required cryoplant capacity *P*cryo = 42.3 kW (without distribution losses and safety margin)
power delivered to beam by each cell *P*beam/cell = 73.1 kW
loaded quality factor of fundamental mode $Q_L = 1.37\times10^6$
number of 1.3 MW klystrons *N*kly = 86

In summary, RF structure cost estimate is 121 M$, cryogenic cost is 72 M$, and klystrons and other RF hardware cost will be approximately 120 M$. Then the total capital cost of RF system is 313 M$.

5.2.3 Beam-cavity interaction

Let us now evaluate effects related to the beam-cavity interaction. We will assume LEP cavity shape that has the equator radius of R_{eq} = 376 mm and the iris radius of R_{iris} = 121 mm. Each cryomodule is furnished with two l = 330 mm long taper transitions to a beam pipe of r = 20 mm. Loss factor of the cryomodule can be calculated using formulae [7, 8]:

$$k_{cell} = \frac{1}{2\pi^2\varepsilon_0 R_{iris}}\left(\sqrt{\frac{g}{\sigma}}-1\right),$$

$$k_{fund} = \frac{\omega_{fund}\left(R/Q\right)_{fund}}{4}\exp\left(-\frac{\omega^2\sigma^2}{c^2}\right),$$

$$k_{tapers} = \frac{1}{4\pi\sqrt{\pi}\varepsilon_0\sigma}\left(1-\tilde{\eta}_1\right)\ln\frac{R_{iris}}{r},$$

$$\tilde{\eta}_1 = \min\left(1.0, \eta_1\right),$$

$$\eta_1 = \frac{l\sigma}{\left(R_{iris}-r\right)^2},$$

$$k_{parasitic} = k_{cell} - k_{fund},$$

$$k_{cryom} = 16k_{parasitic} + k_{tapers},$$

where g is the cavity gap length, and σ is the bunch length. Then for 7.5 mm bunch length we calculate the RF cell loss factor k_{cell} = 0.263 V/pC, the fundamental mode loss factor k_{fund} = 0.064 V/pC, the parasitic HOM loss factor $k_{\mathrm{parasitic}}$ = 0.199 V/pC, the tapers loss factor k_{tapers} = 0.921 V/pC, and the total loss factor of the cryomodule k_{cryom} = 4.11 V/pC. The higher order mode (HOM) power is

$$P_{HOM} = k_{cryom}\frac{I_{beam}^2}{N_{bunch}\cdot f_{rev}} = 11\ \text{kW/cryomodule},$$

where I_{beam} is the total beam current, N_{bunch} is the number of bunches, and f_{rev} is the revolution frequency. The total HOM power is 4.27 MW. How much of this power will go to cryogenics? LEP reported cryogenic loss dependence on bunch length, but LEP cryomodules had unshielded bellows and lossy HOM cables. It is possible to minimize amount of the HOM power going to cryogenics with careful design of HOM dampers. It will probably be a combination of broadband beam line loads (CESR[9]/KEKB[10] type or LEP/LHC[11] type) to handle high power of propagating HOM and coaxial narrowband probes (LEP/LHC type) near cavities to load trapped higher order modes.

The beam loading effects on the RF system controls are very mild due to relatively small beam current. The RF phase modulation by the bunched beam is

$$\Delta\varphi = \frac{I_b\cdot R/Q\cdot h\cdot\sin\varphi_s}{\pi\cdot V_{RF}} = 0.22^\circ,$$

where I_b is the bunch current, h is the RF harmonic number, ϕ_s is the synchronous phase, and V_{RF} is the RF voltage per cell. Cavity detuning to compensate reactive beam loading is

$$\Delta f_r = -\frac{1}{2} f_{RF} \frac{I_{beam} R/Q \cos\varphi_s}{V_{RF}} = 77.6 \text{ Hz} ,$$

less than cavity bandwidth of 257 Hz (here f_{RF} is the RF frequency). Even such small detuning of fundamental mode frequency can cause excitation of the coupled-bunch mode of number –1 because of very low revolution frequency of 1.315 kHz. The growth rate due to fundamental mode impedance is 11.8 msec, shorter than longitudinal damping time of 35 msec. Special feedback loop may be required to deal with this instability [12].

Higher order modes can also cause excitation of multi-bunch instabilities. We can estimate requirements to loaded Q factors for the worst case, when high impedance mode (R/Q = 20 Ohm) is tuned to the synchrotron sideband:

$$Q_L = \frac{4h \cdot V_{RF} \cos\varphi_s}{\Omega_s \tau_s I_{beam} R/Q} = 1.6 \times 10^5,$$

here Ω_s is the synchrotron frequency, τ_s is the longitudinal damping time, and m is the closest harmonic number to the HOM resonant frequency. This damping is easy to reach. LEP cavities have loaded HOM quality factors of the order of 10^4, which is more than adequate.

Special attention must be paid during cavity design period to its mechanical properties: LEP 4-cell structure has mechanical resonance at approximately 100 Hz. This is very close to synchrotron frequency of 175 Hz and can have very unpleasant effect on beam dynamics. The structure must be stiffened to raise its mechanical resonance frequencies. Also, ponderomotive effects should be studied (LEP RF system suffered from those).

5.2.4 General considerations and overall RF system parameters

As in case of LEP, reliability of the RF system will be very important issue. Trip rate at LEP was 1 per 14 minutes. In order to avoid frequent beam losses, system must have enough RF voltage margin so that temporary loss of one or two RF stations does not cause a beam dump. LEP had 7% reserve voltage.

VLLC RF system would greatly benefit from R&D on improving technology of sputtering niobium on copper with the goal to decrease if not completely eliminate phenomenon of the Q slope. Special efforts should be devoted to understanding the nature of this effect. Success of this R&D would allow increase of accelerating gradient without taking serious punishment in the cryogenic heat load. For example, if it would be possible to reduce Q slope by a factor of 2 then one could increase gradient to 10 MV/m reducing active RF structure length to 466 m and RF structure cost to 99 M$ and keeping cryogenic requirements about the same. This would produce saving of about 22 M$. If RF system impedance is an issue then one could make another step by increasing gradient to 12 MV/m. This reduces active length to 388 m and impedance by a factor of 1.5, but would require more installed refrigerating capacity.

The RF system parameters and some RF relevant machine parameters are summarized in Table 1. Overall, the VLLC RF system would be very similar to the LEP-II RF system with some improvements required in cavity design. The system should be divided into several sections distributed around the ring with klystron galleries at the tunnel level parallel to the cavity chains, and cryogenic plants at the ground level.

Table 1: Summary of RF System Parameters.

I_{beam} total	[mA]	25.04
ΔU	[MeV/turn]	3990
P_{beam}	[MW]	100
f_{RF}	[MHz]	352
V_{RF} total	[MV]	4660
E_{acc}	[MV/m]	8
*N*cell/cavity		4
Cavity length	[m]	1.702
*N*cav		344
*N*cav/cryomodule		4
Modular length	[m]	12.5
L active	[m]	585.5
*N*kly		86
SC material		Nb/Cu
R/Q per cell	[Ohm]	116
*Q*o		3.4×10^9 (8 MV/m)
*Q*ext		1.37×10^6
Input coupler		Coaxial
P_{RF} at window	[kW]	292
Static heat leak per cryomodule	[W]	84
*P*refr @ 4.5 K	[kW]	50
k (σ, mm)	[V/pC]	4.1 (7.5)

5.2.5 References

[1] D. Boussard, “Performance of the LEP2 SRF System,” *Proc. of the 1997 Part. Accel. Conf.*, pp. 2879-2883.

[2] P. Brown et al., “Performance of the LEP200 Superconducting RF System,” *Proc. of the 9th Workshop on RF Superconductivity*, 1-5 November 1999, Santa Fe, NM, USA.

[3] B. Aune et al., “Superconducting TESLA Cavities,” *PRST-AB* **3**, 092001 (2000).

[4] D. Proch, “Superconducting cavities for accelerators,” *Rep. Prog. Phys.* **61** (1998) 431-482.

[5] S. Bauer et al., “Production of Nb/Cu Sputtered Superconducting Cavities for LHC,” *Proc. of the 9th Workshop on RF Superconductivity,* 1-5 November 1999, Santa Fe, NM, USA.

[6] H. Padamsee, “SRF for Muon Colliders,” *Proc. of the 9th Workshop on RF Superconductivity*, 1-5 November 1999, Santa Fe, NM, USA.

[7] A.V. Novokhatski, “On the estimation of the wake potential for an ultrarelativistic charge in an accelerating structure,” Preprint INP 88-39.

[8] S.A. Heifets and S.A. Kheifets, “Coupling impedance in modern accelerators,” *Rev. Mod. Phys*. **63** (1991) 631-673.
[9] S. Belomestnykh et al., “Comparison of the Predicted and Measured Loss Factor of the Superconducting Cavity Assembly for the CESR Upgrade,” *Proc. of the 1995 Part. Accel, Conf.,* Vol. 5, pp. 3394-3396.
[10] T. Tajima et al., “Development of HOM Damper for B-Factory (KEKB) Superconducting Cavities,” *Proc. of the 1995 Part. Accel, Conf.*, p. 1620.
[11] E. Haebel et al., “The Higher-Order Mode Dampers of the 400 MHz Superconducting LHC Cavities,” *Proc. of the 8th Workshop on RF Superconductivity*, 1997.
[12] F. Pedersen, “RF Cavity Feedback,” *Proc. of the “B-Factories: The State of the Art in Accelerators, Detectors and Physics,”* pp. 192-207.

6 CONCLUSIONS

This Workshop was extremely useful in fleshing out many of the details related to the VLLC. For example, at the workshop it became very clear that the large machine could not provide high luminosity polarized beams at both the Z_0 pole and at high energy, and it would be best to provide the Z_0 factory function in the injector. In addition, the workshop identified a number of topics for further R&D. A list of some of these topics follows:

- What is the lower limit on β_y^* in the high energy collider?
- What is a reasonable upper limit on the beam-beam parameter at 183 GeV?
- Is there a way to coalesce electron bunches at high energy to finesse the TMCI current limit at injection, allowing a smaller beam pipe aperture to be used?
- Can feedback systems be useful to combat the TMCI instability at injection?
- In the 45 GeV Z^0 factory, are two rings essential?
- Are wigglers essential for polarization in the Z^0 factory?
- How can polarization at high energies be optimized?
- What is the optimum method of pumping the long vacuum chamber sections?
- How much cost and power minimization is possible in the complete design? What is the cost of the final system?
- How can the low field magnets be optimized (alloys, lamination shapes, etc.)?
- How do we get adequate shielding of the beam from the environment?
- How can we eliminate the Q-slope in superconducting rf cavities using sputtered niobium on copper?

It is hoped the VLLC concept will be explored further, and some of these questions will be addressed, at the Snowmass 2001 Workshop.

Beam-Beam Considerations for a VLLC

Richard Talman
Laboratory of Nuclear Studies
Cornell University
Ithaca NY 14853

Abstract

These notes concern miscellaneous issues relevant to a VLLC e+/e- collider. The focus is on beam-beam and IR design issues. (i) The first half of the report (presented at the workshop) describes a theory of beam-beam induced beam distortion in an e+/e- circular collider. Because the beams are ribbon-shaped, much wider than they are high, the fundamental process is parametric pumping of vertical betatron motion by (inexorable) horizontal betatron motion. This mechanism causes the beam height to increase proportional to beam current I, with the consequence that the luminosity is proportional to I, rather than the I^2 dependence that undistorted beam profiles would yield. This report is highly informal and preliminary and is intended primarily to be helpful in organizing further studies.

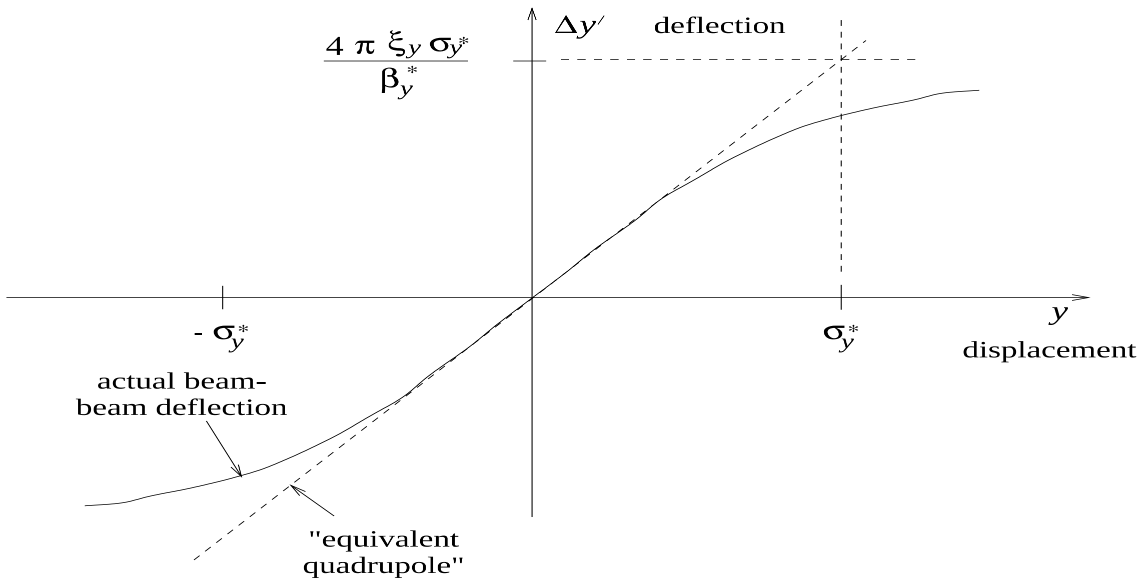

Figure 1: Dependence of vertical deflection $\Delta y'$ on vertical displacement y. The deflection of an "equivalent" quadrupole of strength $q = 4\pi\xi_y/\beta_y^*$ is also shown.

1 The Beam-Beam Deflection

The dependence of vertical beam-beam deflection $\Delta y'$ on vertical displacement y is shown in Fig. 1. The beam-beam tune shift parameter ξ_y is defined to be the tune shift caused by this force acting on a small amplitude particle. The angular deflection $\Delta y'$ and the tune shift ΔQ_y caused by a quadupole of strength q at a place where the beta function is β_y^* are given by

$$\Delta y' = qy, \quad \text{and} \quad \Delta Q_y = \frac{\beta_y^* q}{4\pi} \; . \tag{1}$$

Eliminating q from these relations, and using $\Delta Q_y = \xi_y$, yields the formula

$$\Delta y' = \frac{4\pi\xi_y}{\beta_y^*}\, y \; . \tag{2}$$

This dependence is labelled "equivalent quadrupole" in the figure.

Consider a "typical particle" for which the vertical phase space components, just before colliding with the opposing bunch, are $y = \sigma_y^*$, $y' = 0$, so its Courant-Snyder invariant is $\epsilon_{y,CS} = {\sigma^*}_y^2/\beta_y^*$. The graph shows that in passing through the other beam at the intersection point (IP), the particle's deflection is (almost) $4\pi\xi_y\sigma_y^*/\beta_y^*$. For this particle the effect of the beam-beam impulse on the Courant-Snyder invariant is

$$\epsilon_{y,CS} \rightarrow \frac{{\sigma^*}_y^2}{\beta_y^*} + \beta_y^* \,(\frac{4\pi\xi_y}{\beta_y^*})^2\, {\sigma^*}_y^2 = \epsilon_{y,CS}\,(1 + (4\pi\xi_y)^2) \; . \tag{3}$$

A tune shift parameter $\xi_y \approx 1/(4\pi)$ therefore causes a a rough doubling of the Courant-Snyder invariant of the particle. This formulation makes it all the more impressive when tune shifts approaching 0.1 are achieved, for example with flat beams at LEP and round beams at CESR. It seems that the beam-beam tune shift parameter might better have been defined with an extra factor of 4π since that would yield the mnemonically more satisfactory value of 1 as the tune shift parameter that causes a rough doubling of the Courant-Snyder invariant. As ξ is in fact defined, it is therefore important to keep in mind that $\xi = 0.1$ is a *big* value.

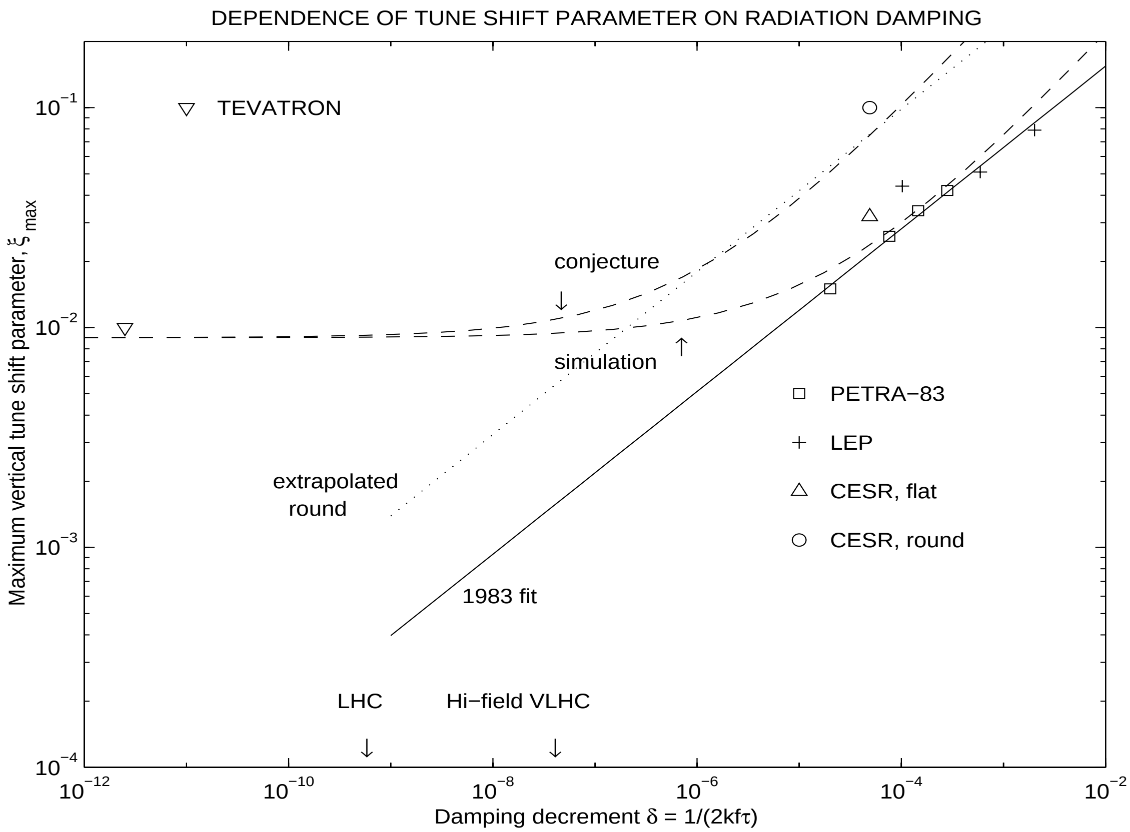

Figure 2: Dependence of maximum vertical tuneshift parameter $\xi_{\rm max}$ on damping decrement $1/(2kf\tau)$, where k is number of bunches, f is revolution frequency, and τ is damping time. The line labeled "1983 fit" was conjectured in 1983 by Keil and Talman based on data available at the time; it describes recent LEP data well. The curve labeled "simulation" linking the ultralow (proton) and ultrahigh (electron) regions is due to Peggs. The curve labeled "conjecture" is my fit (adjusting a parameter in the Peggs formula) to the Tevatron point and a (slightly downward adjusted) round beam CESR point.

2 Beam-Beam Observations from Existing Storage Rings

Fig. 2 shows beam-beam tune shift data, available in 1983, from PETRA and CESR, extrapolated in both directions, to predict performance of VLHC (protons) and VLLC (electrons). Subsequent performance of LEP (for which the analysis was originally performed) fits the extrapolation rather well. The maximum tune shift parameter for VLLC is predicted to be about $\xi_y^{\rm max} \approx 0.12$.[1]

The maximum beam-beam tune shift parameter is expected, and observed, to be greater with round than with flat beams. See Fig. 3.

Other data from existing colliding rings is shown in Fig. 4 and Fig. 5. Comments concerning the relevance to the present paper are given in the captions. In an ideal (perfectly decoupled) ring the beam width is much greater than the beam height. Since the horizontal motion is "hot" and the vertical "cold" any mechanism that couples these motions tends to affect the vertical motion a lot, and the horizontal motion hardly at all.

The important beam-beam phenomenology is that, when colliding with the other beam, the horizontal beam distributions is largely independent of beam current, but, above some threshold, the beam height increases proportional to beam current. This causes the beam-beam tune shift parameter

[1] Though the extrapolation to high damping decrement should be reliable, it is clear that the extrapolation toward zero decrement is not—hadron/hadron performance in existing rings contradicts it.

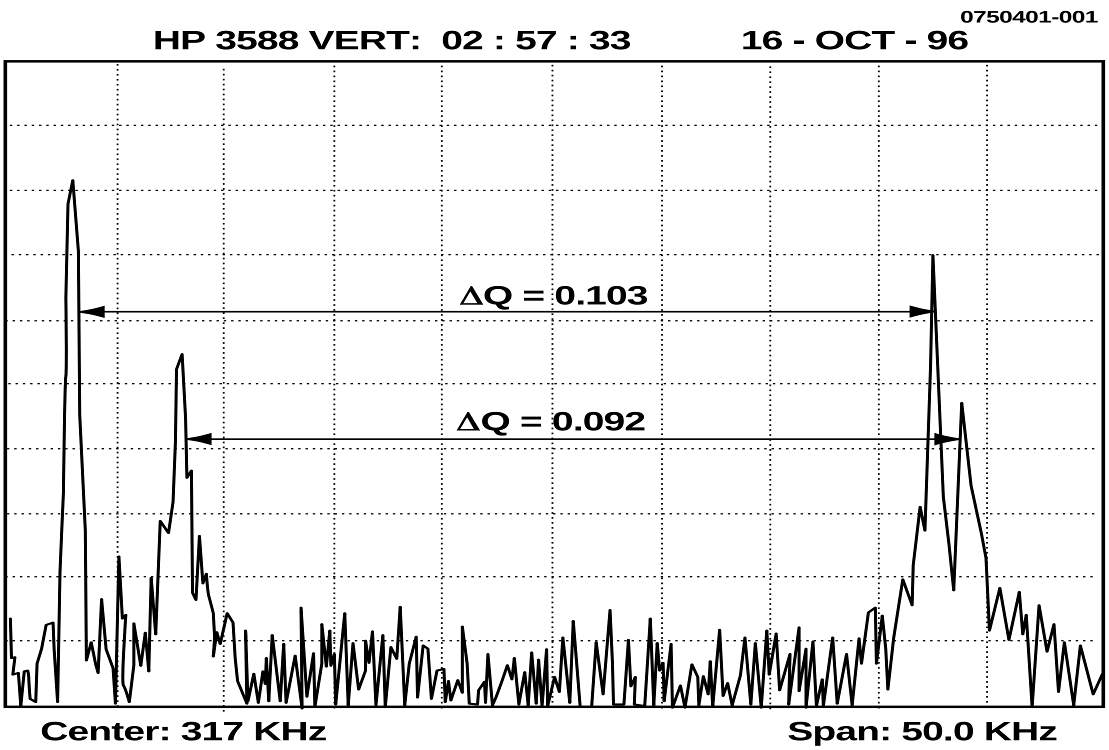

Figure 3: Tune shift parameter achieved with round beams at CESR. The beam-beam parameter ξ_y is proportional to the so-called $\pi \quad \sigma$ coherent beam-beam tune splitting exhibited in this data. After applying various (difficult, but by now fairly well established theory) the value extracted is $\xi_y = 0.09 \pm 0.1$. That is, the constant of proportionality is slightly less than one. See Elizabeth Young's Cornell PhD thesis.

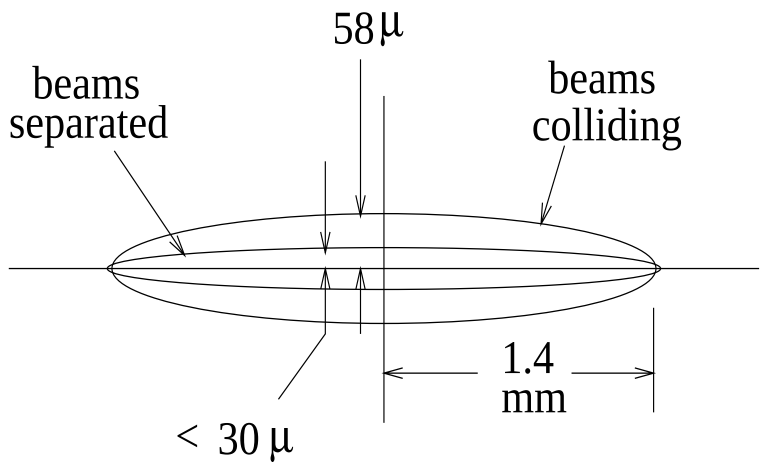

Figure 4: Beam profiles (represented by ellipses through r.m.s. sizes) measured using synchrotron light impinging on video camera during operation of CESR. The r.m.s. beam heights with beams not in collision were not greater than $30\,\mu$, the optical resolution of the viewing apparatus. That the horizontal profiles are unaffected corresponds to the assumption in the text that this motion is "inexorable". The beam height enlargement is claimed to be due to "parametric pumping" of vertical oscillations by the horizontal oscillations.

to "saturate" and no longer increase with increasing beam current. This behavior at LEP is exhibited in Fig. 5, copied from D. Brandt et al. According to the theory in this paper, this behavior would set in already at arbitrarily small beam current in a perfect ring but this behavior is masked by any beam height present due to single beam coupling. This is supported by observed behavior in which improving the decoupling reduces the threshold current at which saturation sets in. When running LEP at highest energy, 100 Gev, the coupling coeffient was $\kappa = 0.8\%$, and no saturation was observed up to the highest possible beam current.

3 Excitation of Vertical Betatron Motion by an External Shaker

Before introducing beam-beam deflections, let us analyse the vertical motion induced by the "direct drive" due to an external "shaker". As well as introducing the method of analysis and the equations of motion, this introduces the important damping decrement δ_y and shows how it influences the motion. It will, however, turn out that the influence of δ_y on parametric drive (the main topic of the first half of this report) is very different from its influence on direct drive (the topic of this section.) I make no great claims for the value of this section in analyzing beam transfer function measurements.

The deflection caused by the external drive on the t'th turn is

$$\Delta y'_t = F_E \cos \mu_E t. \tag{4}$$

We postulate a small "damping decrement" δ_y, so that the once-around transfer map in "Twiss form" is

$$\begin{pmatrix} y \\ y' \quad \Delta y'/2 \end{pmatrix}_{t+1} = \exp(\quad \delta_y) \begin{pmatrix} C_y + \alpha_y S_y & \beta_y S_y \\ \gamma_y S_y & C_y \quad \alpha_y S_y \end{pmatrix} \begin{pmatrix} y \\ y' + \Delta y'/2 \end{pmatrix}_t \tag{5}$$

and a similar equation can be written for backwards propagation from t to $t \quad 1$. Note that y' is evaluated at the middle of the shaker. We are using the notation $C_y \equiv \cos \mu_y$ and $S_y \equiv \sin \mu_y$ and are intentionally using the subscript t as a turn index to be suggestive of the time measured in units of the revolution period. It will however always be an integer. For these two maps the top equations

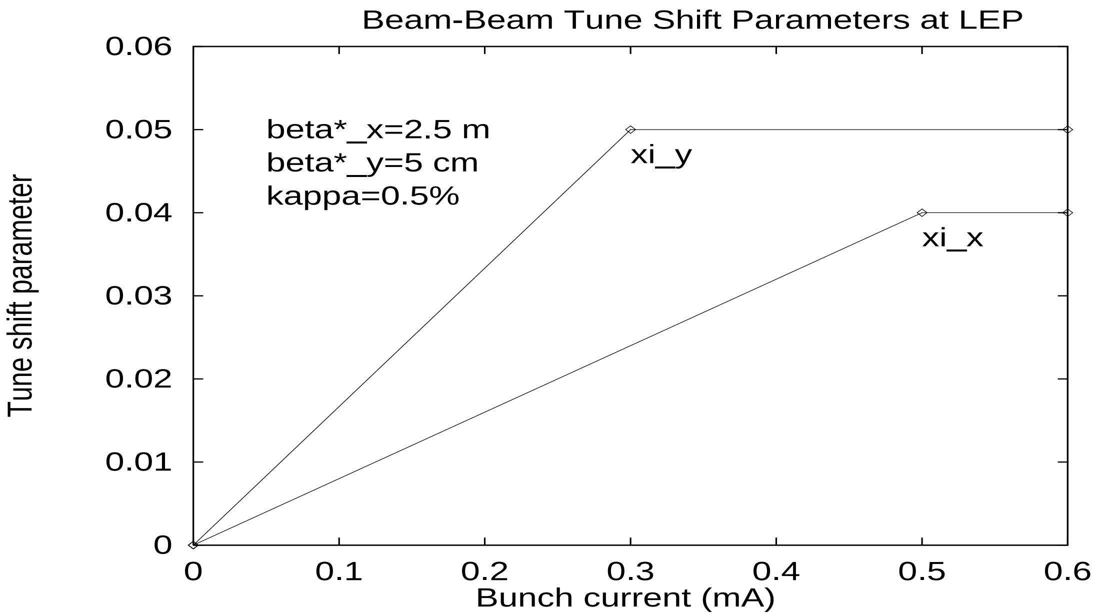

Figure 5: Dependence of ξ_x and ξ_y on beam current. Data from LEP running at 65 GeV, D. Brandt et. al., Rep. Prog. Phys. **63** (2000) 939-100. Similar behavior is observed at CESR, though saturation of ξ_x (with increasing current) is not observed at CESR. Furthermore, saturation of ξ_y had not been observed at LEP at highest energy, up to operationally practical beam currents.

are

$$
\begin{aligned}
y_{t+1} &= \exp(-\delta_y)[(C_y + \alpha_y S_y)y_t + \beta_y S_y (y' + \Delta y'/2)_t] && (6)\\
y_{t-1} &= \exp(+\delta_y)[(C_y - \alpha_y S_y)y_t - \beta_y S_y (y' - \Delta y'/2)_t] && (7)
\end{aligned}
$$

By treating δ_y as small and by addition of the equations Eq. 7 one eliminates y' and obtains

$$
y_{t+1} - 2C_y y_t + y_{t-1} = \beta_y S_y \Delta y'_t - \delta_y (y_{t+1} - y_{t-1}) \tag{8}
$$

After solving this for y_t it will be possible to obtain y'_t from the equation

$$
y'_t = \frac{y_{t+1} - y_{t-1} - 2\alpha_y S_y y_t + \delta_y (y_{t+1} + y_{t-1})}{2\beta_y S_y} \tag{9}
$$

which is obtained by subtracting Eqs. 7.

As usual with driven oscillations we expect a response at the drive frequency. i.e.

$$
y_t = A\cos\mu_E t + B\sin\mu_E t \tag{10}
$$

where any "transient" (i.e. any solution of the homogeneous equation which is obtained by setting the drive term of Eq. 8 to zero.) has been neglected. In electron accelerators this neglect is justified by the existence of true damping. Even in proton accelerators where true damping is negligible, it can be justified by decoherence, or, as it is called, Landau damping. Substituting into Eq. 8 and equating the "in-phase" and the "out-of-phase" coefficients separately to zero, one obtains

$$
\begin{aligned}
A &= \frac{\beta_y S_y (C_E - C_y)/2}{(C_E - C_y)^2 + \delta_y^2 S_E^2} F_E \\
B &= \frac{\beta_y S_y S_E \delta_y/2}{(C_E - C_y)^2 + \delta_y^2 S_E^2} F_E && (11)
\end{aligned}
$$

For near-resonance analysis we define

$$
\varepsilon = \mu_E - \mu_y \tag{12}
$$

(Be sure not to misinterpret frequency difference ε as an emittance, for which the symbol is ϵ.) Substituting into Eq. 10 and neglecting terms containing $\varepsilon\delta_y$ we obtain

$$
\begin{aligned}
y_t &= \frac{F_E\beta_y/2}{\varepsilon^2+\delta_y^2}\,[\quad \varepsilon\cos\mu_E t + \delta_y \sin\mu_E t] \\
&= \frac{F_E\beta_y}{2\sqrt{\varepsilon^2+\delta_y^2}}\,\cos(\mu_E t+\phi)\ ,
\end{aligned}
\tag{13}
$$

where $\phi = \tan^{\ 1}(\delta_y/\varepsilon)$, $\sin\phi = \delta_y/\sqrt{\varepsilon^2+\delta_y^2}$, and $\cos\phi = \varepsilon/\sqrt{\varepsilon^2+\delta_y^2}$. Taking $\alpha_y = 0$, the slope is given by

$$
\begin{aligned}
y'_t &= \frac{F_E/2}{\varepsilon^2+\delta_y^2}\,(\delta_y\cos\mu_E t + \varepsilon\sin\mu_E t) \\
&= \frac{F_E}{2\sqrt{\varepsilon^2+\delta_y^2}}\,\sin(\mu_E t+\phi)\ .
\end{aligned}
\tag{14}
$$

These equations should be reminiscent of driven simple harmonic motion though they are the solution of the difference equations Eq. 5. Except nearly on resonance, the "in-phase" $\cos\mu_E t$ term of Eq. 13 is dominant, but for small ε, the "out-of-phase" $\sin\mu_E t$ dominates. The response always "lags", with phase angle ϕ varying from zero to $\ \pi$ as the drive frequency varies from zero to infinity. With $\phi = \ \pi/2$ at resonance, the response changes sign in passing from below to above the resonance.

The CS invariant of the motion is

$$
\epsilon_{y,CS} = \frac{\beta_y F_E^2/4}{\varepsilon^2+\delta_y^2}\ .
\tag{15}
$$

For small deflections the averaged change in $\epsilon_{y,CS}$ due to the shaker is

$$
\begin{aligned}
\langle\epsilon^{(S)}_{y,CS}\rangle \approx \langle 2y'_t\Delta y'_t\rangle &= \langle\frac{\beta_y F_E}{\varepsilon^2+\delta_y^2}\,(\delta_y\cos\mu_E t + \varepsilon\sin\mu_E t)\,F_E\cos\mu_E t\rangle \\
&= \frac{\beta_y F_E^2\delta_y/2}{\varepsilon^2+\delta_y^2}\ .
\end{aligned}
\tag{16}
$$

The averaged *fractional* change is therefore

$$
\frac{\langle\epsilon^{(S)}_{y,CS}}{\epsilon_{y,CS}\rangle = 2\delta_y\ .}
\tag{17}
$$

This can be compared to the fractional change due to damping

$$
\frac{\epsilon^{(D)}_{y,CS}}{\epsilon_{y,CS}} = \quad 2\delta_y\ .
\tag{18}
$$

The fact that these changes are equal but opposite is consistent with the equilibrium.

4 Centroid Response of a Bunch of Particles Having a Spread of Tunes

Suppose a beam bunch consists of N particles whose tunes, rather than being equal, are spread according to a given probability distribution. When expressed in terms of ε this probability distribution is $P_\varepsilon(\varepsilon)$. The response of the entire bunch is

$$
Y_t = \sum_{i=1}^{N} y_t(\varepsilon^{(i)}) = N\int_{\ \infty}^{\infty} P_\varepsilon(\varepsilon)\,y_t(\varepsilon)\,d\varepsilon\ .
\tag{19}
$$

If the tunes are distributed uniformly over range $\Delta\varepsilon$ this becomes

$$
Y_t \;=\; \frac{N}{\Delta\varepsilon}\,\frac{F_E\beta_y}{2}\,\delta_y\,\sin\mu_E t\int_{\ \Delta\varepsilon/2}^{\Delta\varepsilon/2}\frac{d\varepsilon}{\varepsilon^2+\delta_y^2}
$$

$$= \quad \frac{NF_E\beta_y}{\Delta\varepsilon}\ \tan^{\ 1}\frac{\Delta\varepsilon}{2\delta_y}\ \sin\mu_E t\ . \tag{20}$$

In the usual circumstance that $\delta_y << \Delta\varepsilon$, this becomes

$$Y_t \approx \frac{NF_E\beta_y\pi}{\Delta\varepsilon}\ \sin\mu_E t\ ; \tag{21}$$

in this case the response is independent of δ_y. This might suggest a similar independence of δ_y of the beam-beam equilibrium, but the next section will show this to be incorrect.

5 Parametric Excitation of Vertical Oscillations

The vertical beam-beam deflection, given previously by Eq. 2, actually depends also on the horizontal displacement. Because the beams are ribbon-shaped, and the horizontal profile is Gaussian the deflection is given by

$$\Delta y'_t = \frac{4\pi\xi_y}{\beta^*_y}\ \exp(\quad \frac{a_x^2\cos^2\mu_x t}{2\sigma_x^{*\,2}})\ y_t\ , \tag{22}$$

where ξ_y is now to be interpreted as the value of tune shift parameter at $x = 0$. It will be appropriate to Fourier expand the nonlinear exponential function;

$$\Delta y'_t = \frac{4\pi\xi_y}{\beta^*_y}\ (\sum_{n=0}^{\infty} B_n\cos(2n\mu_x t))\ y_t \tag{23}$$

The coefficients B_n can be evaluated using the following integral from Watson, *Bessel Functions,* 6.22(4);

$$I_{2n}(z) = \frac{1}{\pi}\int_0^{\pi} e^{z\cos\theta}\ \cos(2n\theta)\,d\theta\ . \tag{24}$$

What with frequency aliasing it is possible for one of the terms in this sum to "resonate" with a pre-existing vertical betatron oscillation;

$$y_t = a_t\ \cos((\mu_y+\varepsilon_n)t) + b_t\ \sin((\mu_y+\varepsilon_n)t) \tag{25}$$

where a_t and b_t are "variation of constants" coefficients whose variability is required to satisfy the equation of motion, but which are assumed to vary slowly with t; that is, their fractional changes per revolution are small compared to 1. If they are treated as depending on a continuous variable t, then

$$a_{t\pm1} \approx a_t \pm \dot{a}_t,\ \text{and}\ b_{t\pm1} \approx b_t \pm \dot{b}_t\ . \tag{26}$$

The "frequency offset" ε_n will be defined shortly. Combining Eqs. 23 and Eq. 25 yields

$$\begin{aligned}
\frac{\Delta y'_t}{4\pi\xi_y/\beta^*_y} &= \sum_{n=0}^{\infty} B_n\cos(2n\mu_x t)\,(a_t\ \cos((\mu_y+\varepsilon_n)t) + b_t\ \sin((\mu_y+\varepsilon_n)t)) \\
&= \sum_{n=0}^{\infty}\frac{B_n}{2}\,(a_n\cos((2n\mu_x \quad \mu_y \quad \varepsilon_n^{(\ )})t) \quad b_n\sin((2n\mu_x \quad \mu_y \quad \varepsilon_n^{(\ )})t)) \\
&\quad + \sum_{n=0}^{\infty}\frac{B_n}{2}\,(a_n\cos((2n\mu_x+\mu_y+\varepsilon_n^{(+)})t) + b_n\sin((2n\mu_x+\mu_y+\varepsilon_n^{(+)})t))
\end{aligned} \tag{27}$$

Because of aliasing, any one (or more) of these terms can potentially cause resonance, with the phase offset $\varepsilon_n^{(\pm)}$ quantifying the "distance from resonance". These angles are defined by the following modulo-π relations

$$\begin{aligned}
2n\mu_x+\mu_y+\varepsilon_n^{(+)} &= \quad (\mu_y+\varepsilon_n^{(+)}),\ \text{or}\ \varepsilon_n^{(+)} = n\mu_x+\mu_y\ , \\
2n\mu_x \quad \mu_y \quad \varepsilon_n^{(\ )} &= +(\mu_y+\varepsilon_n^{(\ )}),\ \text{or}\ \varepsilon_n^{(\ )} = n\mu_x \quad \mu_y\ ,
\end{aligned} \tag{28}$$

Presumably one of these possibilities for n and for $\pm$ will dominate over all others. From here on the index n will be taken to indicate this particular dominant case, and Eq. 27 becomes

$$\Delta y'_t = \frac{4\pi\xi_y}{\beta^*_y}\,\frac{B_n}{2}\,(a_n\cos((\mu_y+\varepsilon_n)t) \quad b_n\sin((\mu_y+\varepsilon_n)t))\ . \tag{29}$$

Setting δ_y temporarily to zero, Eq. 8 becomes

$$y_{t+1} - 2C_y y_t + y_{t-1} = S_y\, 2\pi\xi_y\, B_n \left(a_n \cos((\mu_y+\varepsilon_n)t) - b_n \sin((\mu_y+\varepsilon_n)t)\right) . \tag{30}$$

For substituting Eq. 25 into this equation, using Eqs. 26, we obtain

$$\begin{aligned}
y_{t+1} &= (a_t+\dot a_t)(\cos(\mu_y+\varepsilon_n)\cos((\mu_y+\varepsilon_n)t) - \sin(\mu_y+\varepsilon_n)\sin((\mu_y+\varepsilon_n)t)) \\
&\quad + (b_t+\dot b_t)(\sin(\mu_y+\varepsilon_n)\cos((\mu_y+\varepsilon_n)t) + \cos(\mu_y+\varepsilon_n)\sin((\mu_y+\varepsilon_n)t)) \\
y_{t-1} &= (a_t-\dot a_t)(\cos(\mu_y+\varepsilon_n)\cos((\mu_y+\varepsilon_n)t) + \sin(\mu_y+\varepsilon_n)\sin((\mu_y+\varepsilon_n)t)) \\
&\quad + (b_t-\dot b_t)(-\sin(\mu_y+\varepsilon_n)\cos((\mu_y+\varepsilon_n)t) + \cos(\mu_y+\varepsilon_n)\sin((\mu_y+\varepsilon_n)t))
\end{aligned} \tag{31}$$

Performing the substitution, and requiring that the sine and cosine terms vanish separately, yields the equations

$$\begin{aligned}
\dot a_t \sin(\mu_y+\varepsilon_n) - b_t\cos(\mu_y+\varepsilon_n) + C_y b_t - S_y\,\pi\xi_y\,B_n\,b_t &= 0 \\
\dot b_t \sin(\mu_y+\varepsilon_n) + a_t\cos(\mu_y+\varepsilon_n) - C_y a_t - S_y\,\pi\xi_y\,B_n\,a_t &= 0
\end{aligned} \tag{32}$$

We seek a solution for which a_t and b_t exhibit time dependence of the form $\exp(st)$;

$$\begin{aligned}
s\,a_t - \frac{\cos(\mu_y+\varepsilon_n) - C_y + S_y\,\pi\xi_y\,B_n}{\sin(\mu_y+\varepsilon_n)}\,b_t &= 0 \\
\frac{\cos(\mu_y+\varepsilon_n) - C_y - S_y\,\pi\xi_y\,B_n}{\sin(\mu_y+\varepsilon_n)}\,a_t + s\,b_t &= 0
\end{aligned} \tag{33}$$

The requirement for such a solution to exist is that the determinant formed from the coefficients must vanish; this yields

$$s^2 = -\frac{(\cos(\mu_y+\varepsilon_n) - C_y)^2 + (S_y\,\pi\xi_y\,B_n)^2}{\sin^2(\mu_y+\varepsilon_n)} \approx -\varepsilon_n^2 + \pi^2\xi_y^2\,B_n^2 . \tag{34}$$

In the last step it has been assumed that $\varepsilon_n << 1$. In this form the condition for *unstable* motion is that s^2 be positive, which requires

$$-\pi\xi_y\,B_n < \varepsilon_n < \pi\xi_y\,B_n . \tag{35}$$

By setting δ_y to zero we have been neglecting damping so far and have found that, even with no damping, if ε_n lies outside this range, the motion will be stable. That is to say that the horizontal oscillation will not "pump up" vertical oscillations. On the other hand, in an ideal electron storage ring, if there were no cross-plane coupling the vertical beam height would vanish. (This uses the result that synchrotron-radiated photons are emitted precisely in the forward direction. Since their typical angle is $1/\gamma$ this is an excellent, but not perfect assumption.) In this ideal limit $\xi_y = \infty$, so Eq. 35 would not be satisfied. In this limit the parametric pumping that is being described would presumably blow up the beam until condition Eq. 35 is satisfied.

In fact there *is* damping, as represented by $\delta_y \neq 0$. The threshold of instability is therefore determined by the condition that the (positive) growth rate given by Eq. 35 is equal to δ_y;

$$\sqrt{-\varepsilon_n^2 + \pi^2\xi_y^2\,B_n^2} = \delta_y, \quad \text{or} \quad \varepsilon_n = \sqrt{\pi^2\xi_y^2\,B_n^2 - \delta_y^2} . \tag{36}$$

The band of instability is therefore given by

$$-\sqrt{\pi^2\xi_y^2\,B_n^2 - \delta_y^2} < \varepsilon_n < \sqrt{\pi^2\xi_y^2\,B_n^2 - \delta_y^2} . \tag{37}$$

For $\delta_y > \pi|\xi_y B_n|$ there is no unstable band at all. I believe that this is where δ_y has its greatest influence on the beam-beam interaction for flat beams.

There is one way in which the growth derived so far is "too powerful". It is that the exponential growth, according to the solution so far, diverges to infinity, which disagrees with observation and is clearly unphysical. The effect, that has been left out so far, which moderates this behavior, is the nonlinearity as a function of y. (See Fig. 1.) As individual particles come into resonance their amplitudes build, but this growth is accompanied by detuning, that eventually defeats the resonance. When the resonance curve of a nonlinear oscillator becomes multiple valued, it is possible, when a particle's state has become unstable, for the particle to jump discontinuously to a stable point of different amplitude. Since this process is emittance nonconserving, it contributes to the growth of vertical beam size.

A dynamical theory that calculates the absolute beam size caused by these two effects (parametric pumping plus discontinuous jumps in Courant-Snyder invariant) is not available, but computer simulations have born out the essential features of this model with semi-quantitative accuracy.

6 Luminosity and Tune Shift Formulas

The beam-beam tune shift parameters are given by

$$\xi_{x,y} = \frac{I/B}{ef}\,\frac{r_e}{4\pi\gamma}\,\frac{\beta^*_{x,y}}{\sigma^*_x\sigma^*_{x,y}(1+R)}\ , \tag{38}$$

where R, the beam aspect ratio at the IP, is defined by

$$R = \frac{\sigma^*_y}{\sigma^*_x}\ , \tag{39}$$

I is the total beam current, B is the number of bunches, f is the revolution frequency, and $r_e = 2.82 \times 10^{\ 15}$ m is the classical electron radius.

In this section I will be considering only maximum luminosity conditions, so all quantities should implicitly be assumed to have superscript "max" attached to them. Part of the lore of the field is that the maximum luminosity is obtained when $\xi_x \approx \xi_y$. This is a plausible result, though, as far as I know, it is not backed up by sound theoretical understanding. It tends to be supported empirically, however, so I accept it to be true. It follows from Eq. 38 then, that

$$\frac{\beta^*_x}{\sigma^*_x} = \frac{\beta^*_y}{\sigma^*_y}\ . \tag{40}$$

We also know that

$$\epsilon_x = \frac{\sigma^{*\,2}_x}{\beta^*_x}, \quad \text{and} \quad \epsilon_y = \frac{\sigma^{*\,2}_y}{\beta^*_y}, \tag{41}$$

Combining Eqs. 40 and Eq. 41, we obtain

$$\frac{\epsilon_y}{\epsilon_x} = \frac{\sigma^*_y}{\sigma^*_y}, \tag{42}$$

and, finally, the remarkable set of equalities

$$R = \frac{\sigma^*_y}{\sigma^*_y} = \frac{\beta^*_y}{\beta^*_x} = \frac{\epsilon_y}{\epsilon_x}\ . \tag{43}$$

The luminosity with B bunches, each having current I/B is given by

$$\mathcal{L} = \frac{I}{4\pi\sigma^*_x\sigma^*_y}\,\frac{I/B}{ef}\,\frac{1}{e}\ . \tag{44}$$

Both Eqs 38 and Eq. 44 are valid for both flat beams and round beams. Combining them yields

$$\mathcal{L} = \mathcal{L}'\,\frac{\xi}{\beta^*_y}\,\frac{1+R}{2}\,I\ , \tag{45}$$

where

$$\mathcal{L}' = \frac{\gamma}{r_e e} = 2.2 \times 10^{34}\,\frac{\gamma}{10^5}\,\text{cm}^{\ 2}\text{s}^{\ 1}\ . \tag{46}$$

Formula Eq. 45 is tyrannical, responsive to increasing I or decreasing β^*_y but nothing else. For any next-generation e+/e- circular rings, the beam current I will be limited by RF power considerations. To achieve maximum specific luminosity (i.e. luminosity at given current), as well as minimizing β^*_y, it will be necessary to reduce B until the beam-beam tune shift "saturates" at that beam current—i.e. at a value of about $\xi = 0.12$ according to an earlier figure. Assuming flat beams, B will therefore be given by

$$B = \frac{1}{\xi}\,\frac{I}{ef}\,\frac{r_e}{4\pi\gamma}\,\frac{\beta^*_y}{\sigma^*_x\sigma^*_y}\ . \tag{47}$$

(Of course B has to be an integer and cannot be less than 1.)

There is a fallacious design prescription that crops up occasionally and suggests that cross-plane coupling (coefficient $\kappa = \epsilon_y/\epsilon_x$) should be intentionally introduced in order to achieve one of the equalities contained in Eqs 43. In fact, as has been explained in an earlier section, if the beam ribbons are thin enough, the beam height self-regulates itself by blowing up until the ξ "saturates" at its maximum possible value. Best luminosity is obtained by adjusting the non-interacting beam κ to be as close to zero as possible. This has been repeatedly born out at CESR. It looks to me as if the luminosity in the final days of LEP was somewhat lower than it could have been, perhaps because they did not have time to perform the machine studies necessary to reduce κ below 0.8%.

7 Comparison of Flat and Round Beam Operation

In pre-experiment contemplation of flat versus round beam operation of CESR the factors in Eq. 45 were considered individually, assuming I was to be held fixed. From comparative simulations the round beam maximum tune shift was predicted to be two or three times larger than the value for flat beams, and the $1 + R$ factor gives another factor of two. But studies of the IR optics showed that the minimum possible value of $\beta^* y$ was some two times smaller for flat than for round beams. On paper, therefore, round beams were expected to yield two or three times greater luminosity than flat beams. This was not born out by subsequent experimentation. In fact it was found that the maximum value of ξ_y (in Möbius operation at high beam currents) was considerably less than the round beam value. The difficulty was traced to synchrobetatron resonances. The degree to which this limitation is fundamental is unknown at this time, but the result of these observations was to discourage any further efforts to run CESR with round beams.

There is an argument due to Dave Ritson that exhibits a disadvantage round beams have relative to flat beams. This argument shows that the cone of trajectories leaving the IP has greater angle for round than for flat beams. To simplify the formulas, the following plausible relations are assumed:

$$\begin{aligned} \epsilon_{\rm rnd} &= \frac{1}{2}\epsilon_{x,\rm flat}, \\ \mathcal{L}_{\rm rnd} &= \mathcal{L}_{\rm flat}, \\ \xi_{\rm rnd} &= \xi_{\rm flat}, \\ I_{\rm rnd} &= I_{\rm flat}. \end{aligned} \tag{48}$$

The first of these occurs automatically if the flat and round beam lattices are more or less equivalent except at the IP. The third is pessimistic for round beams. Together, these relations imply

$$\beta^*_{y,\rm flat} = \frac{1}{2}\,\beta_{\rm rnd}\ . \tag{49}$$

This is consistent with practical IP designs as has been mentioned previously. Using Eq. 43 we compare the horizontal and vertical angular divergences of the flat beam as it emerges from the IP:

$$\left.\frac{\sigma^{*2}_{x'}}{\sigma^{*2}_{y'}}\right|_{\rm flat} = \frac{\epsilon_{x,\rm flat}/\beta^*_{x,\rm flat}}{\epsilon_{y,\rm flat}/\beta^*_{y,\rm flat}} = 1\ , \tag{50}$$

and obtain the possibly counter-intuitive result that they are equal—the cone evolves rapidly from highly elliptical to nearly round as it leaves the IP. Since the emergence cones are round for both flat and round beams, it is meaningful to compare their cone angles:

$$\left.\frac{\sigma^{*2}_{r'}}{\sigma^{*2}_{x'}}\right|_{\rm rnd/flat} = \frac{\epsilon_{\rm rnd}/\beta^*_{\rm rnd}}{\epsilon_{x,\rm flat}/\beta^*_{y,\rm flat}} = \frac{1}{4}\,\frac{\beta^*_{x,\rm flat}}{\beta^*_{y,\rm flat}}\ . \tag{51}$$

Since the final ratio of flat beam beta functions usually has a large value, such as 40, the divergence cone angle is some three times less for flat beams than for round beams. This argument may be especially important for IP designs with crossing angles.

A Very Large Lepton Collider in the VLHC tunnel

Tanaji Sen
FNAL, P.O. Box 500, Batavia, IL 60510
and
Jim Norem
HEP Division, ANL, Argonne, IL 60439

Abstract

The Very Large Hadron Collider (VLHC) design is converging on a program where a 233 km circumference tunnel would first be occupied by a low field dipole system producing 40 TeV in the center of mass, followed by a higher field magnet system producing nearly 200 TeV in the center of mass. We consider the possibility of first using the tunnel for a large e^+e^- collider, which could operate in the range $90 < E_{cm} < 400$ GeV. This device would be a relatively conservative extrapolation of LEP technology. We assume that the total radiated synchrotron power will be limited to 100 MW. We describe the design strategy, the luminosity and energy reach, the factors that limit the machine performance, the scaling laws that apply to its design, and the technology that would be required for its implementation.

Contents

1 Introduction

Plans for the future very large hadron collider (VLHC) now envisage a staging scenario [1] where a low field collider would be built first followed by a high field collider in the same tunnel several years later. There is also interest in an electron-positron collider in the same tunnel which could study physics that would complement the studies with the hadron collider. This machine could be used to, 1) examine the W and Z^o with high precision, to improve measurements of electroweak parameters by an order of magnitude, 2) study continuum fermion pair production, 3) produce clean Higgs mesons at an energy of perhaps 115 GeV, 4) measure the W mass from W pair production thresholds, and 5) look at the $t\bar{t}$ thresholds with very good energy resolution [2]. The very large circumference of the tunnel makes it possible to think of an $e^+ \quad e$ ring which could reach an energy about twice that of LEP if we limit the synchrotron radiation power to 100 MW. Compared to the NLC, the energy and luminosity reach of such a machine is lower. However the technology required is proven and available today. We believe that such a large lepton collider can be built with conservative assumptions and at a fraction of the current estimated cost of the NLC. In this paper we outline the design of this collider and consider some of the accelerator physics issues. We compare and contrast the parameters of this machine with LEP. Much of the material on LEP is obtained from a recent workshop on the subject of "e^+e in the VLHC" [3], and a recent paper by Brandt et al. [4]. We attempt to identify the mechanisms that will limit the performance of the collider and look at scaling laws for for the operation of such a machine at high energies. We also attempt to identify methods that could perhaps be used to both increase the performance of the machine and reduce the cost of the facility.

2 Design Strategy

Our design philosophy of this electron-positron collider will be to to avail of the maximum RF power available and operate at the beam-beam limit The synchrotron radiation power lost by *both beams*, each with beam current I is

$$P_T = 2C_\gamma \frac{E^4 I}{e\rho}\ , \quad C_\gamma = \frac{4\pi}{3}\frac{r_e}{(m_e c^2)^3} = 8.86 \times 10^{\ \ 5}\ [\mathrm{m/GeV}^3] \tag{2.1}$$

Assuming that there are M_b bunches in each beam with bunch intensities N_b, the luminosity is

$$\mathcal{L} = \frac{f_{rev}}{4\pi}\frac{M_b N_b^2}{\sigma_x^* \sigma_y^*} \tag{2.2}$$

We will assume flat beams so that $\sigma_y^* \ll \sigma_x^*$. With this assumption, the vertical beam-beam tune shift is

$$\xi_y = \frac{r_e}{2\pi}\frac{N_b \beta_y^*}{\gamma \sigma_x^* \sigma_y^*} \tag{2.3}$$

Eliminating one power of N_b from the expression for the luminosity, we can write

$$\mathcal{L} = \frac{1}{2 e r_e}\frac{\xi_y}{\beta_y^*}\gamma I \tag{2.4}$$

I is the beam current in a single beam. Our strategy as stated earlier is that as we change parameters, P_T and ξ_y will be held constant.

Using Equation (2.4) to eliminate the current, we obtain the following equation for the luminosity and energy in terms of the fixed parameters and the bending radius ρ,

$$\boxed{\mathcal{L}\gamma^3 = \frac{3}{16\pi r_e^2(m_e c^2)}\frac{\xi_y P_T}{\beta_y^*}\rho} \tag{2.5}$$

This equation relates the parameters important to the physics program viz. the luminosity and energy to the machine size, optics and beam parameters. For example at constant luminosity, this equation shows that the maximum allowable energy increases only with the cube root of the radius, the radiated power or the beam-beam parameter. In the above equation β_y^* may be assumed constant at different energies only if the IR quadrupoles do not pose an aperture limitation in the vertical plane at any energy. We will assume that to be the case.

Similarly Equation (2.5) shows that the luminosity of the collider at a given energy and radiated power P_T can only be increased by increasing the beam-beam tune shift, ξ_y and/or lowering β_y^*. Other limits can however prevent the machine from operating at the maximum theoretical luminosity, for example, limits on the the maximum current in each bunch at injection.

2.1 Bunch intensity limitations

The dominant limitation on the bunch intensity at collision energy arises due to the beam-beam interactions. We have incorporated this constraint in our scaling of the luminosity with energy, Equation (2.5). Another limitation that is more severe at injection energy is the Transverse Mode Coupling Instability (TMCI). As in the classical head-tail instability, synchrotron motion which exchanges particles in the head and tail of the bunch drives the instability but this instability can arise even with zero chromaticity. In the presence of transverse impedances (typically wall resistivity), the wake forces excited by particles in the head can exert strong enough forces on the tail such that betatron modes $\omega_\beta + m\omega_s$ are modified. Typically, at the threshold intensity of the instability, the modes $m = 0$ and $m = \;\; 1$ become degenerate. TMCI is known to limit the bunch current in LEP to below 1 mA [4].

The threshold bunch current is given by

$$I_b^{TMCI} \simeq \frac{8 f_{rev}\nu_s E}{e\sum_i \beta_i k_{\perp\, i}(\sigma_s)} \tag{2.6}$$

where ν_s is the synchrotron frequency, the sum in the denominator is over tranverse impedances and $k_{\perp\, i}$ is a bunch length dependent transverse mode loss factor. Obviously higher synchrotron frequencies and longer bunches increase the threshold intensity. At LEP larger RF voltages are used to increase ν_s while emittance wigglers are used to increase the bunch length at the injection energy of 20 GeV. Compared to LEP, the very large lepton collider has a revolution frequency that is an order of magnitude smaller while the synchrotron frequency, injection energy and bunch length are comparable. If the impedances in LEP and this large ring are comparable, we may expect an order of magnitude reduction in the threshold current for this ring.

E. Keil[6] and G. Dugan[7] have done rough estimates of the threshold current for this large collider following the model of LEP. The dominant sources of broadband impedance will be the RF cavities, bellows and the resistive wall. LEP has bellows placed every 10 m around the ring. Assuming a similar placing and the same loss factors of the cavities and bellows as in LEP, the loss factor in the bellows would be an order of magnitude larger than that in the cavities. At a bunch length of 1 cm the threshold current would reduce to around 0.01 mA. The number of bellows therefore should be kept to a minimum. Improvements in the vacuum system design may in fact allow the complete elimination of these bellows or at least to space them every km or so (see Section 10). In this case, the cavities and the resistive wall contribute about equally to the loss factor in this large ring. Dugan estimates that at an injection energy of 45 GeV (this will be discussed in Section 7) and in an elliptical chamber with aspect ratio of 2.5, the threshold current, I_b^{TMCI}, will be above 0.2 mA if the chamber half-height exceeds 4.8 cm. We will assume a design current of 0.1 mA to allow for a safety margin of 100%. It is worth noting that various schemes have been proposed to combat TMCI for the low-field hadron collider [8], e.g. starting with lower intensity bunches at injection energy and coalescing at higher energy, feedback systems etc. If required we may also use of one of these compensation schemes to allow a bunch current of 0.1 mA.

2.2 Beam intensity limitations

The available RF power determines the beam current to zeroth order. This constraint will be used in the design strategy in this report. However there are other sources of limitations which need to be considered as the design evolves. Perhaps the most important of these secondary limitations is the available cryogenic cooling power. We will assume that superconducting cavities will be used. The dynamic heat load on these cavities includes contributions from the RF dissipation and the beam induced heat load from both beams. These two sources lead to a power dissipation given by

$$P_{dynamic} = N_{cav}\frac{V_{RF}^2}{(R/Q)Q} + 2R_m(\sigma_s)I_bI_e \tag{2.7}$$

where N_{cav} is the number of cavities, (R/Q) is the normalized shunt impedance per cavity, Q is the unloaded quality factor of the cavities which depends on the operating temperature and the field gradient, R_m is a bunch length dependent loss impedance of the cavities, I_b is the bunch current, I_e is the single beam current. The available cryogenic power must be sufficient to cope with this load which has a contribution that increases with the beam current. The total higher order mode (HOM) power $P_{HOM} \propto I_bI_e$ that could be absorbed by the superconducting cavities was another restriction on the total beam current at LEP. An upgrade of the couplers and RF cables was required to cope with this limitation. Clearly the design of the cavities for the future lepton collider should take advantage of the experience gained while operating LEP.

2.3 Synchrotron radiation power and beam-beam limited regime

Here we specify the design strategy keeping the beam-beam parameter and the synchrotron radiation power constant. The beam-beam parameter depends on the bunch intensity while the power depends on the beam intensity. Hence we will determine the bunch intensity N_b from ξ_y and the number of bunches M_b from P_T while ensuring that the maximum bunch intensity stays below the threshold required to avoid the transverse mode coupled instability.

Writing the emittances in the transverse planes as

$$\epsilon_y = \kappa\epsilon_x$$

where κ is the coupling ratio, the bunch intensity can be expressed as

$$N_b = \left(\frac{2\pi}{r_e} \sqrt{\frac{\kappa \beta_x^*}{\beta_y^*}} \xi_y \right) \gamma \epsilon_x \tag{2.8}$$

where the factors within brackets are assumed to stay constant. One could imagine another scenario with optics changes where $\beta_x^*, \beta_y^*, \kappa$ are allowed to vary.

The equilibrium emittance ϵ_x is determined by the equilibrium between damping and quantum fluctuations and is given approximately by

$$\epsilon_x = \frac{C_q}{J_x} \frac{R}{\rho} \frac{\gamma^2}{\nu_x^3} \, , \qquad C_q = \frac{55 \hbar c}{32\sqrt{3}(m_e c^2)} = 3.83 \times 10 \ {}^{13}[\mathrm{m}] \tag{2.9}$$

Here R is the average radius of the arc assumed to be made of periodic structures such as FODO cells and ν_x is the arc tune. If L_c, μ_c are the length of each periodic cell and the phase advance over the cell respectively, then

$$\nu_x = \frac{2\pi R}{L_c} \frac{\mu_c}{2\pi} = R \frac{\mu_c}{L_c} \tag{2.10}$$

Hence

$$\epsilon_x = \left(\frac{C_q}{J_x} \frac{R}{\rho} \left[\frac{L_c}{\mu_c} \right]^3 \right) \frac{\gamma^2}{R^3} \tag{2.11}$$

The factor R/ρ - the ratio of the arc radius to the bend radius - can be treated as constant. Typically it has a value somewhere between 1.0 and 1.25. The arc radius is determined from the machine circumference C in terms of a filling factor f_1. Thus

$$R = f_1 \frac{C}{2\pi} \, , \quad \text{and} \quad \rho = f_2 R \, , \qquad f_1, f_2 < 1 \tag{2.12}$$

where f_1, f_2 are held constant. Since we do not make optics changes at different stages, we will treat the factor in brackets in Equation (2.11) as constant. The energy in this relation is of course determined from the energy luminosity relation Equation (2.5). Once the emittance is known, the bunch intensity is calculated from Equation (2.8).

The beam current I and the number of bunches are related as $I = e f_{rev} M_b N_b$, hence the maximum number of bunches is found from the total synchrotron radiation power as

$$M_b^{max} = \left(\frac{P_T}{2C_\gamma} \right) \frac{\rho}{f_{rev} N_b E^4} \tag{2.13}$$

The factors in brackets are constant while the other factors change with the machine circumference.

2.4 RF parameters

There are two requirements on the RF voltage parameters. The first requirement on the voltage is that the energy gained due to the RF per turn must equal to the energy lost per turn.

$$e V_{RF} \sin \phi_s = U = C_\gamma \frac{E^4}{\rho} \tag{2.14}$$

where $C_\gamma = (4\pi/3)r_e/(m_e c^2)^3 = 8.86 \times 10^{-5}$ m/GeV^3. The second requirement is that the RF acceptance ΔE_{RF} must be a certain number, say N_{QL}, times the rms energy spread σ_E for an acceptable quantum lifetime,

$$\Delta E_{RF} = N_{QL}\sigma_E \tag{2.15}$$

or

$$\sqrt{\frac{1}{\pi h \eta_{slip}} e V_{RF} E G(\phi_s)} = N_{QL}\sqrt{\frac{C_q}{J_s \rho}}\frac{E^2}{m_e c^2} \tag{2.16}$$

where

$$G(\phi_s) = 2\cos\phi_s - (\pi - 2\phi_s)\sin\phi_s \tag{2.17}$$

J_s is the longitudinal damping partition number. Typically we require $N_{QL} \sim 10$. These two conditions can be solved to find the synchronous phase as the solution of the transcendental equation

$$\cot\phi_s + \phi_s - \frac{\pi}{2} - \frac{55\sqrt{3}}{256}\frac{h\eta_{slip}}{J_s\alpha_f}\frac{N_{QL}^2}{\gamma} = 0 \tag{2.18}$$

where $\alpha_f = e^2/(4\pi\epsilon_0\hbar c) = 1/137.04$ is the fine structure constant. This equation can be solved numerically. Once the synchronous phase is known, the RF voltage can be found from Equation (2.14).

The RF frequency or the harmonic number is related to the desired bunch spacing. In order to accomodate both beams symmetrically around the ring, it is required that the bunch spacing be an even multiple of the RF wavelength. This in turn requires that the harmonic number be an even multiple of the number of bunches. The choice of RF frequency influences the energy acceptance $(\Delta E/E)_{accep}$ because $(\Delta E/E)_{accep} \propto 1/\sqrt{h}$ so lower RF frequencies increase the acceptance. However two economical factors argue for higher frequencies: (1) smaller frequencies increase the size and hence the cost of the cavity and (2) high power klystrons are more cost effective above frequencies of 300 MHz. In superconducting cavities the frequency is limited from above by several factors: (1) cavity losses increase with frequency, (2) longitudinal and transverse shunt impedances scale like ω_{RF} and ω_{RF}^2 respectively, (3) the ratio of the energy removed by a bunch from the cavity to the stored energy in the cavity also increases with frequency. In this paper we will consider RF frequencies in the neighbourhood of 400 MHz.

As an example, consider a circumference of 233km. We will develop a parameter list based on this circumference. We will assume a total synchrotron radiation power of 100 MW and a beam-beam parameter $\xi_y = 0.1 - 0.14$. The maximum number of bunches M_B^{max} determined by Equation (2.13) is 126. The revolution frequency is 1.315 kHz and the harmonic closest to 400 MHz is 310882 = $2 \times (15541)$. This does not have many divisors so a more convenient harmonic number is 310896 = $2 \times (4 \times 9 \times 17 \times 127)$. If we accept the requirement that $h = 2nM_B$, the allowed number of bunches less than M_B^{max} are all products of $(2, 2, 2, 3, 3, 17)$ less than 126.

2.5 Optics

2.5.1 Arc optics

The choice of phase advance per cell μ_c and the length of a cell L_c are crucial design parameters. The equilibrium emittance decreases as the phase advance increases, reaches a minimum at 135° and then increases again at larger values of μ_c. The horizontal dispersion also decreases with increasing phase advance and shorter cell lengths. Conversely, stronger focusing also increases the chromaticity and hence the strength of the sextupoles required to correct the chromaticity. Strong sextupoles can limit the available dynamic aperture. For these reasons, the choice of phase advance per cell in electron machines is usually limited in the range of $60^\circ \le \mu_c < 120^\circ$. For example, LEP started operation with $(60^\circ, 60^\circ)$ phase advances in the (x, y) planes at 45 GeV, and since then has used $(90^\circ, 60^\circ)$, $(90^\circ, 90^\circ)$ and $(102^\circ, 90^\circ)$ phase advances at higher energies.

Another parameter affected by the choice of optics is the threshold current for TMCI. From Equation (2.6) we observe that $I_{thresh}^{TMCI} \propto \nu_s/(\sum_i \beta_i k_{\perp\, i})$. To estimate the dependence on μ_c, L_c we replace β_i by the average value in a FODO cell $\langle\beta\rangle = L_c/\sin\mu_c$. The synchrotron tune $\nu_s \propto \sqrt{\alpha_C}$ where α_C is the momentum compaction. Since $\alpha_C \propto 1/\sin^2(\mu_c/2)$, we find

$$I_{thresh}^{TMCI} \propto \frac{\nu_s}{\langle\beta\rangle} \propto \frac{1}{L_c}\cos\left(\frac{\mu_c}{2}\right) \tag{2.19}$$

Hence the TMCI threshold is raised with shorter cell lengths and smaller phase advance per cell.

In this paper we will choose the phase advance per cell $\mu_c = 90^\circ$ and then choose a cell length L_c so that the bunch intensity does not exceed a certain threshold set by the TMCI. We will develop parameter sets (luminosity, energy, RF voltages,...) for different machine circumferences in this paper. As we increase the ring circumference μ_c, L_c will be assumed constant while the revolution frequency decreases and the bunch intensity always stays below the TMCI threshold.

The phase advance per cell is one way of controlling the equilibrium emittance. Another way is to redistribute the equilibrium emittance between the horizontal and longitudinal planes by changing the RF frequency. In an lattice constructed entirely of FODO cells, the change of partition number with momentum deviation is given by

$$\frac{dJ_x}{d\delta} = \quad \frac{dJ_s}{d\delta} = \quad 4\frac{L_D}{L_Q}\left[\frac{2 + \frac{1}{2}\sin^2\mu_C/2}{\sin^2\mu_C/2}\right] \tag{2.20}$$

where L_D, L_Q are the length of dipoles in a half cell and length of a quadrupole respectively. Writing $J_x(\delta) = J_x(0) + (dJ_x/d\delta)\delta + \ldots$, we observe that reducing the emittance ϵ_x by half requires increasing the damping partition number to $J_x(\delta) = 2J_x(0)$ or a momentum shift of $\delta_{\Delta J_x = 1} = 1/(dJ_x/d\delta)$ if initially $J_x(0) = 1$. The required RF frequency shift is related to the momentum deviation δ by

$$\frac{\Delta f_{RF}}{f_{RF}} = \quad \frac{\Delta R}{R} = \quad \alpha_C\delta \tag{2.21}$$

While the horizontal emittance can be changed by an appropriate shift in RF frequency, there is also a change in the radial excursion ΔR of the beam. It is important to keep this as small as possible both to minimize a loss in physical aperture and avoid a significant reduction in the transverse quantum lifetime. A lower phase advance per cell and a shorter quadrupole length relative to the dipole length, i.e. weaker focusing, help to keep the relative change in RF frequency and radial excursion small. As an example we consider the 233 km ring whose parameters will be given later in Section 6. With $L_D = 94.70$ m, $L_Q = 0.49$ m, $\mu_C = 90^\circ$, $\alpha_C = 0.23 \times 10^{\ \,4}$, we find the damping aperture to be $\delta_{\Delta J_x = 1} = 2.9 \times 10^{\ \,4}$. The corresponding radial excursion is about $\Delta R = 0.20$ mm. Since this changes the damping partition number by one, we can write this as the change in damping partition per unit of radial excursion,

$$\frac{\Delta J_x}{\Delta R} = 5.0 \ /[\mathrm{mm}]$$

Thus radial excursions of the closed orbit by only fractions of a mm are sufficient to change the damping partition number by a unit or more.

An alternative method of reducing the transverse emittances is to place a damping wiggler in a region where the dispersion vanishes. Conversely the emittance could be increased if required, e.g. to reduce the beam-beam tune shift, by placing the wiggler where the dispersion is non-zero.

If the horizontal emittance is reduced by any method, the energy spread increases which decreases the energy resolution of the experiments and also the longitudinal quantum lifetime if the RF voltage is kept constant. This places constraints on the allowed emittance manipulations.

Synchrotron radiation in quadrupoles may be an issue. If the gradient is sufficiently large, then paricles with large betatron amplitudes may radiate enough energy that they are lost from the RF bucket. This was termed the radiative beta-synchrotron coupling (RSBC) [9]. A rough measure of this effect [11] is the ratio of the field in a quadrupole at an amplitude equal to the rms beam size to the dipole bend field. To ensure that this effect is within bounds, the quadrupole gradient will be limited from above by requiring that this ratio not exceed unity.

2.5.2 Interaction Region

A detailed design of the IR must include the focusing scheme to obtain the desired spot sizes, a beam separation scheme, the collimation and masking scheme to protect components from synchrotron radiation, local chromaticity correction if required, the interface with the detectors etc. Here we will consider only the basic optics parameters. The lower limit on β^*, which could perhaps be 1 - 3 cm, is usually determined by the maximum tolerable beam size in the interaction region (IR) quadrupoles and the chromaticity generated by these quadrupoles. Furthermore to prevent the loss of luminosity due to the hourglass effect, β^* should be significantly greater than the bunch length. A preliminary IR design [12] shows that it is possible to achieve $\beta_y^* = 1$ cm with sufficient momentum aperture. A more precise estimate of the tolerable minimum requires tracking to determine the dynamic aperture of the machine with realistic arc and IR magnets.

Here we will assume that $\beta_y^* \ll \beta_x^*$ as is true at most e^+ e rings. Consequently aperture and chromaticity limitations will first arise in the vertical plane. As stated earlier in this section we will consider fixed values of β_x^*, β_y^* at all circumferences and energies and assume that these do not pose aperture restrictions at any energy. These values will need to be reconsidered during the design of the final focusing system.

The choice of β_y^*/β_x^* needs to be closely related to the emittance coupling ratio $\kappa = \epsilon_y/\epsilon_x$. The horizontal beam-beam parameter is related to the vertical parameter as

$$\xi_x = \left[\sqrt{\frac{\kappa}{\beta_y^*/\beta_x^*}}\right] \xi_y \tag{2.22}$$

If $\kappa > \beta_y^*/\beta_x^*$, then $\xi_x > \xi_y$. In this case the beam-beam limit is reached first in the horizontal plane. Beyond this limiting current, the emittance grows linearly with current and the beam-beam parameters stay constant. In particular the vertical beam-beam parameter ξ_y never reaches its maximum value and since the luminosity is proportional to ξ_y, the maximum luminosity is not obtained. It is therefore desirable to have $\kappa \leq \beta_y^*/\beta_x^*$. In this paper we will consider the so called *optimal coupling* scenario where $\kappa = \beta_y^*/\beta_x^*$ and the beam-beam limits are attained simultaneously in both planes, $\xi_x = \xi_y$.

2.6 Summary of design strategy

The design of the ring optics depends on a number of parameters, among these are the maximum synchrotron radiation power allowed by the facility, the maximum beam-beam parameter which is assumed, the number of IPs required to satisfy the user community (and saturate the tolerable beam beam tune shift), the maximum bunch intensity limited by TMCI. In addition the minimum beta functions at the interaction point, β_x^*, β_y^*, the emittance coupling ratio $\kappa = \epsilon_y/\epsilon_x = \beta_y^*/\beta_x^*$, must be specified. The arc design is determined by the arc filling factor f_1 and ring filling factor f_2, which can be realized in a realistic design, the phase advance per cell μ_C, and the required rf voltage determined by N_{QL} - the ratio of RF bucket height (energy acceptance) to rms energy spread.

The design values for a first iteration can be produced from these requirements. For a given machine circumference C, determine the bend radius ρ and arc radius R from Equation (2.12) with assumed values of f_1, f_2. The maximum energy of the ring at this circumference can then be determined from Equation (2.5). The equilibrium emittance at this energy and required maximum bunch intensity from Equation (2.8) can be calculated and compared with the maximum bunch current allowed by I_{thresh}^{TMCI} . The cell length can be obtained from Equation (2.11). The maximum number of bunches can be obtained from Equation (2.13). The maximum quadrupole gradient tolerable B'_{max} is found from

$$\frac{B'_{max}\sigma_x}{B_0} = 1$$

where σ_x is the rms horizontal beam size in the arcs and B_0 is the bend field. The values obtained must then be checked for internal consistancy and collider performance.

3 Lifetime

The radiative Bhabha scattering process $e^+e^- \rightarrow e^+e^-\gamma$ is expected to dominate the beam lifetime at collision in this large lepton collider. The lifetime from this process with a scattering cross-section $\sigma_{e^+e^-}$ is

$$\tau_L = \frac{1}{N_{IP}}\frac{M_b N_b}{\mathcal{L}\sigma_{e^+e^-}} \tag{3.1}$$

Substituting for the luminosity from Equation (2.4) we can write this in terms of the beam-beam parameter ξ_y as

$$\tau_L = \left[\frac{2r_e}{N_{IP}}\frac{\beta_y^*}{\xi_y}\frac{1}{\sigma_{e^+e^-}}\right]\frac{1}{\gamma f_{rev}} \tag{3.2}$$

The cross-section $\sigma_{e^+e^-}$ has a weak logarithmic dependence on energy (see Equation (A.25) in Apendix A) which can be ignored to first order. Assuming that β_y^*, ξ_y are constant, the terms in square brackets above can be considered nearly constant. At a fixed circumference, the luminosity lifetime decreases with approximately the first power of the energy.

There are other contributions to the beam lifetime such as beam-gas scattering and Compton scattering off thermal photons but those lifetimes are about an order of magnitude larger than the luminosity lifetime considered above. For present purposes those effects can be ignored but need to be considered at a later stage.

4 Scaling of the beam-beam parameter

Although a value of the beam-beam tune shift of $\xi_x \sim \xi_y \sim$ 0.03 - 0.06 has described the operation of almost all lepton colliders over the past 20 years, recent results at LEP have shown that large colliders at high energies behave somewhat differently. The LEP machine operated quite reliably at tune shifts around $\xi_x \sim \xi_y \sim$ 0.09,[4] and, in fact, was limited by the transverse mode coupling instability rather than the beam beam tune shift, which was estimated to be in the range of 0.14[11]. Since the machine described here is even larger and higher energy than LEP, we consider how the LEP tune shifts can be extrapolated, and ultimately consider a maximum tune shift in the range of 0.17 for normal operation at the highest energies.

The damping time τ_s determines the time it takes for the beam to reach an equilibrium distribution in the absence of external nonlinear forces. As the damping increases and this time decreases, the beam becomes more immune to non-resonant perturbations that would change this equilibrium distribution. Indeed observations at several e^+ e colliders have shown that the limiting value of the beam-beam parameter increases slowly with energy or more precisely with the damping decrement. The damping decrement for beam-beam collisions is defined as the inverse of the number of beam-beam collisions per damping period,

$$\lambda_d = \frac{1}{N_{IP}\tau_s} \tag{4.1}$$

where τ_s is the damping time measured in turns. For example at LEP, the beam-beam limit has increased by more than 50% as the energy was increased from 45.6GeV to nearly 100GeV. Fitting a power law to the LEP data [4] for the maximum beam-beam tune shifts at three different energies we find that

$$\xi_{y,max} \sim \lambda_d^{0.26} \tag{4.2}$$

Earlier Keil and Talman [13] and more recently Peggs [10] considered the scaling of the beam-beam tune shift with λ_d applied to data from earlier machines such as SPEAR, PETRA, CESR and found roughly the same power law behaviour. Figure 1 shows this power law curve and also the expected beam-beam tune shifts for VLLC33 and VLLC34. The damping decrement for VLLC33 at 185 GeV is 0.01 which implies $\xi_{y,max} = 0.1$ while for VLLC34 where the maximum energy is lower, $\lambda_d = 0.0006$ and the expected $\xi_{y,max} = 0.05$. Uncertainties in the data and the fitting of this data to a power law may in fact allow higher values in the range $0.1 \leq \xi_{y,max} \leq 0.14$ at 185 GeV [11].

5 Polarization

In a storage ring electrons become vertically polarized via the emission of synchrotron radiation. In a perfect ring - planar and without errors - this polarization would build up to a maximum value of 92.4%. In a real ring - nonplanar, misalignments and field errors - the maximum achievable polarization can be significantly less. The emission of photons with

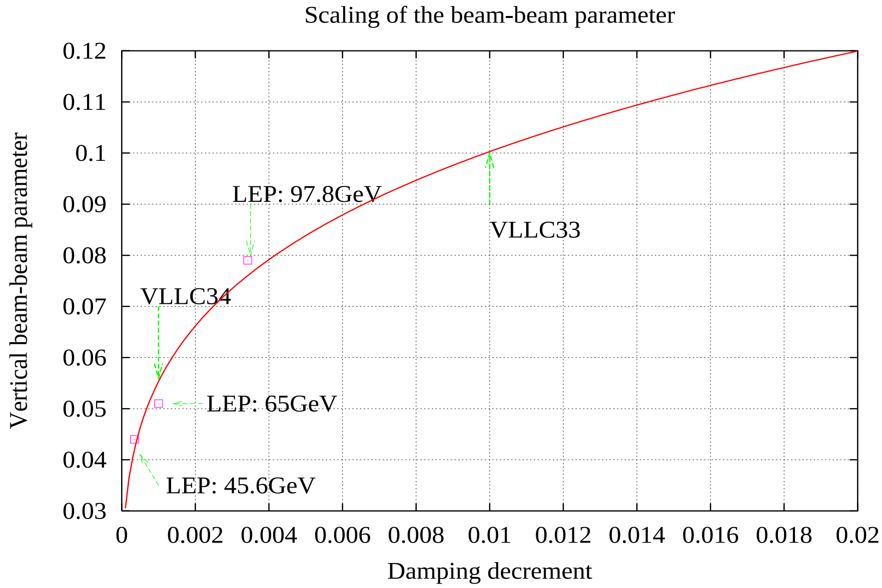

Figure 1: The LEP data on the maximum beam-beam tune shift is fit to a power law curve. Also shown are the damping decrements and expected maximum beam-beam parameter for the VLLC33 (luminosity=10^{33}cm ^{2}sec ^{1}) and VLLC34 (luminosity=10^{34} cm ^{2}sec ^{1}) design parameters.

a very small probability of spin flip while leading to polarization also leads to depolarization in the presence of imperfections. The stochastic changes in electron energy after photon emission and coupling to the orbit motion lead to spin diffusion and loss of polarization. In the presence of depolarizing effects, the maximum value of the polarization along the equilibrium spin direction $\hat{n}$ is given by the expression due to Derbenev and Kondratenko

$$P_\infty = \frac{8}{5\sqrt{3}} \frac{\oint ds \langle \frac{1}{|\rho(s)|^3} \hat{y} \cdot (\hat{n} \quad \partial\hat{n}/\partial\delta) \rangle_s}{\oint ds \langle \frac{1}{|\rho(s)|^3} [1 \quad \frac{2}{9}(\hat{n}\cdot\hat{s})^2 + \frac{11}{18}(\partial\hat{n}/\partial\delta)^2] \rangle_s} \tag{5.1}$$

where $\delta = \Delta p/p$ and $\langle\rangle_s$ denotes the average over phase space at a location s. We note that $\hat{n}$ is a vector field which changes with location in phase space. The polarization rate is approximately [14]

$$\frac{1}{\tau} = \frac{1}{\tau_{ST}} + \frac{1}{\tau_{Dep}} \tag{5.2}$$

$$\frac{1}{\tau_{ST}} = \frac{8}{5\sqrt{3}} \frac{e^2\gamma^5\hbar}{m_e^2c^2} \frac{1}{C} \oint ds \langle \frac{1}{|\rho(s)|^3} [1 \quad \frac{2}{9}(\hat{n_0}\cdot\hat{s})^2] \rangle_s \tag{5.3}$$

$$\frac{1}{\tau_{Dep}} = \frac{8}{5\sqrt{3}} \frac{e^2\gamma^5\hbar}{m_e^2c^2} \frac{1}{C} \oint ds \langle \frac{1}{|\rho(s)|^3} \frac{11}{18} (\partial\hat{n}/\partial\delta)^2 \rangle_s \tag{5.4}$$

When $\hat{n_0}$ is nearly vertical, then $\hat{n_0}\cdot\hat{s}$ is small compared to unity and assuming that the bend radius is everywhere the same, the Sokolov-Ternov polarization rate reduces to the simplified expression

$$\frac{1}{\tau_{ST}} \approx \frac{8}{5\sqrt{3}} \frac{e^2\hbar}{m_e^2c^2} \frac{\gamma^5}{\rho^3} \tag{5.5}$$

The time to build up to the asymptotic polarization falls sharply with increasing energy but increases as the cube of the bend radius. The energy ratio between this collider and LEP is between two to three while the radius is nearly an order of magnitude larger than LEP. Consequently the polarization build up time in this machine will be a few hours compared to approximately 6 minutes at 100 GeV in LEP. Polarization may still be a practical possibility but that is primarily determined by the value of the achievable asymptotic polarization.

The key to calculating the asymptotic polarization P_∞ in a real machine lies in the calculation of the spin-orbit coupling vector $\partial\hat{n}/\partial\delta$. This depends on the detailed lattice configuration and there are several sophisticated programs which do this [14, 15].

Observations at several $e^+ \quad e$ rings have shown that the maximum polarization drops with energy. For electrons, integer resonances are spaced 0.44 GeV apart so the larger energy spread at higher energies leads to a larger portion of the resonance to be spanned by the beam distribution. However prediction of the drop in polarization with energy is complicated and there does not exist a simple analytical way to extract the energy dependence of $\hat{n}$ in general. If however we assume that both orbital and spin motion is approximately linear, then examination of the spin-orbit coupling matrices (the **G** matrices in [14]) shows that $\partial\hat{n}/\partial\delta \propto \gamma^2$. Using Equation (5.1) this implies [16] that the asymptotic polarization scales as

$$P_\infty = \frac{8}{5\sqrt{3}}\frac{1}{1+\beta E^4} \tag{5.6}$$

Here β is a parameter which does not depend on energy. Experience has shown that this is relation is nearly true if the motion is linear and the closed orbit is well corrected. This scaling law will be violated if either the orbital motion or the spin motion is strongly nonlinear. Observations at LEP show a sharp fall off in polarization above 45 GeV and polarization at the level of a few % at 60 GeV. This would predict that there will be no usable polarization at the energies of interest in this very large ring.

It may however be possible to increase the polarization by a combination of methods, as used for example in HERA [17]. These include:

- Tight alignment tolerances on all magnets, specially in the vertical plane.
- Extremely good correction of the vertical closed orbit distortions and the vertical dispersion.
- Careful selection of the tunes, e.g. the energy should be chosen so that the fractional part of the spin tune (approximately equal to $a\gamma$) is close to 0.5. At energies near 185 GeV, this would specify an energy of 184.84 GeV. The tunes in all planes should be chosen so that the resonance conditions

  $$\nu = k + m_x\nu_x + m_y\nu_y + m_s\nu_s$$

  are far from satisfied especially for 1st order resonances $|m_x| + |m_y| + |m_s| = 1$ and low order synchrotron sideband resonances of 1st order betatron resonances $|m_x| + |m_y| = 1$.
- Harmonic spin matching and minimizing the spin orbit coupling will be essential. A sequence of vertical orbit correctors and dispersion correctors is used to generate harmonics which compensate the integer and linear spin resonances driven by the imperfection fields. These correction methods can be facilitated by making each section of the ring locally "spin transparent" which would place constraints on the phase advances and other Twiss functions in these sections.

It is clear that if polarization is desired, the lattice must be designed from the outset to achieve this. Further studies are required however to examine whether, even with the use of the methods outlined above, respectable levels of polarization will be achievable at the energies of interest.

6 Design Parameters at High Energy

The design strategy has been outlined in Section 2. We know for example that at fixed luminosity, synchrotron radiation power and beam-beam parameter that the maximum energy of the beams scales with the cube root of the circumference. Here we apply this strategy to different machines with circumferences in the range from 200 km to 300 km. This should span the range envisoned for different versions of the VLHC.

One feature of the design that needs some iteration is the initial choice of the beam-beam parameter. We have seen in Section 4 that the maximum beam-beam parameter scales with some power of the energy. Since the beam energy is an output parameter, we need to ensure that the choice of the beam-beam parameter is self-consistent with the design energy.

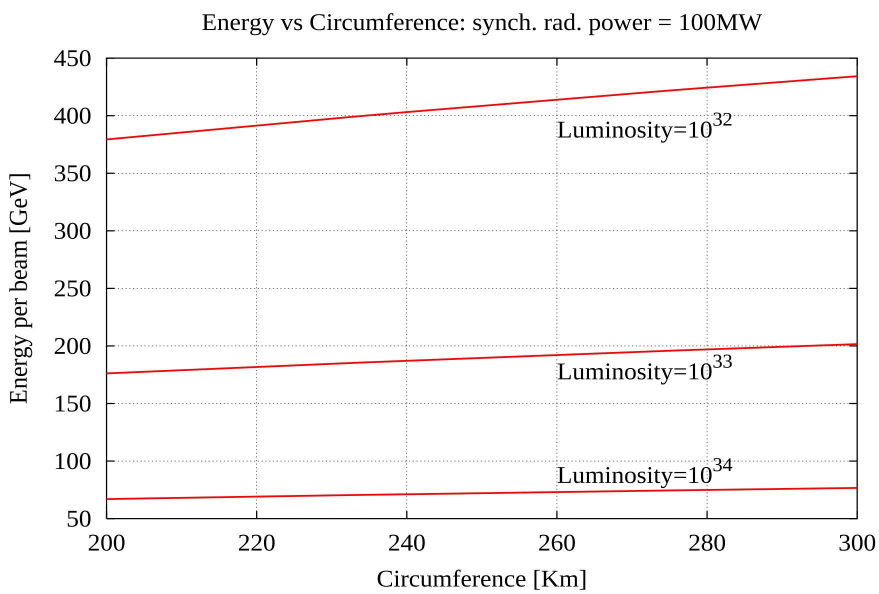

Figure 2: The maximum energy attainable as a function of the machine circumference for three different luminosities. At the energies obtainable with luminosities of 10^{33} cm ^{2}sec ^{1} and lower, the maximum beam-beam parameter was set to 0.1. At the luminosity of 10^{34} cm ^{2}sec ^{1}, the beam-beam parameter was set 0.05. The synchrotron radiation power of both beams was set to 100MW in all cases.

Figure 2 shows the maximum energy as a function of the circumference for three different luminosities. For example at a circumference of 233 km, the maximum single beam energies at luminosities of 10^{32}, 10^{33}, 10^{34} cm ^{2}sec ^{1} are 396, 185 and 70 GeV respectively. Thus a ring with circumference around 233 km should suffice to reach the top quark production threshold, estimated to be at 360GeV, with a luminosity close to 10^{33} cm ^{2}sec ^{1}. One also observes that single beam energies from 300-500 GeV appear attainable at a luminosity of 10^{32}cm ^{2}sec ^{1}. However the RF voltages required in this range of energies is in the hundreds of GV as seen in Figure 3. In the range of 150-250 GeV per beam and luminosity 10^{33} cm^{-2}sec^{-1}, the RF voltages are a few GV, comparable to LEP.

Figure 4 shows the $e^{-}-e^{+}$ bremmstrahlung lifetime as a function of circumference at three luminosities. We observe that at a luminosity of 10^{33} cm^{-2}sec^{-1}, this lifetime ranges from 15-36 hours which should be adequate considering that this is the dominant contribution to the beam lifetime at luminosity. The lifetime was calculated using the expression (A.25) for the bremmstrahlung cross-section which does not have corrections from a cut-off parameter which corresponds to the characteristic distance between particles in the bunches. With this cut-off the cross-sections are typically 30% lower. For example analysis of the cross-section at LEP energies [31] showed that the uncorrected cross-section of 0.3 barns was reduced to 0.2 barns. This number was found to agree well with measurements. As a consequence of the smaller cross-section, luminosity lifetimes may be about 30% higher than shown in Figure 4. At most energies, the lifetime is typically in the tens of hours and increases to hundreds of hours when the energy drops to less than 100 GeV as is the case when the required luminosity is 10^{34} cm^{-2}sec^{-1}. By comparison, the luminosity lifetime at LEP is about 5-6 hours.

Table 1 shows the design parameters of a 233 km ring obtained by following the design strategy outlined in Section 2. We remark on some of the interesting features of this ring compared to LEP.

- Increasing the circumference of LEP by a factor of 8.5 and the total synchrotron radiation power by about 7 allows a 10 fold increase in luminosity at almost double the energy.
- The bunch current in VLLC33 is roughly 7 times lower in keeping with the expected lower threshold for TMCI.
- The $e^{+}-e^{-}$ bremmstrahlung lifetime in VLLC33 is significantly longer at 23 hours.
- The vertical beam sizes in the two machines are comparable
- The horizontal beams sizes in the arcs of the two machines are also close. Hence vacuum chamber dimensions in VLLC33 can be similar to those in LEP.
- The main dipole field is about 5 times weaker than that of LEP. Iron magnets operated at room temperature will suffice. Conversely, good shielding from stray magnetic fields, e.g. those of the low field hadron collider, will be critical.
- The critical energy is smaller in VLLC33 so shielding against synchotron radiation as in LEP should be adequate for VLLC33. The photon flux per unit length is almost the same in the two machines.
- The RF voltage required for VLLC33 is significantly higher at 4.7GV (without beam loading) compared to 3.1GV (presumably with beam loading) for LEP.
- We assumed $f_1 = f_2 = 0.84$ to have the same ratio of bend radius ρ to the machine radius $C/(2\pi)$ as in LEP. A somewhat more aggressive choice of packing fractions $f_1 = f_2 = 0.90$ or $2\pi\rho/C = 0.81$ yields slightly different parameters, e.g. maximum energy $E_{max} = 193$ GeV, RF voltage $V_{RF} = 4883$ MV. Both of these quantities scale with the third root of the bend radius.
- We chose optimum coupling, i.e. $\epsilon_y/\epsilon_x = \beta_y^*/\beta_x^*$ which implies that $\xi_x = \xi_y$. Operating at the beam-beam limit in both planes might well be challenging. If we reduce the emittance coupling to half this value, $\epsilon_y/\epsilon_x = 0.025$, then $\xi_x = 0.071$ while staying at the beam-beam limit in the vertical plane $\xi_y = 0.1$. With this choice, optics and

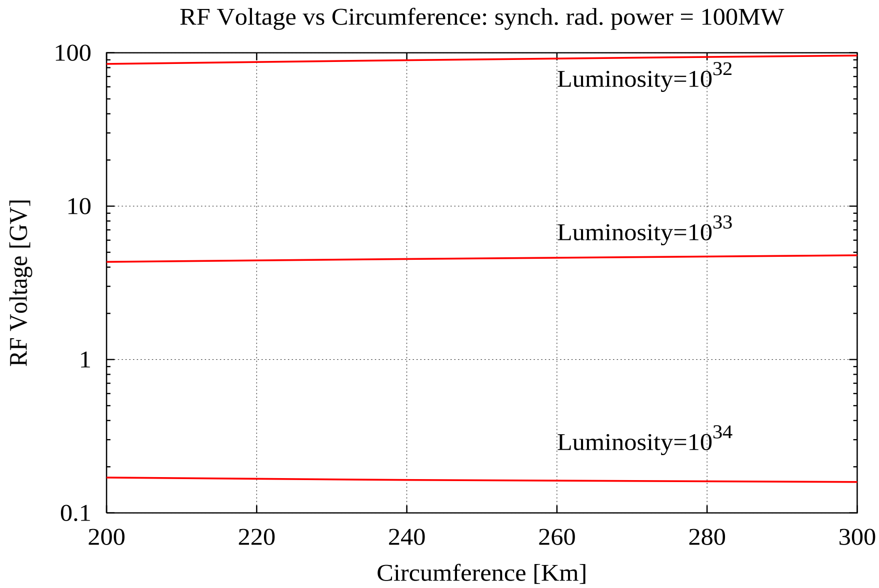

Figure 3: RF voltage required when operating at the maximum energy as a function of the machine circumference for different luminosities with the synchrotron radiation power of both beams set to 100MW in all cases.

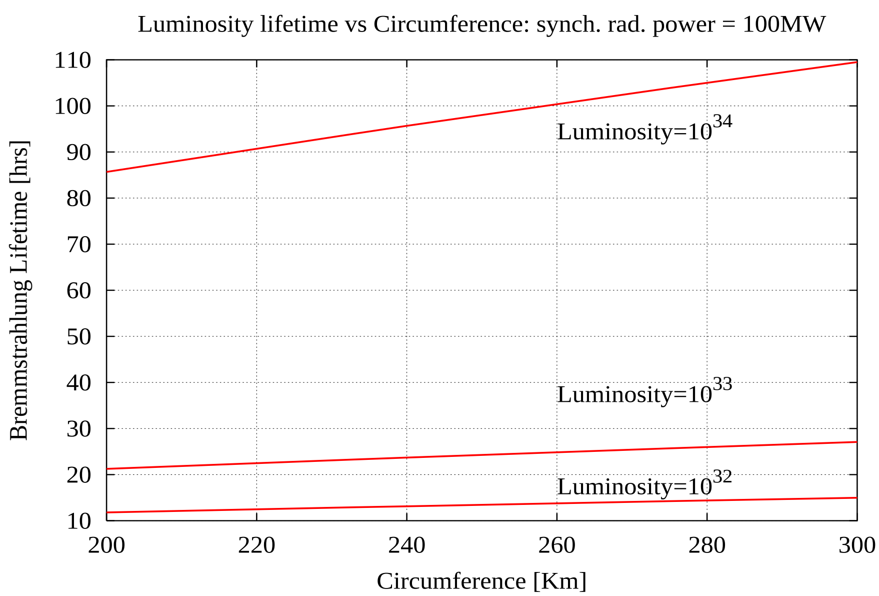

Figure 4: Luminosity lifetime vs the circumference at three different luminosities. Here the lifetime *increases* with the required luminosity because the maximum energy decreases at higher luminosities and the lifetime $\sim 1/E$, cf. Equation(3.2). See the text for other remarks.

e^{+} e **Collider Parameters**

Parameter	LEP 1999	VLLC33
Circumference [m]	26658.9	233000.
β_x^*, β_y^* [cm]	150, 5	100, 5
$\kappa/(\beta_y^*/\beta_x^*)$	0.31	1.0
Luminosity [cm ^{2}sec ^{1}]	9.73×10^{31}	1×10^{33}
Maximum Energy [GeV]	97.8	185.3
Emittances ϵ_x, ϵ_y [nm]	21.1, 0.220	6.06, 0.30
RMS Beam size at IP σ_x^*, σ_y^* [μm]	178., 3.30	77.52, 3.88
Bunch intensity/current [/mA]	4.01×10^{11}/0.720	4.85×10^{11}/0.10
Number of bunches per beam	4	126
Bunch spacing [km]	6.66	1.85
Total beam current (both beams) [mA]	5.76	25.20
Beam-beam tune shift ξ_x, ξ_y	0.043, 0.079	0.1, 0.1
e^+e bremmstrahlung lifetime [hrs]	6.0	23.6
Dipole field [T]	0.110	0.0238
Bend Radius [m]	3026.42	25968.1
Phase advance per cell μ_x, μ_y [degrees]	102, 90	90.0
Arc tune	70.3, 62.0	215
Cell Length [m]	79.110	226.345
Total length of dipoles in a cell [m]	69	189.41
Quadrupole gradient [T/m]	9.50	15.59
Length of a quadrupole [m]	1.60	0.494
Arc β^{max}, β^{min} [m]	144, 18	386, 66
Arc $\sigma_x^{max}, \sigma_x^{min}$ [mm]	1.70, 0.60	1.52, 0.63
Arc dispersionD^{max}, D^{min} [m]	1.03, 0.450	1.12, 0.53
Bend radius to Machine radius $2\pi\rho/C$	0.710	0.70
Momentum compaction	$1.60\times10^{\ 4}$	$2.23\times10^{\ 5}$
Polarization time [hrs]	0.1	2.2
Energy loss per particle per turn [GeV]	2.67	4.0
Critical energy [keV]	686.	452.61
Longitudinal damping time [turns]	73.0	46.3
RMS relative energy spread	$1.52\times10^{\ 3}$	$9.83\times10^{\ 4}$
Bunch length [mm]	11.0	7.06
Synchrotron tune	0.116	0.115
RF Voltage [MV]	3050.00	4572.5
RF frequency [MHz]	352.209	400.
Revolution frequency [kHz]	11.245	1.287
Synchrotron radiation power - both beams [MW]	14.5	100.7
Available RF power [MW]	34.1	
Power load from both beams [kW/m]	0.820	0.517
Photon flux/length from both beams [/m/sec]	2.40×10^{16}	1.15×10^{16}

Table 1: Parameters of the very large lepton collider with a desired luminosity of 10^{33} cm ^{2}sec ^{1} and a circumference of 233km.

beam size parameters change, e.g. $\epsilon_x = 11.8$ nm, cell length=278 m, $\beta^{max} = 475$ m, $D_x^{max} = 1.72$ m, $\sigma_x^{max} = 2.4$ mm, $\nu_s = 0.156$, $\sigma_l = 8.1$ mm. The RF voltage increases to 4780 MV while most other parameters are relatively unaffected.

- We chose an energy acceptance that is ten times the equilibrium energy spread of the beam to ensure sufficient quantum lifetime. At LEP with the parameters given in Table 1, this ratio is only about 6.6. If we assume this value for the 233 km ring, the RF voltage is lowered from 4.57 GV to 4.43 GV. The energy loss per turn requires that the RF voltage be greater than 4 GV.

7 Operation at 45 GeV

There is considerable interest in precision measurements at the W and Z^0 mass range, $E_{CM} \sim 90$ GeV. Here we consider the feasibility of using this large collider to attain high luminosities - in excess of 5×10^{33} cm ^{2}sec ^{1}. These are the so-called "gigaZ" measurements which required integrated luminosities around 500 inverse picobarns. Polarized beams at this energy will greatly add to the physics program allowing for example measurements of the left right asymmetry or the Weinberg angle.

The design principles for obtaining high luminosity at low energies are different from those at high energy. At low energies, the synchrotron radiation power is low and does not impose any constraints. Only the beam-beam tuneshift limit needs to be respected. This constrains the bunch intensity per unit transverse area or N_e/ϵ. Under these conditions, the luminosity is

$$\begin{aligned} \mathcal{L} &= \frac{\pi}{r_e^2} M_B f_{rev} [\frac{\sigma_x^* \sigma_y^*}{(\beta_y^*)^2}] \gamma^2 \xi_y^2 &\quad (7.1) \\ &= \frac{\pi}{r_e^2} M_B f_{rev} [\frac{\kappa \beta_x^*}{(\beta_y^*)^3}]^{1/2} \gamma^2 \xi_y^2 \ \epsilon_x &\quad (7.2) \end{aligned}$$

In this regime the luminosity increases with the emittance $\mathcal{L} \propto \epsilon_x$ so this requires that the aperture be filled to maximize the luminosity. Leaving enough room for good quantum lifetime, the maximum permissible emittance could be determined by a condition such as

$$A_{req} \equiv 10 * [\sigma_x^2 + (D_x \delta_p)^2]^{1/2} + \text{c.o.d} \leq r_{pipe} \tag{7.3}$$

where c.o.d is the expected closed orbit distortion and r_{pipe} is the radius of the beam pipe. The emittance can be increased by lowering the phase advance per cell. The bunch intensity is found from the beam-beam tune shift

$$N_b = (\frac{2\pi}{r_e} \sqrt{\frac{\kappa}{\beta_y^*/\beta_x^*}}) \gamma \epsilon_x \ \xi_y \tag{7.4}$$

If this intensity exceeds the TMCI threshold N_b^{TMCI}, the emittance can be lowered by increasing the phase advance.

There is no significant constraint on the beam current from the synchrotron radiation power so this does not limit the number of bunches. Instead the number of bunches is limited by the minimum bunch spacing allowed. This spacing S_b^{min} could be limited by multi-bunch instabilities. Assuming a uniform bunch distribution around the ring, the number of bunches is determined by

$$M_B f_{rev} = \frac{c}{S_b^{min}} \tag{7.5}$$

We will assume $S_b^{min} = 5$ m, somewhat arbitrarily. It remains to be checked that this short a bunch spacing is feasible with a reasonable longitudinal feedback system.

For 45 GeV operation we will use the same magnet lengths as determined by high energy operation. The cell length is also fixed although it may be attractive to double the cell length by turning off half (or perhaps two thirds of) the quadrupoles. This would allow a higher phase advance for the same emittance. We assume that the beam pipe radius is 5 cm. The parameters that are determined by high energy operation are shown in Table 2.

Circumference [km]	233.00
Revolution frequency [kHz]	1.2867
Arc radius [m]	31031.880
Bend radius [m]	25968.098
β_x^*, β_y^* [cm]	100.0, 5.0
Ratio of emittances	0.050
Number of cells	861
Bend angle in half-cell [mrad]	3.647
Length of cell [m]	226.345
Length of all dipoles in cell [m]	189.410
Quadrupole length [m]	0.494
Cell packing fraction	0.189

Table 2: Fixed parameters for 45 GeV operation. These are determined by optimizing at 185 GeV.

The minimum phase advance per cell μ^{min} is determined by the requirement $A_{req} \leq 5$ cm. We allow for a rms closed orbit distortion of 1 cm - a conservatively large value. The left figure in Figure 5 shows the emittance and A_{req} as a function of the phase advance. From this figure we determine $\mu^{min} = 25°$. The right figure in Figure 5 shows that the luminosity drops below 10^{34} cm ^{2}sec ^{1} at phase advances greater than 27°. Hence we set the phase advance per cell to the minimum value $\mu_C = \mu^{min}$. The values of other parameters follow and are shown in Table 3.

The luminosity is slightly above 10^{34} cm ^{2}sec ^{1}. This theoretical value will correspond to the peak luminosity at best. A more aggressive design will be necessary if the average luminosity is required to be 10^{34} cm ^{2}sec ^{1}. The single bunch current is low at 0.03 mA or about a third of that required at 185 GeV so the TMCI instability may not be an issue. However with the large number of bunches, the beam current is high at 1.4 A. This makes the design more akin to that of the B factories. While the RF voltage required is low at 50 MV, we assume that it will be provided by the superconducting cavities required for operation at 185 GeV. The dynamic heat load and the HOM power generated in these cavities may be substantial at these high beam currents and may therefore rule out such a large beam current. Multi-bunch instabilities may also be severe and therefore require dedicated feedback systems for low energy operation. Finally the Sokolov-Ternov polarization time is 2600 hours, thus physics with polarized beams is not an option at this energy unless one injects polarized beams into the ring.

In short, operation at 45 GeV will require several different challenges to be faced compared to operation at 185 GeV. It is not even clear if the components will be able to withstand

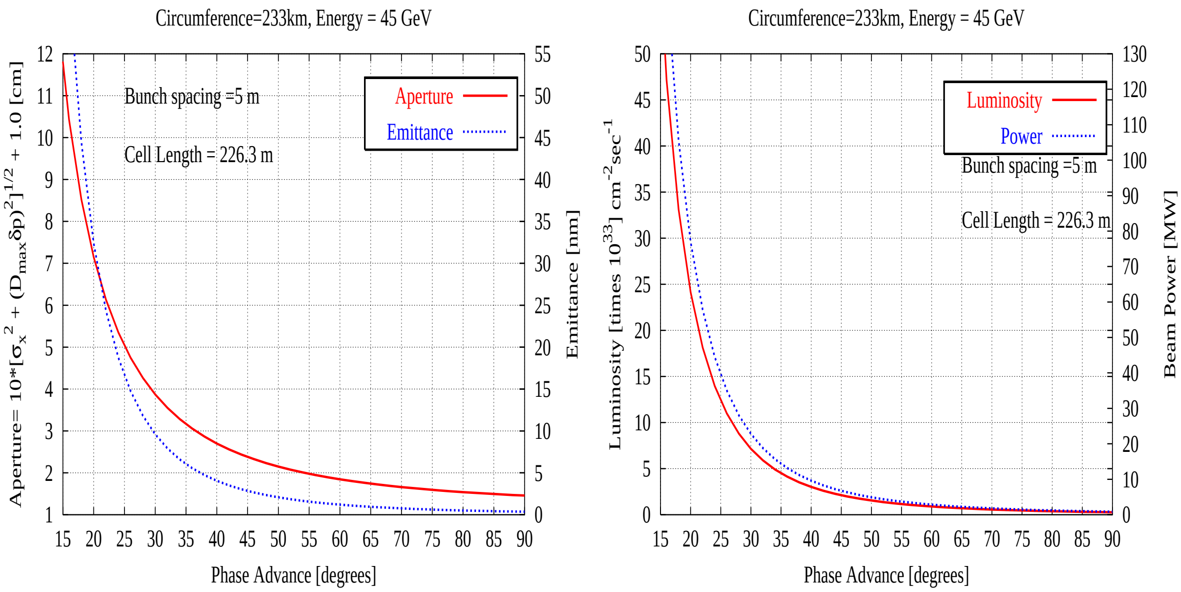

Figure 5: Left: The emittance and A_{req} as a function of the phase advance per cell. Assuming the beam pipe radius is 5 cm, this determines the phase advance to be 25°. Right: The luminosity and synchrotron radiation power as a function of the phase advance. The luminosity drops below 10^{34} cm ^{2}sec ^{1} at phase advances greater than 27°.

the high beam currents required. Therefore it makes more sense to consider a smaller ring for physics at the Z0 mass. A natural choice for this would be the injector to the large ring. Such a ring (a Z0 factory) has been proposed by E. Keil [6]. The top energy of this injector is 45 GeV with a circumference of 12.57 km chosen so that the polarization time is reasonable at about 20 minutes. Besides the physics potential of this ring, this is an attractive option for several other reasons. It raises the injection energy into the VLLC and thus may alleviate or eliminate concerns about TMCI in the large ring. Also it would allow physics to be possible while the VLLC is under construction.

Energy [GeV]	**45.00**
Luminosity	12.38×10^{33}
Synch. radiation power(both beams) [MW]	39.40
σ_x^*, σ_y^* [microns]	128.8, 6.4
Number of bunches	46600
Bunch spacing [km]	0.0050
Particles per bunch	1.47×10^{11}
Bunch current [mA]	0.0302
Emittances [nano-m]	16.59, 0.83
Beam-beam parameter	0.045
Damping decrement	0.00016
Single beam current [mA]	1408.08
Brho [Tesla-m]	150.10
Arc tune	59.8
Phase advance per cell [deg]	25.0
Dipole field [T]	0.00578
Focal length of cell [m]	261.44
Quad gradient [T/m]	1.161
Quad field at $1\sigma_x^{max}$/dipole field	0.66
Cell: β_{max}, β_{min} [m]	651.50, 419.66
Cell: $\sigma_x max, \sigma_x^{min}$ [mm]	3.29, 2.64
Cell: $\sigma_y^{max}, \sigma_y^{min}$ [mm]	0.74, 0.59
Max apertures required [cm]	5.03, 1.74
Max and min disp. [m]	9.76, 7.86
Momentum compaction	0.2376×10^{3}
Energy loss per turn [GeV]	0.014
Damping time [turns]	3216
RF Voltage [GV]	0.05
Synchronous phase [deg]	16.25
Relative energy spread	0.239×10^{3}
RF acceptance	0.240×10^{2}
Synchrotron tune	0.112
Bunch length [mm]	18.82
Longitudinal emittance [eV-sec]	0.0021
Bremm. cros-section [barns]	0.454
Bremm. lifetime [hrs]	168.9
Polarization time [hrs]	2600.8
Critical energy [keV]	6.514
Critical wavelength [A]	1.593
Number of photons/m/sec	0.314×10^{18}
Gas load [torr-L/m-sec]	0.282×10^{6}
Linear Power load(both beams) [kW/m]	0.202

Table 3: Parameters of a 45 GeV ring with the same circumference and magnets as the 185 GeV ring with parameters in Table 1.

Parameter	Energy dependence
Equilibrium emittance ϵ_x	γ^2
Energy loss U_0, RF Voltage V_{RF}	γ^4
Damping time $\tau_s \sim E/U_0$	$\gamma^{\;3}$
Maximum beam-beam parameter $\xi_y \sim \tau_s^{\;0.26}$	$\gamma^{0.8}$
Luminosity $\mathcal{L} \sim \xi_y \gamma^{\;3}$	$\gamma^{\;2.2}$
Bunch intensity $N_b \sim \xi_y \gamma \epsilon_x$	$\gamma^{3.8}$
Maximum number of bunches $M_B^{max} \sim 1/(N_b E^4)$	$\gamma^{\;7.8}$
Synchrotron frequency ν_s	$\gamma^{3/2}$
Equilibrium energy spread σ_E/E	γ
Bunch length σ_l	$\gamma^{\;1/2}$
Critical energy E_c	γ^3
Bremmstrahlung lifetime $\tau_L \sim 1/(\xi_y \gamma)$	$\gamma^{\;1.8}$

Table 4: Scaling of beam parameters with energy. Machine circumference and synchrotron radiation power are kept fixed.

8 Scaling Laws with Energy

In the previous two sections we developed parameter sets for operation at 185 GeV and 45 GeV respectively. The design philosophies at these two energies were quite different. The main interest in this ring however is at the high energy end so it is important to determine the useful upper limit in energy for this machine. Thus for all energies above 100 GeV or so, the design philosophy outlined in Section 2 is relevant.

We assume that magnet lengths, phase advances are chosen at some energy of interest and thereafter kept fixed. Table 4 shows the scaling with energy of some of the important parameters. Most of these dependences on energy are well known. For example the equilibrium emittance increases as γ^2 and the RF voltage increases as γ^4. The additional twist here is that the beam-beam parameter is allowed to scale with energy and recent data (see Section 4) suggest that in a given machine $\xi_y^{max} \sim \gamma^{0.8}$. If we are to operate at the beam-beam limit at all energies, then (a) the luminosity drops more slowly with energy $\mathcal{L} \sim \gamma^{\;2.2}$ compared to $\gamma^{\;3}$ without the scaling of the beam-beam parameter and (b) the bunch intensity increases more rapidly as $N_b \sim \gamma^{3.8}$ rather than γ^3. The e^+ e bremmstrahlung lifetime also drops faster with energy as $\tau_L \sim \gamma^{\;1.8}$ in this scenario.

Figure 6 shows the values of luminosity and RF voltage as a function of energy with a ring circumference of 233 km and synchotron radiation power kept constant at 100 MW. As mentioned above ξ is allowed to scale with energy and the values at some of the energies are shown in the figure. On this plot we show the luminosity and RF voltage at 45 GeV as a single data point while the values above 100 GeV are obtained using the high energy design strategy. We observe that if a maximum of 15 GV of RF is available, the energy reach of a single beam in this ring extends from 100 GeV to 250 GeV with luminosities in the range from 0.5-4$\times 10^{33}$ cm $^{\;2}$sec $^{\;1}$.

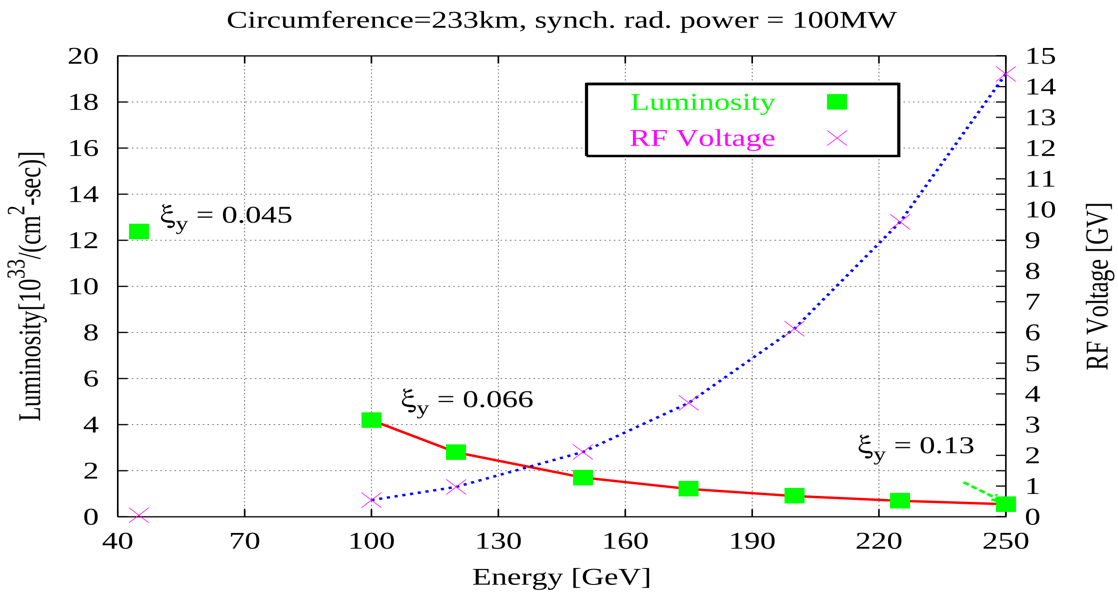

Figure 6: Achievable luminosities and the RF voltages required as a function of energy at a ring circumference of 233km. The synchotron radiation power is kept constant at 100MW for energies at and above 100 GeV. The beam-beam parameter scales with the damping decrement as discussed in Section 4. The values at 45 GeV are obtained using the design strategy discussed in Section 7.

9 An Injector System

The Fermilab accelerator complex (Linac, Booster and Main Injector) could be used as the basis for an e$^+$e injector if the beam energies were somewhat reduced from those used for protons. The specifications of of an injector system could follow the design of the LEP[21] and HERA[25] injectors, or the the APS[26] injection system.

Two new electron linacs would be required. The first would operate at about 3 GHz and accelerate electrons to an energy of around 200 MeV, which would be sufficient to produce positrons. A positron production target would be followed by a second linac section to produce a positron energy high enough to inject into the positron damping ring. Since the positrons will be produced at a much lower flux and larger emittance than electrons, it is necessary to damp and collect positrons from many pulses before further acceleration. The CERN, HERA and APS damping rings are very compact, and operate at energies of around 400 600 MeV. The operation of these systems in the same enclosure, parallel to the Fermilab proton linac, seems possible, During the checkout of the FNAL 805 MHz linac upgrade, the linac tunnel was operated essentially with two parallel linacs, so the addition of a e$^+$e linac line would not crowd the existing facility[27].

We have considered the use of the FNAL Booster to accelerate the e$^+$ and e to higher energies, however the use of gradient magnets in the lattice makes this ring somewhat inappropriate for electrons, since this lattice affects the damping partition numbers in undesirable ways. In order to eliminate this problem, a correction package, consisting of a gradient magnet and a quadrupole, should be inserted in the ring to correct the damping partition numbers. The booster has sufficient space to accommodate this package. Similar packages have been used in the PS at CERN.

It is unclear if it is more efficient to reverse the magnetic field in the accelerator structures or build injection lines so beams could circulate in opposite directions. We assume the fields will not be reversed and injection and extraction systems would have to be added to the booster for e^+e^- operation. The maximum energy that could be reached with the existing rf would be around 3 GeV. Since a new proton source is being considered for a neutrino source and muon collider, which would not fit in the existing booster tunnel, there is also the possibility of designing a compact, separated function magnet lattice to replace the existing booster magnets.

We assume electrons and positrons would be injected into the Main Injector (MI) in opposite directions at an energy of around 3 GeV. This energy would require the MI magnets to operate at a much lower field than would ever be used for protons, however the magnets have been measured at this low field and the field quality seems to be acceptable for electron operation[28]. The maximum energy that could be produced in the main injector is around 12 GeV, due to the limited rf, and the limited space for adding more. The beams would then be extracted in opposite directions into the VLHC booster tunnel for acceleration up to the injection energy of the VLHC ring.

A third synchrotron is probably required, since the 12 GeV electrons from the MI injected into the collider ring, would require the average magnetic field to be about 16 Gauss, which should be compared to the 215 Gauss injection field of LEP. We have studied the properties of an electron ring in the tunnel of a low field VLHC booster in the context of an ep collider[29]. Such a ring could have a maximum energy up to about 80 GeV with a installed RF voltage of 1.09 GV. We assume this rf operates at 352 MHz. If the VLHC booster ring was used only as an injector, an injection energy of around 40 GeV could be accommodated with an rf voltage of about 60 MV.

A recent suggestion by E. Keil[11] of building an injector with a beam energy of 45 GeV has a number of desirable results. A higher energy injector makes injection into the high energy ring easier, and raises the transverse mode coupling instability threshold, permitting more intense bunches. In addition the injector is at an energy where it could be carefully optimized for operation as a "Giga Z" Factory, with many tightly spaced bunches circulating in a comparatively small ring. This permits staging, in that the injector can be producing useful physics while the large ring is under construction. When the facility is complete, there would be the opportunity of using the injector for Z^0 physics while the high ring is used for Higgs, SUSY and top quark physics.

10 Technological Challenges

The primary technical challanges seem to be cooling the vacuum chamber, disposing of the heat produced, and determining how low the field of the collider magnets can be confidently run, since this minimum field determines the design of the magnets and the injection energy. In addition, however, there are a number of other technical problems which must be considered.

10.1 Vacuum System

Besides the usual synchrotron radiation induced gas desorption, the vacuum chamber design is determined by a number of constraints. Although the power density of the synchrotron radiation deposition is smaller than many other storage rings and synchrotron sources, the critical energy of the synchrotron photons spans a large range, (5 - 500 keV), and the large bend radius complicates the power deposition. In addition the large circumference requires a design which both minimizes beam wall interactions and is inexpensive.

The large range in critical energy of the synchrotron radiation implies that the power in *low* energy beams will be deposited mostly inside the vacuum chamber, but the chamber will become transparent to *high* energy photons, so external absorbers are required for high energies. The high energy photons will also be subject to internal reflection at grazing incedence, but are poorly attenuated by aluminum. These photons are a radiation hazard to electronics and cable insulation, thus the absorbers must be shielded to insure useful radiation levels in the tunnel.

The large bending radius complicates even deposition of synchrotron radiation power on the vacuum chamber walls, since these chambers would be expected to move slightly with operational temperature fluctuations and the motion of the earth. Since depostion on the wall is not expected to be constant, we assume that the vacuum chamber would have an ante-chamber which would conduct the synchrotron radiation to lumped absorber / window assemblies where the power could be absorbed and the synchrotron radiation outgassing could be pumped.

In order to minimize both beam-wall interactions and the cost and complexity of the vacuum system, it may be desirable to use prebaked chambers, and welding the aluminum vacuum sections in-situ, without a subsequent bake out[30]. This makes assembly easier, eliminates the need for bellows with a large mechanical range, reduces the rf loss factor induced by the bellows on the beam (both due to the number and complexity of bellows), and reduces the cost and complexity of the vacuum system as a whole. Since the chamber will heat up somewhat during normal operation, some bellows are required. It is, however, highly desirable to avoid the expansion involved in a high temperature bake, ($\Delta l = \alpha l \Delta T = 2.4 \cdot 10^{\ 5}\ 100\ 100 = 24$ cm), for lengths l and ΔT of 100 m and 100 deg C. In order to do this, one must have sufficient pumping in the chamber to insure that a pressure of $10^{\ 8}$ Torr can be achieved, which would allow a beam lifetime of about an hour, and permit subsequent wall scrubbing by synchrotron radiation.

10.2 Cooling System

The warm water produced in the synchrotron absorbers is also a concern. Since there will be roughly 100 MW of heating, distributed over 230 km, we assume this heat must be brought to the surface where cooling towers would be used to discharge it into the atmosphere. This system would be a significant environmental perturbation on the surface. We have also looked at discharging the heat into the ground and into surface water. Since the tolerable thermal range of the system is fairly narrow, due to the fact that thermal expansion must be minimized, the temperature range of the water would also be comparatively limited, thus it would be difficult to recover any useful power from the waste water.

10.3 Magnet Design

The primary issue with the injector system design is determining the minimum field where the ring magnets can usefully transport beam. Since the bending magnets in the arcs operate at a field of B_{inj}[Gauss] = 1.3 E[GeV], and the error fields at injection should be below $(10^{\ 4} \quad 10^{\ 3)} B_{inj}$, error fields due external sources, other components and remanent

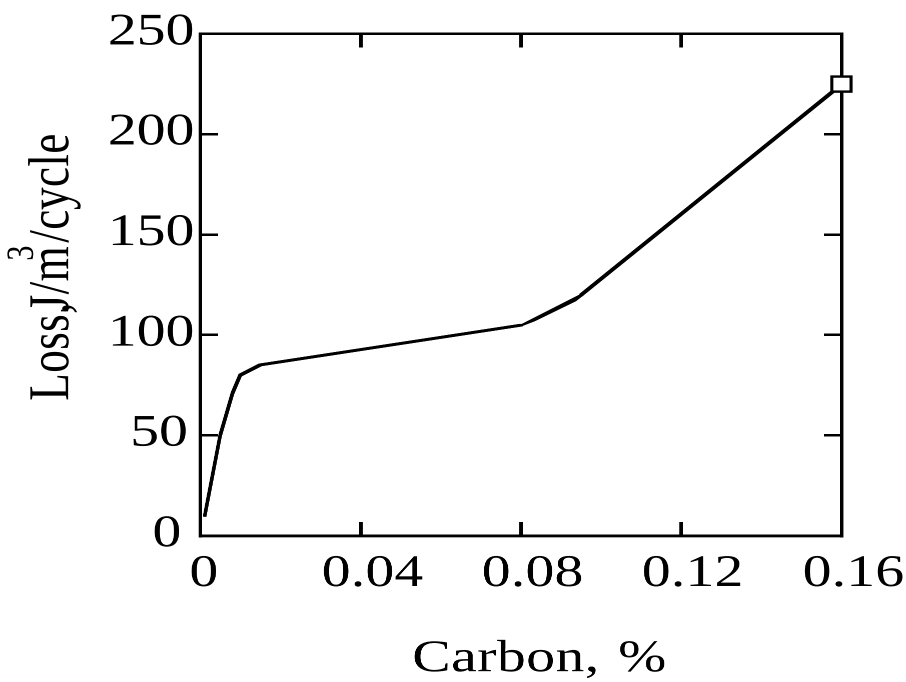

Figure 7: Hysteresis loss as a function of carbon content in steel.

fields, could be a problem. A final injector synchrotron must then be designed which can produce beams in the required energy. This synchrotron can be located in the tunnels which would be eventually occupied by the hadron booster.

We have shown that external fields can be well attenuated by the magnet yoke itself and extensive shielding of magnets may not be required[5] [22]. The remanent fields at low excitation are a function of the specific alloy used, and number of alloys exist with very low remanent fields, however their costs tend to to be higher than steel. One option seems to be the use of vacuum or hydrogen annealed steel [23]. This anneal removes carbon from the steel very efficiently, reducing the remanent field and hysteresis loses by a significant factor, as shown in Figure 5 [24]. It seems as though an order of magnatude reduction in remanent fields from the standard low carbon 1010 alloy, ($\sim$ 0.1% carbon), may be possible, in an alloy which is not significantly more expensive than standard commercially produced ones.

10.4 Other Components

A number of other systems and design issues have not been considered in any significant detail in this paper. We assume that superconducting RF cavities will be necessary. The design of these cavities must suppress higher order modes efficiently.

It is not clear if the e^+ e collider arcs would be optimized with one or two rings. While it is possible to assume that pretzel orbits can produced in the comparatively long arcs, it is not clear if parasitic collisions will produce significant emittance growth to justify the construction of a second set of arc magnets. This may significantly affect the cost.

The placement of the rf cavities will determine the energy of the beam around the ring. Since so much energy is added per turn, it may be necessary to distribute the cavities around the ring. This might require zero dispersion straights at a number of locations.

If the $e^+ \quad e$ collider and the low field hadron collider magnets are both energized at the same time, the lepton collider will need to be protected from the fringe fields of the hadron collider. These fringe fields at a distance of about a meter are of the order of a few hundred Gauss, about the same level as the main bending field in the lepton collider.

Extensive masking and collimation systems will be required to protect the detector components from synchrotron radiation.

11 Conclusions

We have explored the feasibility of a large electron-positron collider within the context of a staged approach to building a very large hadron collider. We have shown that in a ring of circumference 233 km, a lepton collider with $200 \leq E_{cm} \leq 500$ GeV with synchrotron radiation power limited to 100 MW would require RF voltages comparable to LEP and would achieve luminosities in the range 0.5 - 4 $\times 10^{33}$ cm ^{2}sec ^{1} with conservative choices of beam parameters. The achievable energy extends to nearly 800 GeV (center of mass) at a lower luminosity of 10^{32}cm ^{2}sec ^{1} but an unrealistic RF voltage is required to replenish the energy lost by the beam.

Such a machine derives benefits from its size and operating energy, in that the limiting beam-beam tune shifts may be much higher than even those seen at LEP. In addition it may be possible to further optimize the operation of this machine, particularly the interaction regions, to operate with a smaller $\beta*$ than was used in LEP. A preliminary IR design [12] shows that $\beta_y^* = 1$ cm may be feasible. There are a number of issues which require more study, in particular methods of working around the limitations imposed by the transverse mode coupling instability. The polarization of the beam which can be achieved also requires better quantification, and there are a number of concepts which we were unable integrate in the design.

We believe that a lepton collider in a tunnel built to house a very large hadon collider is technically feasible. The important question to answer first is whether the physics at these energies is sufficiently interesting. Assuming that is the case, the design of such an accelerator can proceed to the next stage. The cost of the technical components in the lepton collider will likely be dominated by the superconducting RF cavities. Improvements in design and technology can be expected to reduce the cost a decade from now compared to what they are today. Several technical challenges have to be faced but none appear to be insurmountable.

Acknowledgements

We thank Ernie Malamud for initiating this study, and Alvin Tollestrup for his encouragment. We would also like to acknowledge many useful suggestions and comments by Eberhard Keil, Oswald Grobner, Ralph Assmann and Karel Cornelis of CERN, Gerry Dugan and Richard Talman of Cornell, Desmond Barber of DESY, and Lee Teng and Sushil Sharma of Argonne.

References

[1] Annual VLHC meeting, October 2000, Port Jefferson

[2] C. Hill, Workshop on an e+e- Storage Ring at the VLHC, IIT, March 9-11, 2001, Chicago, IL, http://capp.iit.edu/ capp/workshops/epem/ ee_workshop_schedule.html

[3] Workshop on an e+e- Storage Ring at the VLHC, IIT, March 9-11, 2001, Chicago, IL, http://capp.iit.edu/ capp/workshops/epem/ee_workshop.html

[4] D. Brandt et al., *Accelerator Physics at LEP*, Reports on Progress in Physics, **63**, 939 (2000)

[5] J. Norem, E. Keil, *A High Energy* $e^+ \quad e$ *collider in a "Really Large" Tunnel*, ANL-HEP-CP-96-94, 1996

[6] E. Keil, Workshop on an e+e- Ring at VLHC, Illinois Insitute of Technology, March 2001

[7] G. Dugan, Workshop on an e+e- Ring at VLHC, Illinois Insitute of Technology, March 2001

[8] A. Burov, et al., *Beam stability issues in very large hadron collider*, NIM Section A, Vol. 450, pg 194 (2000)

[9] J. Jowett, Proc. Fourth Workshop on LEP Performance, Chamonix, January 1994 ed. J. Poole, CERN-SL/94-06, pg 47 (1994)

[10] S. Peggs, Workshop on Synchrotron Radiation Effects in the VLHC, BNL (Sept 2000)

[11] E. Keil, CERN, personal communication, (2001)

[12] C. Johnstone, T. Sen, *Lattice Design for a Very Large Lepton Collider*, Proc. of the Workshop on an e+e- Ring at VLHC, Illinois Insitute of Technology, March 2001

[13] E. Keil, R. Talman, *Part. Acc.*. **14**,p 109 (1983)

[14] D. Barber, in *Handbook of Accelerator Physics and Engineering*, edited by A. Chao and M Tigner (World Scientific, 1999)

[15] J. Buon and J.P. Koutchouk, *Polarization of Electron and Proton Beams*, CERN Yellow Report 95-06, Vol II, pg 879 (1995)

[16] Desmond Barber, DESY, personal communication (April 2001).

[17] D. Barber et al. *High spin polarization in the HERA electron storage ring*, NIM A, **338**, 166 (1994)

[18] H. Wiedemann, Nucl. Instr. Methods, **172**, 33 (1980)

[19] M. Sands, SLAC Report SLAC-121 (1970)

[20] A. Chao, *Frontiers of Particle Beams*, Lecture Notes in Physics Vol. 296, pg 51 (1988)

[21] The LEP Injector Study Group, *LEP Design Report: Vol.I, The LEP Injector Chain* CERN-LEP/TH/83-29, 1983.

[22] J. Norem, J. Jagger, S. Sharma, E. Keil, G. W. Foster, E. Malamud, E. Chojnacki, D. Winn, *An e+e- Top Factory in a 50+t0 TeV Hadron Collider Tunnel*, Proceedings of the 1997 PAC Conference, Vancouver, 363, (1997)

[23] C. W. Chen, *Magnetism and metallurgy of Soft Magnetic Materials*, North-Holland, Amsterdam, (1977).

[24] J. R. Davis, ed., *Metals Handbook, Desk Edition, Second Edition*, The Materials Information Society, Materials Park, Oh, (1998)

[25] G. Stange, IEEE Trans. Nucl Sci. **NS-26** (1979) 4146.

[26] *Annex to 7-GeV Advanced Photon Source Conceptual Design Report*, Argonne Report ANL-87-15 Annex, (1987).

[27] R. Noble, Fermilab, personal communication, (1997)

[28] B. Brown, Fermilab, personal communication, (1997)

[29] M. Derrick, H. Friedsam, A. Gorski, S. Hanuska, J. Jagger, D. Krakauer, J. Norem, E. Rotela, S. Sharma, L. Teng, K. Thompson, T. Sen, E. Chojnacki, D. P. Barber, *An ep Collider with* E_{cm} *= 1 TeV in a VLHC Tunnel*, Proceedings fo the 1999 Particle Accelerator Conference, New York (1999) 2635

[30] O. Grobner, CERN, personal communication, (2001)

[31] R. Kleiss and H. Burkhardt, Computer Physics Communications, **81**, 372 (1994)

[32] H. Burkhardt, Proceedings of the 3rd Workshop on LEP performance (Chamonix), J. Poole (ed.), CERN SL/93-19

A Appendix: Useful Symbols and Formulae

c	Velocity of light
e	Electron charge
E	Beam energy
f_{rev}	Revolution frequency
h	Harmonic number
$\mathcal{H}$	Lattice factor $= [\eta^2 + (\beta\eta' \quad \beta'\eta/2)^2]/\beta$
I_b	Bunch current
I	Beam current in a single beam
J_x, J_y, J_s	Horizontal and Longitudinal partition numbers
$k_\perp, k_\parallel$	Transverse, Longitudinal loss factor
$\mathcal{L}$	Luminosity
m_e	Electron mass
M_b	Number of bunches in the ring
N_b	Number of particles in a bunch
P_T	Synchrotron power lost in both beams
r_e	Classical electron radius
R	Arc radius
V_{RF}	Maximum RF voltage
α_c	momentum compaction
β_x, β_y	Beta function at some point in the ring
β_x^*, β_y^*	Beta function at at the interaction point
γ	Relativistic factor
δ	Momentum variation
ϵ_x, ϵ_x	Horizontal, Vertical emittance
η	Slip factor
κ	Emittance ratio = ϵ_y/ϵ_y
λ_d	Damping decrement
μ_x, μ_y	Phase advance per cell
ν_s	Synchrotron frequency
ν_x, ν_y	Arc tunes
ξ_x, ξ_y	Beam beam tune shift
ρ	Bending radius
σ_x, σ_y	Beam radius
σ_E	Bunch energy spread
σ_x^*, σ_x^*	Beam radius at interaction point
τ_L	Beam lifetime
ϕ_s	Synchrotron phase

Luminosity

$$\mathcal{L} = \frac{N_{e^+}N_{e} \;\; M_b f_{rev}}{4\pi} \frac{1}{\sqrt{\beta^*_{x,e}\epsilon_{x,e}}\sqrt{\beta^*_{y,e}\epsilon_{y,e}}} \tag{A.1}$$

where $N_{e^+}, N_{e} \;\;$ are the bunch intensities, M_b is the number of bunches.

Equilibrium horizontal emittance

$$\epsilon_x = \frac{C_q\gamma^2}{J_x}\left[\frac{\oint \mathcal{H}/\rho^3 ds}{\oint 1/\rho^2 ds}\right] \tag{A.2}$$

The equilibrium emittance in a lattice built entirely with FODO cells scales with the horizontal phase advance μ_x^C per FODO cell as [18]

$$\epsilon_x(\mu_x^C) = 4\frac{C_q\gamma^2}{J_x}\theta^3 \frac{1 \;\; \frac{3}{4}\sin^2(\mu_x^C/2) + \frac{1}{60}\sin^4(\mu_x^C/2)}{\sin^2(\mu_x^C/2)\sin\mu_x^C}. \tag{A.3}$$

where $C_q = (55/32\sqrt{3})\hbar/mc = 3.84 \times 10^{\;\;13}$m, J_x is the horizontal damping partition number and θ is the bending angle in half of the FODO cell.

Momentum compaction

$$\alpha_C \approx \frac{L_{Arc}}{C}\frac{\theta^2}{\sin^2(\mu_c/2)} \tag{A.4}$$

where L_{Arc}, C are the lengths of the arcs and the circumference respectively, θ is the bend angle per half cell and μ_c is the phase advance per cell.

Equilibrium energy spread

$$\frac{\sigma_E}{E} \simeq \sqrt{\frac{C_q}{J_s\rho}}\,\gamma \tag{A.5}$$

where

$$C_q = \frac{55}{32\sqrt{3}}\frac{\hbar c}{mc^2} = 3.84 \times 10^{\;\;13}\ \mathrm{m}$$

for electrons and positrons. J_s is the longitudinal damping partition number, ρ is the bending radius.

Equilibrium bunch length

$$\sigma_l = \frac{c \mid \eta \mid}{\omega_s}\frac{\sigma_E}{E} = \frac{c}{\sqrt{2\pi}f_{rev}}\sqrt{\frac{\mid \eta \mid E}{heV_{RF}\cos\psi_s}}\frac{\sigma_E}{E} \tag{A.6}$$

where η is the slip factor, ω_s is the angular synchrotron frequency and the other symbols have their usual meanings.

Energy acceptance

$$(\frac{\Delta E}{E})_{accept} = \sqrt{\frac{eV_{RF}}{\pi h|\eta|E}G(\phi_s)} \tag{A.7}$$

$$G(\phi_s) = 2\cos\phi_s \quad (\pi \quad 2\phi_s)\sin\phi_s$$

Beam-beam tune shifts

$$\xi_x = \frac{N_e r_e \beta_x^*}{2\pi\gamma\sigma_x^*(\sigma_x^* + \sigma_y^*)}\,, \qquad \xi_y = \frac{N_e r_e \beta_y^*}{2\pi\gamma\sigma_y^*(\sigma_x^* + \sigma_y^*)} \tag{A.8}$$

In the limit $\sigma_x^* \gg \sigma_y^*$,

$$\xi_x = \frac{N_e r_e \beta_x^*}{2\pi\gamma(\sigma_x^*)^2} \ , \qquad \xi_y = \frac{N_e r_e \beta_y^*}{2\pi\gamma\sigma_x^*\sigma_y^*} \tag{A.9}$$

Energy lost by electrons per turn

$$U = C_\gamma \frac{E^4}{\rho}, \qquad C_\gamma = \frac{4\pi}{3}\frac{r_e}{(m_e c^2)^3} = 8.86 \times 10 \ \ ^5 \mathrm{m/GeV}^3 \tag{A.10}$$

Synchrotron radiation power in beam

$$P_{synch} = \frac{U I_e}{e} \tag{A.11}$$

Critical energy

$$E_{crit}[keV] = 2.218 \frac{E^3}{\rho} \ , \quad E \text{ in GeV} \ , \rho \text{ in m} \tag{A.12}$$

Critical Wavelength

$$\lambda_{crit} = \frac{4\pi\rho}{3\gamma^3} \times 10^{10} \ , \quad \text{in Angstroms} \tag{A.13}$$

Number of photons emitted per second by a particle

$$N_\gamma = \frac{15.0\sqrt{3}}{8.0}\frac{P_{synch}}{e N_e E_{crit}} \times 10^3 \tag{A.14}$$

where P_{synch} is in MW, E_{crit} is in keV.
Total Photon Flux

$$\dot{N}_\gamma = 8.08 \times 10^{17} \times I[\mathrm{mA}] E[\mathrm{GeV}], \quad \text{photons/sec} \tag{A.15}$$

Gas Load

$$Q_\gamma = 4.5 \times 10 \ \ ^{20} \eta_{photo} \phi_\gamma \ , \qquad [\text{Torr} \quad \text{litres/m/sec}] \tag{A.16}$$

where η_{photo} is the photo-desorption coefficient and $\phi_\gamma = \dot{N}_\gamma / L_{Arc}$ is the photon flux per unit length.

Damping partition numbers

$$J_s \simeq 2.0 \tag{A.17}$$

$$J_x + J_y + J_s = 4 \tag{A.18}$$

For a FODO cell in the thin-lens approximation

$$\frac{dJ_x}{d\delta} = 4\frac{L_D}{L_Q}\left[\frac{2 + \frac{1}{2}\sin^2\mu/2}{\sin^2\mu/2}\right] \tag{A.19}$$

Damping times

$$\tau_0 = \frac{E}{f_{rev} U}, \quad \tau_s = \frac{2}{2 + \mathcal{D}}\tau_0 \approx \tau_0, \quad \tau_y = 2\tau_0, \quad \tau_x = \frac{2}{1 \quad \mathcal{D}}\tau_0 \approx \tau_y \tag{A.20}$$

$$\mathcal{D} = \frac{\langle \frac{D}{\rho^2}(\frac{1}{\rho} + 2\frac{B'}{B})\rangle}{\langle \frac{1}{\rho^2}\rangle} \tag{A.21}$$

Longitudinal quantum lifetime

$$\tau_{quant;s} = \frac{\tau_s}{N_{QL}^2}\exp[\frac{1}{2}N_{QL}^2] \tag{A.22}$$

where

$$N_{QL} = (\frac{\Delta E_{RF}}{\sigma_E})$$

ΔE_{RF} is the energy acceptance of the bucket provided by the RF system, σ_E is the sigma of the energy distribution and τ_s is the longitudinal synchrotron radiation damping time. This is the expression due to Sands [19] but there are other (perhaps more accurate) expressions.

Transverse quantum lifetime

$$\tau_{quant;\beta} = \frac{e^{r_\beta}}{2r_\beta}\tau_\perp \tag{A.23}$$

where

$$r_\beta = \frac{1}{2}(\frac{x_{Apert,\beta}}{\sigma_\beta})^2$$

$x_{Apert,\beta}$ is the transverse position of the aperture limitation, σ_β is the transverse sigma of the particle distribution and $t_{damp,\perp}$ is transverse synchrotron radiation damping time. If there is finite dispersion at the location of the aperture limitation, then Chao's formula [20] holds

$$\tau_{quant;\beta} = \frac{1}{\sqrt{2\pi}}\frac{\exp[r_{\beta,\delta}]}{(2r_{\beta,\delta})^{3/2}}\frac{1}{(1+f)\sqrt{f(1 \quad f)}}\tau_\perp \tag{A.24}$$

where

$$r_{\beta,\delta} = \frac{1}{2}(\frac{x_{Apert,\beta}}{\sigma_T})^2 \ , \quad \sigma_T^2 = \sigma_x^2 + D_x^2\sigma_\delta^2 \ , \quad f = \frac{D_x^2\sigma_\delta^2}{\sigma_T^2}$$

D_x is the dispersion at the location of the aperture, σ_δ is the relative momentum deviation. For a fixed transverse damping time, the quantum lifetime depends on the parameters $f, r_{\beta,\delta}$ and has minimas at specific values of these parameters.

e^+e Bremmstrahlung cross-section

The dominant process which determines the lifetime at collision is small angle forward radiative Bhabha scattering which has a cross-section given by [32]

$$\sigma_{e^+e} = \frac{16}{3}\alpha r_e^2\left[\quad (\ln(\frac{\Delta E}{E})_{accept} + \frac{5}{8})(\ln(4\gamma_{e^+}\gamma_e \ ) \quad \frac{1}{2}) + \frac{1}{2}\ln^2(\frac{\Delta E}{E})_{accept} \quad \frac{\pi^2}{6} \quad \frac{3}{8}\right] \tag{A.25}$$

where $(\Delta E/E)_{accept}$ is the RF acceptance of the bucket.